5-2008

Effect of Combined Loading and Low-Temperature on the Stiffness of GFRP Laminates

Curtis Patrick Nordin
University of Tennessee - Knoxville

To the Graduate Council:

I am submitting herewith a thesis written by Curtis Patrick Nordin entitled "Effect of Combined Loading and Low-Temperature on the Stiffness of GFRP Laminates." I have examined the final electronic copy of this thesis for form and content and recommend that it be accepted in partial fulfillment of the requirements for the degree of Master of Science, with a major in Civil Engineering.

Z. John Ma, Major Professor

We have read this thesis and recommend its acceptance:

Richard Bennett, Dayakar Penumadu

Accepted for the Council:
Dixie L. Thompson

Vice Provost and Dean of the Graduate School

(Original signatures are on file with official student records.)

To the Graduate Council:

I am submitting herewith a thesis written by Curtis Patrick Nordin entitled "Effect of Combined Loading and Low-Temperature on the Stiffness of GFRP Laminates." I have examined the final electronic copy of this thesis for form and content and recommend that it be accepted in partial fulfillment of the requirements for the degree of Master of Science, with a major in Civil Engineering.

_____
Z. John Ma, Major Professor

We have read this thesis
And recommend its acceptance:

_____
Richard Bennett

_____
Dayakar Penumadu

Accepted for the Council:

_____
Carolyn R. Hodges, Vice Provost and
Dean of the Graduate School

(Original signatures are on file with official student records.)

Effect of Combined Loading and Low-Temperature on the Stiffness of GFRP Laminates

A Thesis
Presented for the
Master of Science
Degree
The University of Tennessee, Knoxville

Curtis Patrick Nordin
May 2008

DEDICATION

This thesis is dedicated to all of those people who have made life a journey truly worth taking. My parents, David and Carol Nordin, for always supporting, inspiring, and encouraging me in all walks of life. My siblings, Kenneth and Merilee, for a lifetime of warm memories and continued moral support. My dear friend, Sarah Limper for keeping graduate school entertaining with her crazy personality and deeply genuine friendship.

"Every man builds his world in his own image. He has the power to choose, but no power to escape the necessity of choice." - Ayn Rand

ACKNOWLEDGMENTS

I would like to thank Dr. John Ma for his continued support and useful guidance throughout the entire research process. Also I wish to thank Dr. Dayakar Penumadu for providing access to his testing equipment and for being understanding and helpful throughout the testing program. I would also like to acknowledge all of Dr. Ma's research team, especially Dr. Baisong Du and Dr. Hyoseon Ji, for their cooperation and useful insight into various aspects of composite theory. I wish to also thank Akawat Siriruk for his greatly appreciated assistance with the testing equipment. I wish to thank Ken Thomas and Larry Roberts for their often-sought assistance setting up and fixing the testing equipment. Jerry D. Plunkett the president and CEO of Kansas Structural Composite Inc. for his continued support of FRP research and donation of the glass fiber reinforced polymer (GFRP) materials. The National Science Foundation - NSF CAREER program (CMS – 0550899) for providing financial support for the research. Finally I would like to thank Dr. John Ma, Dr. Dayakar Penumadu and Dr. Richard Bennett for serving on my committee.

ABSTRACT

At the present time a large portion of America's bridge infrastructure is aging, and in many cases approaching its design live. Therefore, there is a need for structurally sound, low-maintenance, and rapidly constructible alternatives for conventional materials. Due to this need there has been a renewed interest in structural glass fiber reinforced polymer (GFRP) products. A large portion of the US is regularly subjected to freezing temperatures and therefore the numerous gaps in our knowledge and understanding of the low-temperature response of GFRP materials need to be addressed. Although strides have been made in researching the cold climate responses of GFRP materials, a lack of comparable testing procedures and reproducible results has lead to confusion and a lack of confidence applying them. Therefore this thesis presents a detailed theoretical analysis of a structural GFRP bridge deck panel, and documents a research program that observed the effects of low-temperature and strain levels on the longitudinal modulus of GFRP samples. A series of GFRP coupon laminates were tested at 1000, 2000, and 3000 micro-strain levels at temperatures down to –31 F [-35 C]. Both biaxial and uniaxial samples subjected to 1000 micro-strain showed an increase in stiffness as the temperature was lowered, and no significant reduction in stiffness was seen when the samples were warmed back up to room temperature and retested. However samples subjected to the higher strain levels did show significant stiffness degradation when retested. The degree of degradation was noticeably larger for samples subjected to the low temperatures than for control samples that were subjected to the equivalent number of cycles at room temperature. It was also noted that the degradation due to load cycles or temperature coupled with load cycles was noticeably less for uniaxial samples than for biaxial samples.

TABLE OF CONTENTS

LIST OF TABLES

LIST OF FIGURES

CHAPTER 1

INTRODUCTION

1.1. History of Fiber Reinforced Polymer

The benefits of fiber reinforced polymer (FRP) composites have been studied since the early 1940's, when its strength-to-weight ratio along with its excellent resistance to weather and corrosion were first used heavily by the military for aerospace and naval applications. It was not long before fiberglass pipe and other commercial applications were developed. Since its early heyday FRP products have been used widely in many non- or minor-structural applications including architectural, marine, electrical, corrosion-resistance and automotive. Until recently the primary structural use for FRP materials has been in the aerospace industry, which is reaching a high level of sophistication due in part to a long period of use, acceptable modeling techniques, as well as an accepted industry standard. Due to the specialty nature of these products as well as their precision fabrication and high costs, they cannot be readily applied to the mainstream construction industry.

Many other countries have to one degree or another been studying and implementing structural FRP designs for the last twenty to thirty years, but America saw only small-scale designs and a limited degree of interest until the early nineties. At the present time a large portion of America's infrastructure is aging, and in many cases approaching its design live, therefore need for structurally sound, maintenance-free, and economically feasible alternatives for conventional materials has prompted a renewed

interest in structural FRP products. Some of the main problems currently facing the advanced composites for construction industry are the high initial manufacturing costs of FRP materials, their short period of use, and the lack of industry testing and design standards. FRP materials vary from traditional materials due to their composite nature and time dependant behavior therefore current design and testing procedures are not adequate and this has resulted in FRP technology not being widely accepted. In spite of these challenges FRP materials are slowly emerging in the construction industry and as of today their primary use is FRP reinforcing bars in standard reinforced concrete structures particularly when steel corrosion is a concern, and the repair and rehabilitation of existing bridges using FRP laminates. There is a significant body of completed as well as ongoing research into both of these applications, but neither takes full advantage of the strength-to-weight ratio of FRP materials.

1.2. FRP Constituents and Manufacturing Processes

Fiber reinforced polymer materials are made of a polymer or plastic matrix within which a fibrous material is embedded. This system of different materials works compositely where each individual or constituent material remains physically identifiable but contributes desirable properties to the overall structural material. The physical performance of FRP materials is highly dependent upon the individual constituent properties of which the composite is made. A quick overview of FRP constituent materials and common manufacturing methods is detailed below, and many of the details were obtained from a Colorado Department of Transportation report written by Cusson and Xi.

1.2.1. Fiber Reinforcement

Glass, carbon, and aramid are the most commonly employed organic and inorganic materials being used for the fibrous reinforcement. Typically the fibers used in FRP materials are continuous thread-like materials with extraordinary axial strength and stiffness. The fibers provide the majority of the material strength, but are susceptible to environmental corrosion, and due to their small aspect ratios react poorly in compression.

Glass fibers are inorganic silica based materials and can achieve very high tensile strengths if the glass surface is protected from abrasion, moisture and water vapor. Glass fibers are broken down into three main types, E-glass, S-glass, and C-glass. E-glass or economical glass fibers comprise about 80-90% of commercial glass production. S-glass or high strength glass fibers are nearly 1/3 stronger than E-glass but tend to be expensive to produce and are currently most prevalent in military applications. C-glass or corrosion resistant glass fibers exhibit excellent resistance to corrosion and are useful where acidic or chemically aggressive environments exist.

Carbon fibers are organic carbon based materials and can achieve high stiffness and corrosion resistance, but have low toughness and impact resistance. Carbon fibers come in two main types, high modulus and high strength. Also graphite fibers use carbon that has been graphitized and contains carbon content greater than 99%.

Aramid fibers are organic based liquid crystal polymers that exhibit good fatigue, abrasion resistance, corrosion resistance, and high thermal stability. Aramid is in the nylon family and is less dense and has a lower Young's modulus when compared to carbon fibers. Aramid is also less brittle than glass or carbon, but does not bond to the matrices as well.

1.2.2. Matrix Polymers

Matrix polymers include two main classifications: thermoplastic and thermosetting. Thermoplastic polymers can be repeatedly softened at high temperatures and then recast. Thermoset polymers undergo a chemical reaction when cured and therefore are unable to be softened or recast. Most structural applications for FRP materials use thermoset polymers.

The thermoset polymer matrix protects the FRP composite from environmental degradation, provides lateral support to counter fiber compression buckling, and allows for stress transfer between the fibrous reinforcement. The matrix also provides the FRP materials with good thermal stability and chemical resistance. For enhanced structural performance additives can be used to help specific problems (Ultraviolet inhibitors, dies, ect.). Some common thermosetting resins include: epoxy, polyester, and vinyl ester.

1.2.3. Manufacturing Processes

Several composite manufacturing processes exist, and it should be noted that a FRP product's final characteristics depend heavily on three factors: the material composition, the process of fabrication, and the level of quality control during manufacturing process. Two of the main manufacturing processes for construction based FRP materials are pultrusion and hand lay-up.

Pultrusion is currently the most popular method for manufacturing linear composite members with the primary fibrous reinforcement in the longitudinal direction. The pultrusion process involves using guide plates to align the continuous reinforcing fibers called rovings or continuous fiber mats. Then the fibers are drawn through a liquid

polymer solution of resin filler, hardening catalyst, and other add-mixtures. Once the fibers are wetted they are drawn through a steel die form guide with the desired cross-sectional properties. At this point the formed mass is heated to harden it and a solid polymer material with a given cross-section emerges. Pultrusion provides very good quality control, and the process can be essentially automated.

Hand lay-up is an open mold process where the constituent materials are applied to a mold in successive plies or layers. Each layer involves applying either dry or resin-impregnated reinforcements after which resin and hardeners are added to the layer. The composite is then built up and worked by hand. Hand lay-up composites are typically cured at room temperatures, but can also be cured at elevated temperatures to accelerate the curing process if desired.

1.3. FRP Materials Used in Bridge Applications

Bridge design and construction provides an ideal application for utilizing the strengths of FRP materials. FRP components were first introduced into small-scale bridge designs as early as the 1970's. The construction of the 370 ft long all FRP pedestrian bridge in Scotland across the river Tay in the early 1990's was the first large-scale implementation of FRP composites being used in a bridge application. Since then FRP pedestrian bridges have been successfully built in Europe, Asia, and the United States, and are a valuable alternative to standard construction materials when their significant weight reduction is a benefit, such as the installation of two remote pedestrian bridges in Hawaii's Haleakala National Park (Johansen, et al. 1996). Lightweight FRP members can be installed or airlifted into place without the use of heavy equipment

allowing installation in locations that would have been inaccessible otherwise. Another FRP bridge application that is being developed is FRP bridge deck panels; recent studies have shown FRP composite bridge deck systems to be a valuable alternative to conventional deck systems. Due to their high strength-to-weight ratio these panels are about one-fourth the weigh of concrete decks, which greatly reduces the dead load on the bridge structure. Also they are typically quick to install and do not require the heavy equipment necessary for standard pre-cast concrete panels, nor the lengthy curing time of poured concrete decks. With many of America's interstate bridge structures approaching their design life FRP deck panels allow for rapid construction and significantly reduced closure times. Also with the reduction of weight the use of FRP bridge decking could in some cases allow for the existing superstructure to remain in use under elevated traffic loads.

Typically there are two general types of FRP decks used for bridge applications; these include pultruded decks, and sandwich decks. The pultrusion fabrication method was explained earlier in section 1.2.3. Pultrusion is very useful in fabricating linear members with unchanging cross-sections; therefore pultruded deck panels typically resemble w-beams, box beams, or other constant cross-sectional members. Sandwich deck panels are fabricated with a type of core material or geometry sandwiched between a top and bottom face sheet. The face sheets resist the tensile and compressive flexural stresses while the core resists out-of-plane forces and shear stresses.

1.4. FRP Concerns

While bridge deck systems take advantage of the excellent strength-to-weight ratio and corrosion resistance of FRP composites there remains other concerns that could affect the structural soundness of the material, these include: connection details, failure modes and ultimate behavior predictions, lifetime durability and high as well as low temperature effects.

1.4.1. Connection Details

Connection detailing for FRP members are particularly critical due to their anisotropic nature. Stress concentrations caused by connection details can have undesirable effects if not properly modeled and understood. Typical connection details between panels still remain in the hands of the manufacturer and very little continuity exists between them. This leads to an ambiguous and confusing installation procedure, which eventually costs more in labor and hinders the widespread acceptance of FRP deck systems (Rightman, *et al.* 2004). Typical deck/girder connections for FRP materials include: stud-type connections, clamped connections, and bolted connections. Shear stud connections have had favorable results but lack uplift support. Clamped connections tend to provide adequate horizontal as well as uplift support, but are labor intensive and generally need to be installed from underneath the bridge decking. Bolted connections are effective but the installation can be very labor intensive, and Rightman has reported post installation inspection problems. Various connection details have been reported to help standardize the panel-to-panel as well as girder-to-deck connections, and research is ongoing in this area.

1.4.2. Failure Modes and Ultimate Behavior Predictions

Failure mechanisms are dependent not only on the basic material properties, but are also highly dependent on the structural properties of a given sample. In general the mode of failure for FRP materials is sudden and brittle and shows an almost linear-elastic response to failure (Cheng, *et al.* 2005). Sandwich panel configurations are common in bridge deck panels and are particularly susceptible to debonding of the top and bottom face sheets when loaded to failure or even under service level fatigue loading (Reising, *et al.* 2004). Also any unsupported edges of the deck panels are prone to failure and should be supported or avoided when possible (Zhou, *et al.* 2005).

1.4.3. Lifetime Durability

Although one of the major considerations in the selection of FRP materials is the claim of long-term durability in comparison to conventional materials, there is a lack of long-term durability data. A study completed in 2003 showed sever gaps in FRP durability knowledge, in fact there was evidence that civil structures often were subjected to environments that can cause FRP composites to undergo significant degradation. It was shown that there was a critical lack of data for: extended time periods (18+ months), the effects of field curing on the overall performance of FRP materials, of standardized short term representative tests and conditions, response and protection of FRP materials under intended and accidental damage, and finally testing data under combined conditions that are readily seen under field conditions (Helbling, *et al.* 2006).

1.4.4. High Temperature Effects

There are two critical components to fire engineering: initial performance, and behavior under fully developed fires. A materials initial fire performance is determined by how combustible it is, how well it propagates or retards fire growth, and other safety concerns such as smoke generation and toxicity. While combustibility and fire propagation are the primary concern with respect to bridge engineering, a materials behavior under the rare condition of a fully developed fire is an important life safety concern. So the performance of FRP materials under fire conditions need to understood with respect to both its initial performance, and its behavior under fully developed fire conditions.

FRP composite materials have a polymer based matrix, which will burn if subjected to a sufficiently high temperature. Common matrix materials are polyester, vinyl ester, and epoxy, these materials in their native form not only support combustion, but also suffer degradation in strength, stiffness, and bond properties (Williams, B. K., 2004). Thick FRP sections tend to behave better than thinner sections because as the outer matrix is burned the relatively temperature insensitive fiber reinforcement creates a layer of insulation protecting further fire propagation (Sorathia, *et al.* 2001). Though the problem of combustibility and fire propagation can be sufficiently addressed by adding fire retardant admixtures to the matrix resin, there has yet to be an established critical temperature for FRP materials although it is widely believed to be in the range of 392-572 °F [200-300 °C]. Also there are concerns regarding the post-fire strength and stiffness of FRP materials because there is essentially no information on this topic.

1.4.5. Temperature Cycling and Low Temperature Effects

Many locations in the US are subjected to extreme winter temperatures, significant temperature transitions over relatively short periods of time and freeze-thaw cycles. Unique difficulties arise when fiber-reinforced polymer composites are subjected to these harsh environmental conditions, these difficulties arise due primarily to the materials micro-structural characteristics. The addition of the fiber reinforcement to the resin matrix creates an anisotropic stiffness, and allows potentially sever residual stresses to build up due to varying coefficients of thermal expansion between the constituent materials. The coefficient of thermal expansion of the matrix is usually an order of magnitude larger than the fibers, and when multiple layers are present with different fiber orientations the mismatch in the thermal expansion coefficients has to be taken into consideration not only between the matrix/fiber interface, but also between the layers. The mere cooling of FRP materials from their curing temperatures to room temperature can subject the material to sever enough internal stresses as to develop micro-cracking within the matrix (Dutta, Lampo 1993). The three main low temperature problems as outlined by Dutta and Lampo include: low temperature residual stresses, material degradation due to environmental cycling, and moisture effects under freeze-thaw cycling.

1.4.5.1. Low Temperature Residual Stresses

Dutta studied the temperature effects of FRP composites as early as the 90's. It was found that in general most matrix resins show an increase in stiffness and strength

with a decrease in temperature (Dutta, Lampo 1993). However as the resin shrinks due to a reduction in temperature the relatively stiff fibers resist the contraction thereby developing internal tensile stresses within the resin matrix which when large enough cause and propagate existing micro-cracks thereby counteracting the natural increase in the matrix stiffness. So in general FRP composites stiffen up at lower temperatures and the overall performance is increasingly dominated by the matrix's behavior. The type of matrix will greatly affect all the mechanical properties at lower temperatures. Uniaxial and longitudinal fiber dominated samples have shown a reduction in ultimate strength due to extreme low temperatures, while samples with a low proportion of longitudinal to transverse fibers have shown little effect and possibly a slight increase (Dutta, Lampo 1993). The transverse fiber-dominated samples show little effects due to low temperatures because they are primarily matrix dominated. Dutta and Lampo proposed a "Wavy fiber" theory to help explain the loss of strength seen in longitudinal dominated samples. His explanation was that the fibers had some waviness due to micro-buckling of the fibers when the matrix was cured thereby creating stress concentrations. Increased matrix stiffness does not allow the matrix to yield at these stress concentrations resulting in a non-uniform load distribution between the fibers, which causes a reduction in the ultimate strength.

1.4.5.2. Material Degradation Due to Thermal Cycling

As previously stated internal stresses create micro-cracks within the matrix due to differing coefficients of thermal expansion. Thermal cycling rapidly propagates these

micro-cracks, which result in a reduction in stiffness. This was shown by tests in which transverse fiber dominated samples showed a decreased ultimate strength, but longitudinal fiber dominated samples showed an increase in strength. Once again Dutta's "wavy fiber" theory explains this increase. The fibers develop stress concentrations due to micro-buckling during the curing process which is amplified as the matrix stiffness increases, but the softening of the matrix due to the propagation of micro-cracks allows the fibers to re-straighten thereby reducing the stress concentrations and allowing higher ultimate strengths to be reached (Dutta, Lampo 1993). This increase in ultimate strength was also seen between aged and un-aged FRP reinforcing bars which showed a 5% increase in strength (Dutta, Porter 2004). These are general patterns and tend to be material specific were different fiber/matrix combinations react differently. For example military S2-glass/polyester samples thermally cycled to extremely low temperatures 250 times showed much less degradation than E-glass/polyester samples which degraded to the point of failure after only 100 cycles (Dutta, Hui 1996). In general any matrix-dominated behavior will be adversely affected by micro-crack propagation associated with thermal cycling.

While the ultimate strength increase is a positive aspect offsetting the reduction in stiffness, it was also shown that by aging samples through thermal cycling the failure mechanism in both tension and compression became much more brittle (Dutta, Porter 2004). Research is underway to produce more ductile FRP reinforcing bars, which have the possibility of being implemented in other FRP constructions. The University of Missouri-Rolla is developing Pseudo-ductile bars using different types of fibers that fail at different times during loading. Also bars with bilinear stress-strain characteristics

similar to steel and with a Young's modulus approaching that of steel are being developed at Drexel University (Cusson, Xi 2002).

1.4.5.3. Freeze-Thaw Cycling Effects

Freeze-thaw cycling is primarily an issue when the structure has a significant quantity of water. The same is true for FRP materials. Water migrates into the matrix by water absorption and through the micro-cracks, then as the structure undergoes freezing the water expands creating internal stresses, which further propagate matrix cracking. Rivera and Karbhari found that cyclic freeze-thaw reduced the strength as well as the stiffness of the material similar to thermal cycling. It was found that carbon based fibers had a more significant compressive loss than glass fibers which was attributed to the carbon fibers weaker bond to the vinyl ester matrix. That paper also showed that the tensile modulus was more significantly degraded in E-glass samples. There still remains a fundamental lack of understanding of the basic mechanisms of degradation due to freeze and freeze-thaw cycles (Rivera, Karbhari 2001).

1.4.5.4. Large-Scale Problems Due to Temperature

Temperature not only affects the micro-structural properties of FRP products but is also a concern with full-scale members. In Dayton, Ohio four FRP bridge deck systems were incorporated into a new bridge. Two panels were created using sandwich constructions. Thermal characteristics of the various panels created an uplift difference at the joints, and significant cracking of the overlay (Reising, *et al.* 2004). This resulted

in connection problems, increased localized stresses, and increased maintenance costs. Also there are issues involving the structural performance of FRP sandwich panels. One of the primary failure mechanisms of a sandwich panel is the delamination of the core from the face sheets (Chen, Davalos 2004), and special attention needs to be focused on how temperature affects this bond.

1.5. Literature Review on Effects of Low-Temperature

This thesis and the corresponding experimental research will focus on the effects of low temperature and low temperature phenomenon on the material properties of E-glass/Polyester GFRP samples fabricated using a hand lay-up process. Therefore a survey of literature on these specific topics was conducted. For clarity each important source is presented separately.

1.5.1. Behavior of Fiber-Reinforced Plastics as Construction Materials in Extreme Environments: Dutta, Lampo 1993

Dutta and Lampo defined how the design and analysis of traditional materials have serious limitations when directly applied to fiber-reinforced polymers. The primary difficulties mentioned are related to the micro-structural characteristics of FRP materials. The coefficient of thermal expansion of an FRP's matrix is usually an order of magnitude greater than that of the fibers. Cooling of the FRP material from the fabrication process temperature to normal environmental conditions cause residual stresses proportional to the difference in temperatures. For cold environments these temperature changes can be as large as 200 °F, which can cause residual stresses large enough to create micro-cracks

within the matrix and the matrix-fiber interfaces. Also, most FRP resins used in creating the FRP's matrix become stronger and stiffer as they are cooled. Finally, moisture absorption causes swelling of the matrix, which reduces the FRP materials strength and stiffness. Micro-cracks can exasperate the absorption of water leading to an increased reduction in stiffness and therefore more micro-cracking. That paper therefore focuses on the theoretical evaluation of the residual stress buildup within each FRP lamina or layer, the theoretical evaluation of the laminates hygrothermal properties, as well as an accumulation of previous cold temperature FRP studies conducted at the U.S. Army Cold Regions Research and Engineering Laboratory. Four potential problem areas were identified for short- and long-term cold regions related environmental effects: low temperature residual stress, material degradation due to low-temperature environmental cycling, moisture effects of freeze-thaw cycling, and the long-term effects of loading history combined with environmental effects in relation to the material durability. The effects of low temperature and low-temperature thermal cycling on tensile strength were characterized by testing 300 composite specimens under various low temperatures (Figure 1.1). The tensile strength of uniaxial $[0]_6$ laminates decreased, longitudinal fiber-dominated $[90_20_2]_S$ laminates slightly decreased, transverse fiber-dominated $[90_20]_S$ laminates slightly increased, and off-axis $[45/-45]_6$ laminates showed no change. The degradation of the FRP material properties due to low temperature exposure was explained with a wavy fiber theory. This theory states that due to matrix stiffening any curvature or waviness in the fibers will produce large localized stress concentrations in the fibers. This stress concentration will result in the fiber failing at a lower load then under a less stiff or warmer matrix. The effects of low temperature on the flexural

strength of uniaxial graphite/epoxy FRP composite's flexural strength and fatigue durability were investigated by fatigue loading specimens for 100,000 cycles at various temperatures (Figure 1.2). The effects of thermal cycling for both glass-epoxy and graphite-epoxy laminates were determined by testing the durability under low temperature thermal cycling. The composites were subjected to -292 °F [-180 °C] temperatures and thermally cycled. The flexural strength was reduced in the transverse and off-axis directions, but increased in the longitudinal direction. The transverse fracture surfaces viewed under an electron microscope showed a progressive increase in smoothness with thermal cycling. That paper postulated that the thermal cycling induced micro cracks in the matrix thereby decreasing matrix dominate properties, but increased fiber dominated properties.

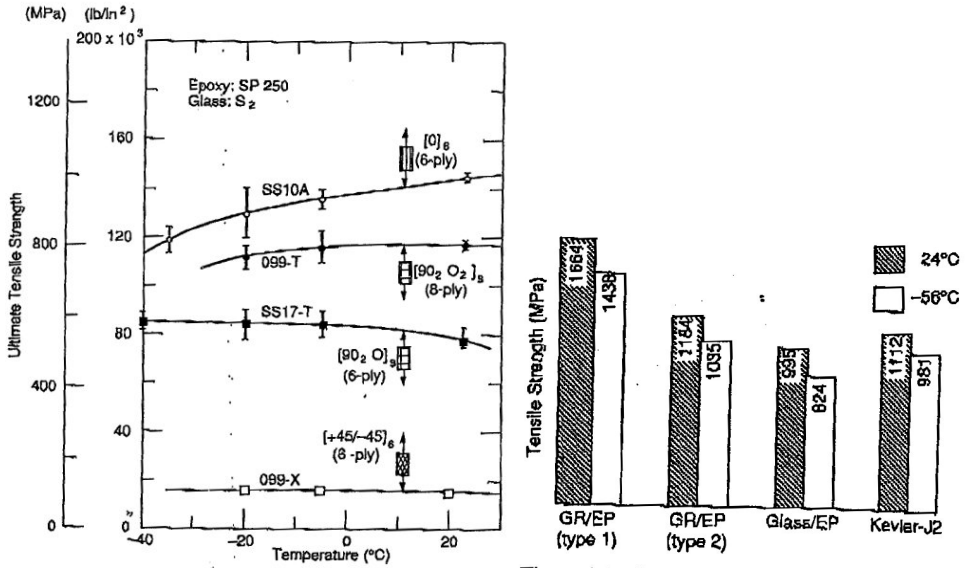

Figure 1.1 – Effects of Low Temperature on Tensile Strength of Laminates (Dutta , Lampo 1993)

1.5.2. Low-Temperature and Freeze-Thaw Durability of Thick Composites:

Dutta, Hui 1996

Dutta and Hui note that currently there are no appropriate models to describe FRP materials subjected to both multi-axial loading and environmental exposure. External loading even under simple unidirectional cases cause complex multi-axial stresses within each ply, complicating things further is the fact that most FRP laminates have multiple plies orientated in different directions. Superimposed on these loading stresses are the thermal effects of changing stiffness, induced thermal stresses, exasperated residual stresses, and finally the influx of water coupled with freeze-thaw cycles. Therefore the fundamental response behavior of FRP composite materials would be functions of external loading, as well as its thermal and hygrothermal environment, structural geometry, and material characteristics. As a result that study tested thick specimens of both commercially available E-glass reinforced polyester and military grade S2-glass reinforced polyester. The E-glass samples were fabricated using a pultrusion process, while the S2-glass samples were fabricated using a silicone rubber vacuum bag

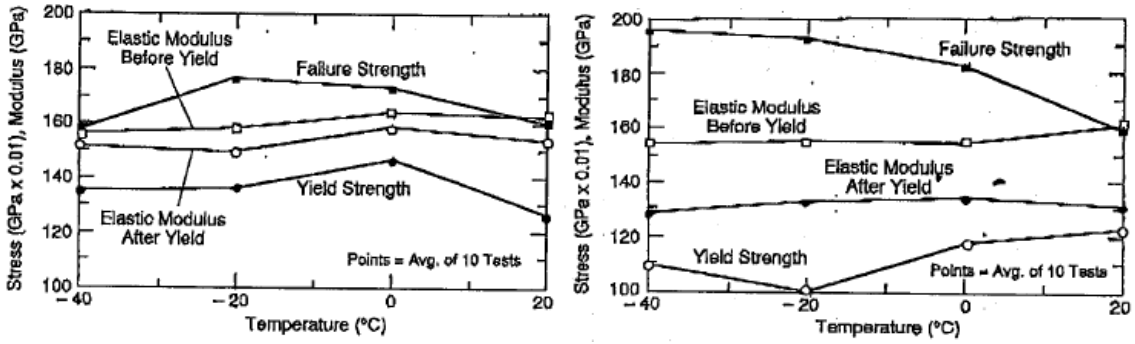

Figure 1.2 - Low Temperature Effects on Beam Flexure
(A) Pre-Fatigue and (B) Post-Fatigue
(Dutta, Lampo 1993)

Table 1.1 - Sample Materials and Test Specifications (Dutta, Hui 1996)

S2-glass FRP composite	E-glass FRP composite
Process: Vacuum bag	Process: Pultrusion
Fiber: S2-glass	Fiber: E-glass
Matrix: Polyester	Matrix: Polyester
Density: 0.068 lb/in^3	Density: 0.071 lb/in^3
Volume fraction of fiber: 0.532	Volume fraction of fiber: 0.593
Number of specimens: 27	Number of specimens: 18
Specimens per batch: 9	Specimens per batch: 9
Dimensions:	Dimensions:
Length: 13.0 in	Length: 13.0 in
Section: Square	Section: Square
Conditions of test:	Conditions of test:
Span: 10 in	Span: 10 in
Test temperatures	Test temperatures
81 F	81 F
23 F	23 F
-40 F	-40 F
-76 F	-76 F
Thermally cycled 250 times between 122 F and -76 F temperatures	Thermally cycled 100 times between 122 F and -76 F temperatures

technique. Sample materials and test specifications can be found in Table 1.1. The samples were tested in three-point bending using ASTM Short Beam Method (D 2344), the Young's modulus and shear modulus were obtained at 81, 23, -40, -76 °F [27, -5, -40, and -60 °C]. After the initial flexural tests the samples were subjected to 250 thermal freeze-thaw cycles between 122 °F [50 °C] and -76 °F [-60 °C] with a two hour duration at each temperature and a 15-20 minute window to allow for the temperature change. Finally the samples were to be tested in flexure once again to determine the affects of the thermal cycling. The experimental tests involved the use of a 60 kip universal testing machine to induce the load. The flexural test span was 10 inches, and the supports were provided by 1 inch loading pins. The crosshead load rate was 0.1 or 0.2 in/s depending

on the sample. Deflections were obtained by a cantilevered extensometer. The low temperature testing was conducted in the interior of an environmental chamber, which used evaporated liquid nitrogen for cooling.

The testing results for both types of FRP materials showed an increase in both the Young's and shear modulus with a reduction of the temperature (Figure 1.3). It was also noted that low-temperature thermal cycling had a significant influence on the degradation of both the Young's and shear modulus for both materials. The degradation of the commercial pultruded E-glass composite was so severe that after 100 thermal cycles macroscopic cracks developed within the central part of the cross-section, and the samples could not be tested in flexure again. The S2-glass material did not show any

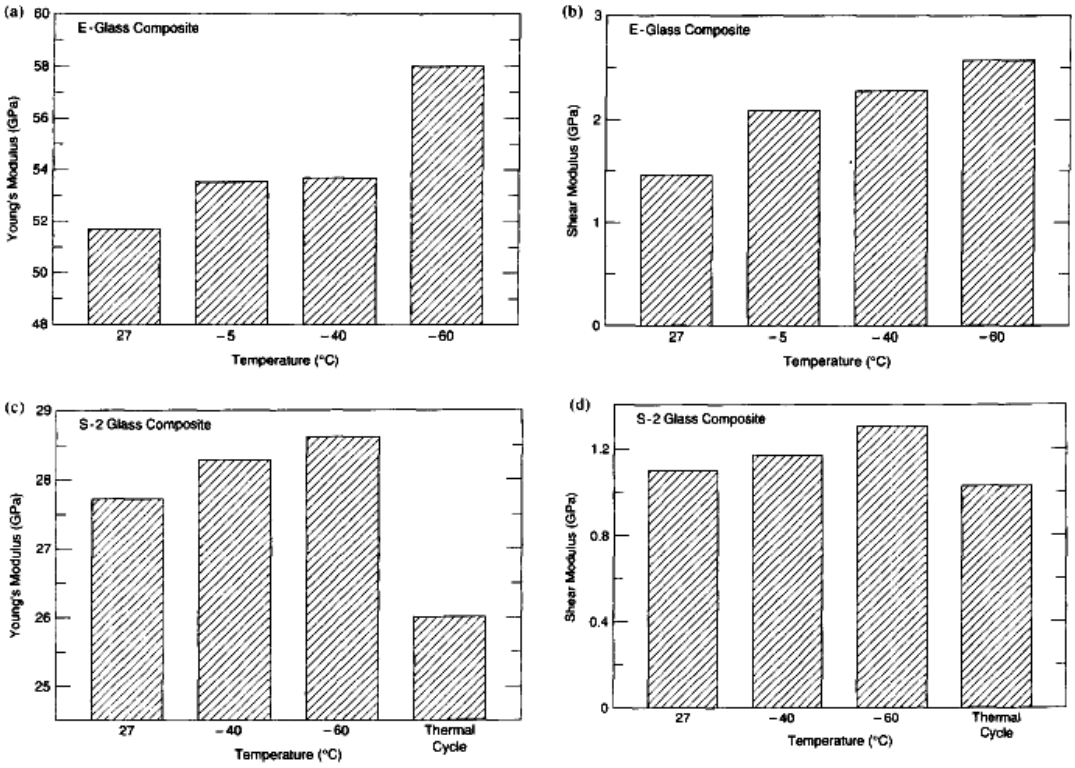

Figure 1.3 - Young's and Shear Modulus Results at Various Low Temperatures (Dutta, Hui 1996)

signs of cracking, but when tested in flexure again a noticeable decrease in both the Young's and shear modulus were noticed (Fig. 1.3). That paper attributed this to the matrix degradation.

That paper concluded that the thermal stresses in the matrix are a function of the matrix materials young's modulus, coefficient of thermal expansion, and the change in temperature from the 'stress-free' temperature (usually the curing temperature). This relationship is shown in the following simplified equation: $\sigma_{mL} = -E_m \cdot \alpha_m \cdot \Delta T$.

The large theoretical thermal stresses induced at low temperatures could at times significantly exceed 50% of the matrix's tensile strength. Therefore it is evident that those stresses could become potentially damaging. That damage could begin with the formation of microscopic cracks in the matrix or matrix/fiber interface, the micro-cracks then develop and coalesce into macroscopic cracks. It was argued that this may account for the thermal cycling degradation seen by both FRP materials. Those stresses and the corresponding damage were intensified with the pultruded E-glass fibers to the point of failure after 100 thermal cycles.

1.5.3. Characterization of Sub-Zero Response of Vinylester FRP in Civil Infrastructure Renewal: Rivera, Karbhari 2001

Rivera and Karbhari state that there is a large body of research on the durability of aerospace grade autoclave cured composites, but that grade of material differs substantially from the set of materials and fabrication processes likely to be used in civil infrastructure applications. The effects of cold region climates on civil type FRP materials is of special concern because in addition to the cold climate material response,

the absorption of moisture coupled with freeze and the freeze-thaw phenomenon could lead to irreversible physical and chemical changes. Rivera argues that there is still a critical lack of understanding of FRP degradation due to freeze and freeze-thaw regimes, therefore a series of testes were conducted to determine the durability of carbon and E-glass reinforced vinyl ester composites after being subjected to short-term freeze and freeze-thaw conditions. These tests were specifically aimed at materials and fabrication processes used in the application of seismic retrofitting and strengthening of deteriorated concrete columns. The E-glass and carbon composites were fabricated using the wet lay-up process with a VE-8117 vinyl ester resin. The samples were comprised of both flat plates and hollow cylindrical specimens comprised of three uniaxial layers. The regiment of tests included moisture absorption, tensile tests, compression tests, split-D tests, and dynamic mechanical thermal analysis (DMTA). This review will focus on the flat specimens moisture absorption and material properties because the cylindrical samples, split-D, and DMTA are off topic.

Moisture absorption was tested using both deionized water and a 5% NaCl solution, and was measured using gravimetric means. Figure 1.4 shows the absorption results, and it can be seen that all of the flat specimens showed a decrease in weight due to leaching of the composite materials into the solution. To determine the effects of the environment on tensile strength, compressive strength and tensile modulus, samples were tested at five environmental conditions. These five conditions consisted of 100 days conditioned at (a) unexposed, stored at 23 °C and 55% RH, (b) dry freeze, kept at -10 °C at 50% RH, (c) freeze-thaw (dry), cyclic regime between -10 °C and 22.5 °C at 50% RH, (d) freeze-thaw (water), cyclic regime between -10 °C and 22.5 °C while immersed in

water, and (e) freeze-thaw (sea water), cyclic regime between -10 °C and 22.5 °C while immersed in a NaCl solution. The results can be found in Figure 1.5, and it should be noted that the dry freeze increased all the material properties while the dry freeze-thaw saw reduction in some properties. The increase in the compressive strength due to the dry freeze was consistent with the idea of matrix hardening or "embrittlement". A drop in the tensile modulus was only seen in the E-glass composite and was attributed to fiber-resin interface debonding due to hygrothermal fatigue during the freeze-thaw cycling. The freeze-thaw cycling in water was degrading to all material properties but was particularly damaging to the compressive strength, which is a matrix-dominated property. The carbon composite showed the greatest compressive strength degradation. This drop in compressive strength was attributed to resin relaxation and depolymerization, as well as matrix cracking due to the freeze-thaw. The freeze-thaw cycling in a NaCl solution showed larger degradation in the fiber-dominated properties of tensile strength and tensile modulus, and less degradation of the compressive strength than water. The more

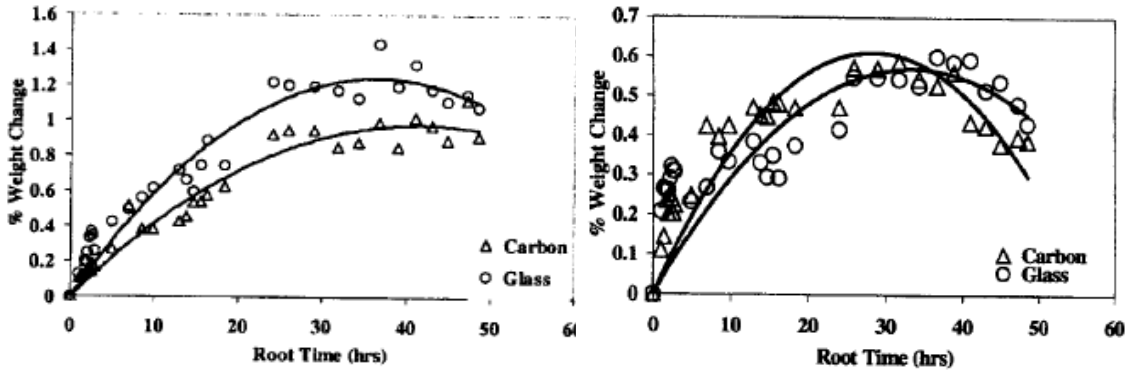

(A) **(B)**

Figure 1.4 - Percent Weight Change of Flat Specimens
(A) deionized water and (B) 5% NaCl Solution
(Rivera, Karbhari 2001)

sever drop in the tensile properties was attributed to a synergistic effect of the sodium chloride.

1.5.4. Fatigue Evaluation of Multiple Fiber-Reinforced Polymer Bridge Deck Systems Over Existing Girders – Phase II Report: Dutta, et al. 2003

Dutta states that some of the key technical issues relating to FRP bridge decks have been identified as (a) structural system response, inspection, maintenance and repair; (b) joints and connections; and (c) materials and manufacturing. To increase our knowledge of FRP materials Dutta conducted an experimental fatigue study of five deck prototypes (Table 1.2). The full-sized decks included three FRP composite decks, one hybrid FRP-concrete deck, and one reinforced conventional bridge deck system. The FRP composite decks included one fabricated using a Vacuum Assisted Resin Transfer

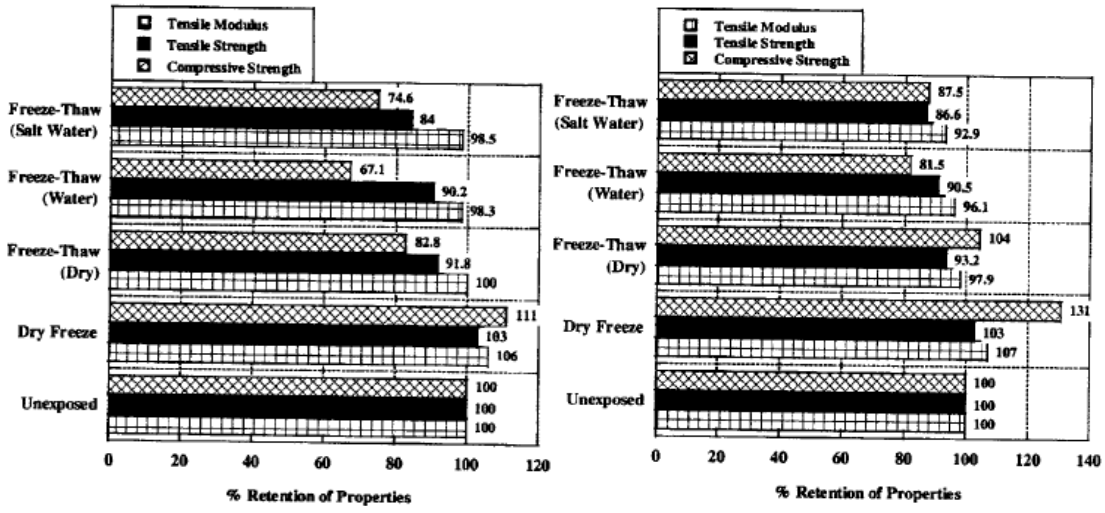

Figure 1.5 - Changes in Mechanical Properties due to Low Temperature Conditions (A) carbon and (B) E-glass composites (Rivera, Karbhari 2001)

Table 1.2 - Bridge Deck Prototypes
(Dutta, *et al.* 2003)

Deck No.	Deck Material	Dimensions (mm)	Fabrication Process	Resin Matrix	Reinforcements
Bridge #1	Conventional Reinforced Concrete	1,829 x 6096 x 179		N.A.	
Bridge #2	Hybrid FRP Concrete	1,829 x 6096 x 203	Cast in Place	Polyester Vinyl ester	E-glass Roving/ Directional-bias Fabric
Bridge #3	FRP Composite Sandwich	1,829 x 6096 x 203	VARTM	Vinyl ester	Multi-Axial Stitched E-glass/ Integral Cell Core
Bridge #4	FRP Composite	1,829 x 6096 x 203	Pultrusion	Vinyl ester	E-glass Continuous Roving/ Multi-Axial Stitched E-glass
Bridge #5	FRP Composite Sandwich	1,829 x 6096 x 203	Hand Lay-up	Isophthalic Terephthalic Polymer	Honeycomb Core/ Biaxial E-glass mat

Molding (VARTM) process, one fabricated using the pultrusion process, and one fabricated by a hand lay-up process. All the decks were evaluated under two extreme temperatures to assess the response between temperatures. The decks were subjected to one million simulated wheel load cycles at -22 °F [-30 °C], and another one million cycles at 122 °F [50 °C]. Finally the panels were subjected to another four million cycles at both the low and high temperatures for a total of 10 million cycles. Each deck was placed on three W36x182 steel girders, which resulted in a continuous two span bridge setup. Two actuators applied the load onto steel plate/elastomeric pads centered with respect to the support spans. The load was designed to simulate the AASHTO HS20-44 design truck wheel load, and was applied at a rate of 3.5 Hz. Each deck was

instrumented using strain gauges, thermocouples, and linear voltage differential transducers (LVDT). The deck tests were conducted in a cold room after it achieved equilibrium with the target temperature. Static testes were conducted at specific intervals to determine the load-deflection and load-strain responses. The static tests were loaded at a rate of .04 in/min, and data was logged at three-second intervals.

The results of the fatigue tests (Figure 1.6) showed that although the FRP decks did not fail there was a noticeable degradation of the stiffness. Therefore it was concluded that fatigue damage accumulated which promoted degradation to the stiffness and lead to residual deformation of the deck and deck/girder connections. Overall the reinforced concrete control deck as well as the FRP-concrete hybrid deck showed the highest stiffness. The temperature effects on the load-deflection response included an expected reduction in stiffness at higher temperatures, but this reduction was more noticeable in the FRP decks than in the two concrete decks. The FRP decks fabricated by the pultrusion and VARTM processes showed significantly more deflection that either

Bridge No.	Deflection (mm) at location LV-2			Strain (micro-strains) at location SG-2		
	Low Temperature	High Temperature	Change %	Low Temperature	High Temperature	Change %
Bridge #1	2.05	2.17	5.9	231	248	7.8
Bridge #2	1.48	2.13	43.6	117	139	18.5
Bridge #3	3.28	3.48	6.2	534	574	7.6
Bridge #4	3.43	4.08	18.8	503	564	12.1
Bridge #5	2.18	2.42	10.9	391	446	14.3

Figure 1.6 - Deflections and Strains after 10 Million Cycles (Dutta, *et al.* 2003)

concrete deck panels. The FRP deck fabricated using the hand lay-up process showed only a slight change in deck stiffness when compared to the reinforced concrete deck panel. Dutta argues that the significant stiffness change with temperature implies that the deck stiffness was controlled mainly by temperature changes and not the number of applied load cycles.

The general conclusions Dutta drew from the results included: (a) a protocol for fatigue performance evaluation of FRP composite bridge deck panels was successfully completed under extreme temperatures, (b) the FRP panels were correlated with a conventional reinforced concrete bridge deck panel benchmark, (c) the load-deflection response or stiffness of the FRP composite decks were significantly affected by temperature, and (d) the progressive degradation in stiffness for the load cycling at the high temperature of 122 °F [50 °C] was observed, but a low temperature stiffness reduction under load cycling was not significant.

1.5.5. Low Temperature Response of Pultruded Composites at Saturation: Shao, Darchis 2007

Shao and Darchis state that most previous FRP composite research has focused on the tensile and compressive strength in the longitudinal direction, but that most failures of thin-walled composite structures is usually dominated by buckling which is a transverse dominated property. Therefore transverse properties E_{22}, F_{2t}, and F_{2c} are equally important in determining the buckling initiation and the post-buckling capacity. That paper documented three typical pultruded composites that were tested at six different exposure conditions: (a) dry for reference, (b) saturated in tap water at room temperature

for two years, (c) saturated then exposed to 100 freeze-thaw cycles between 41°F [5 °C] and 0 °F [-18 °C] (d) saturated then exposed to a 60 day continuous freeze at -11°F [-24 °C], (e) dry then exposed to 100 freeze-thaw cycles between 41 °F and 0 °F, (f) dry then exposed to a 60 day continuous freeze at -22 °F. Composites A and B were both commonly used for pultruded FRP beam flanges, and composite C was designed for the beam webs. Each composite was cut from a pultruded section in the longitudinal, transverse and 45° (off-axis) directions and then tensile and compressive tests were performed to determine the strength and stiffness in each direction. ASTM 3039 was used for the longitudinal and transverse tensile properties, and ASTM 3518M was used for the off-axis properties. ASTM D695 with modified end conditions was used to obtain the compressive properties of the composite laminates. Water absorption testes were conducted according to ASTM D570 using tap water at room temperature. Freeze-thaw cycling was conducted using an ASTM 666 chamber at a rate of 4.5 hours per cycle. All property tests were performed at room temperature; therefore there should have been no stiffening of the composites due to low temperatures. That study focused on the elastic moduli E_{11} and E_{22}, as well as the strengths F_{1t}, F_{1c}, F_{2t}, and F_{2c}. The effects of the environmental conditions on the longitudinal and transverse tensile modulus and the tensile strength can be seen in Figure 1.7 and Figure 1.8 respectively. The stiffness change under the various environmental conditions was not drastic, but the loss in ultimate strength was significant. Overall the saturated composite samples showed the most degradation in both longitudinal and transverse strength. It was also found that the freeze-thaw cycling degraded composite C significantly more than composites A or B.

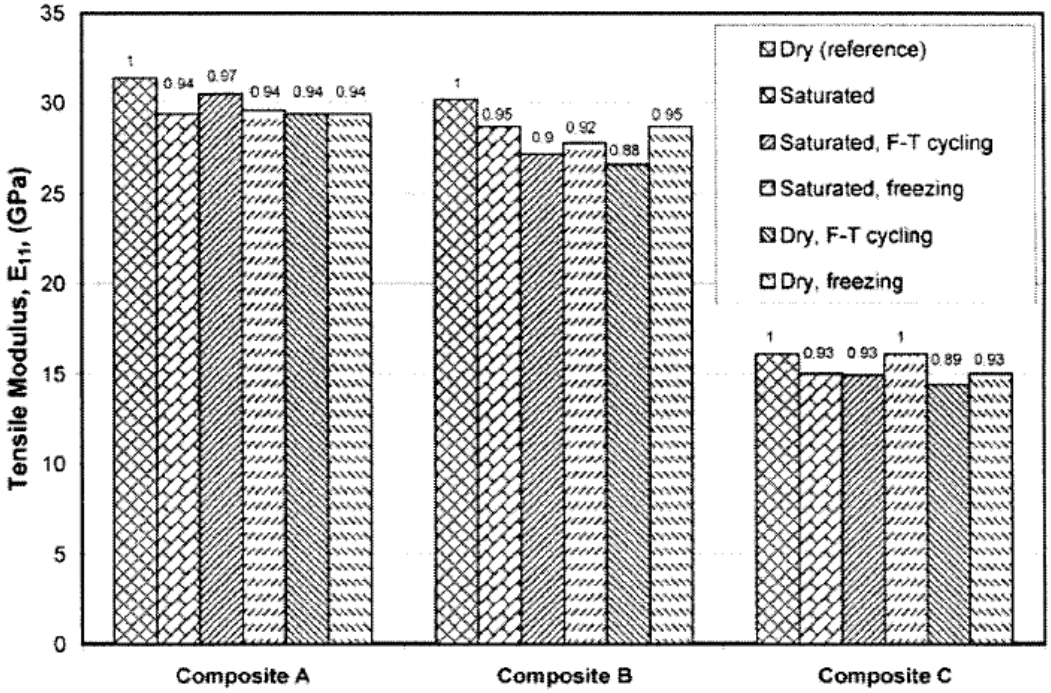

(A)

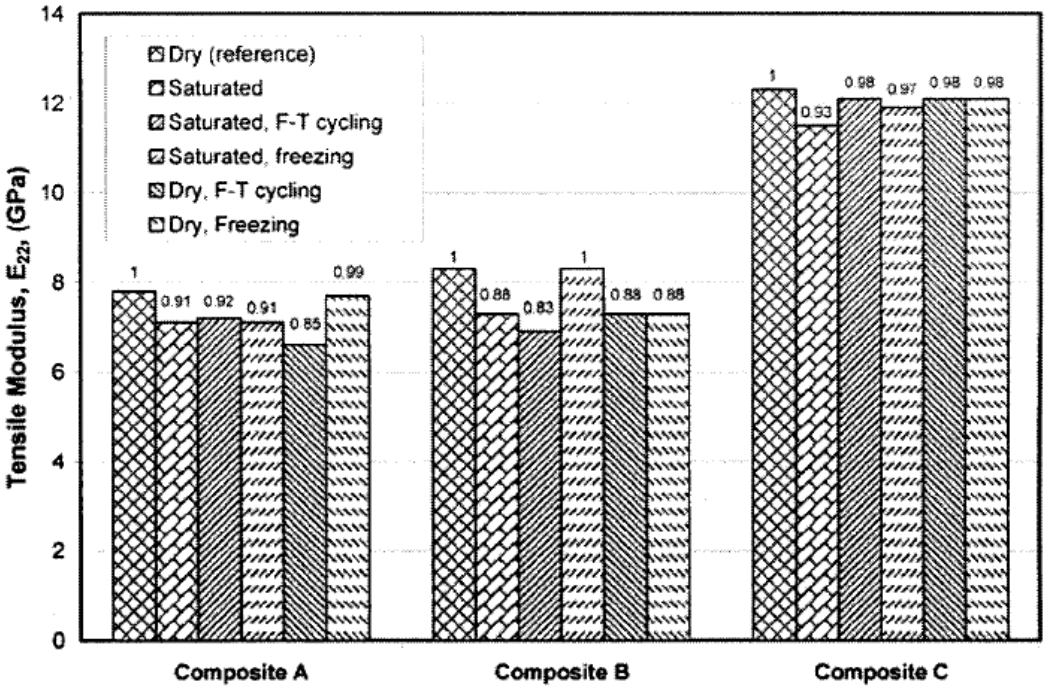

(B)

Figure 1.7 – Effects of Environmental Conditioning on the Tensile Modulus (A) longitudinal and (B) transverse directions. (Shao, Darchis 2007)

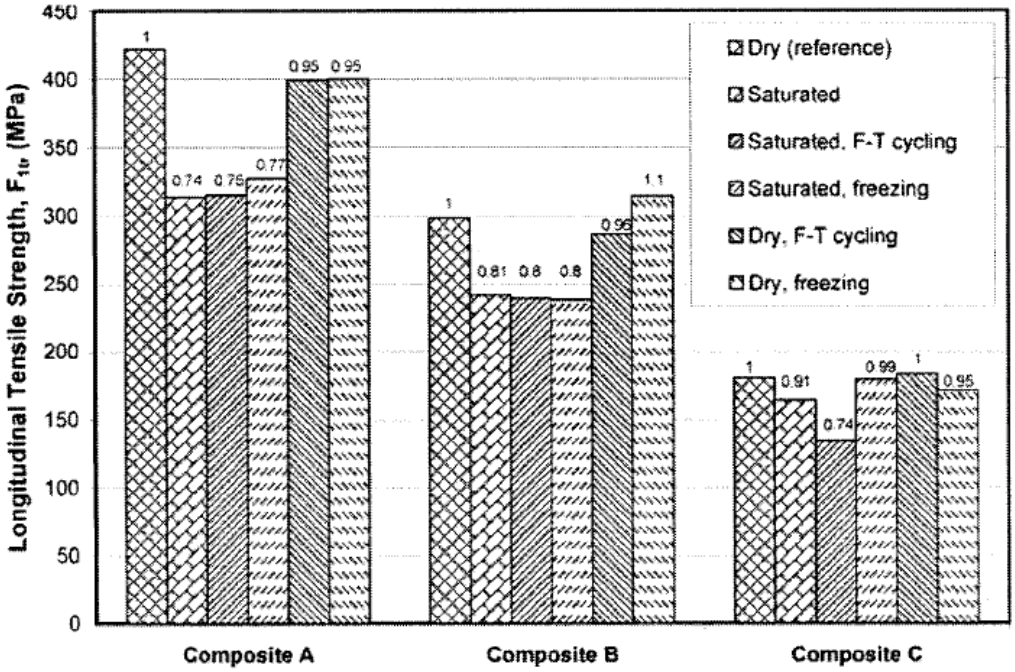

(A)

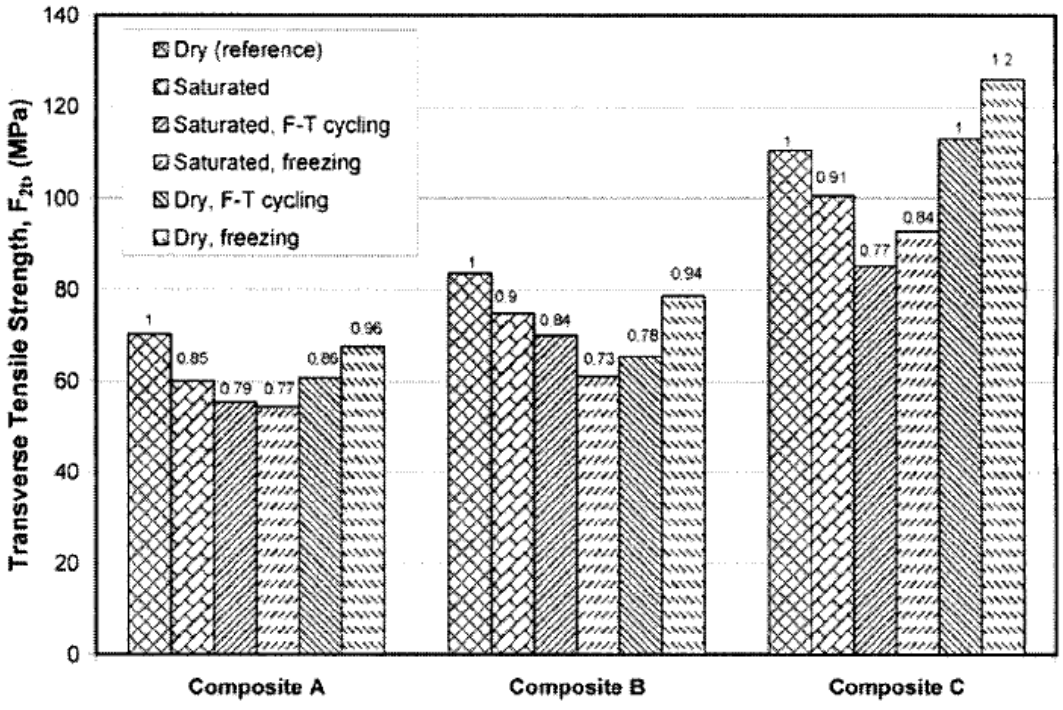

(B)

Figure 1.8 - Effects of Environmental Conditioning on the Tensile Strength (A) longitudinal and (B) transverse directions. (Shao, Darchis 2007)

Shao and Darchis also concluded that pultruded composites proved more resistant to freeze-thaw cycling and low temperature freezing than to moisture attack.

1.6. Scope of Work

After completing the above literature review, it is evident that the complex nature of FRP design as well as the numerous gaps in our knowledge and understanding of its behavior has severely limited its application within the construction industry. The low temperature knowledge of fiber-reinforced polymers is severely lacking and although strides have been made in researching its cold climate responses, a lack of comparable testing procedures and reproducible results has lead to confusion and a lack of confidence in applying them.

Therefore the goal of this thesis is twofold. The first goal is to present a single detailed theoretical analysis of a structural GFRP bridge deck panel. This analysis will introduce the reader to the basics of composite theory as well as some simplified procedures that can be used as warranted. The second goal of this thesis is to detail the procedures as well as the results of an experimental testing regiment that was meant to delve deeper into the material properties and behavior of GFRP composites at low temperatures. This experimental research will expound on findings from a previous low-temperature test conducted on a GFRP bridge deck panel fabricated by Kansas Structural Composites Inc. (KSCI) (Choppali, 2005).

1.7. Organization of Thesis

This thesis is organized as follows. Chapter 2 presents the theoretical analysis of a structural GFRP bridge deck panel. In Chapter 3 the experimental testing goals as well as the test setup and testing procedures will be presented. Chapter 4 will present and analyze the results obtained during the testing regiment. Conclusions and recommendations for future research will be presented in chapter 5.

CHAPTER 2

THEORETICAL ANALYSIS OF GFRP SANDWICH PANEL

2.1. Introduction

Fiber-reinforced polymer (FRP) composite materials have been used in numerous applications since the 1950's. While the use of FRP composites has grown to maturity in a few industrial applications (aerospace and marine industries), it has only been in the last 15-20 years that FRP composites have gained serious attention within the civil and structural industry. FRP materials potentially offer numerous advantages over conventional materials, such as a superior strength/weight ratio, a better stiffness/weight ratio, and a varying degree of corrosion resistance. These advantages are particularly attractive to the transportation industry because the nation's bridge system is currently undergoing significant rehabilitation, and the need for quick bridge replacement and repair is becoming an ever-increasing concern. The reduced weight for a comparable strength and stiffness allows many new construction and rehabilitation possibilities. For example it may be possible to increase the traffic load on a bridges existing superstructure by replacing the heavier existing bridge deck with a lightweight FRP alternative. Also the corrosion resistance of FRP composites could significantly help bridges plagued by steel corrosion due to saltwater, deicers, and other such chemicals. These advantages also come with some distinct drawbacks though. One of the primary drawbacks in the implementation of FRP composites is the inherent analysis and design

complexity. This chapter will attempt to tackle the complexity of FRP composites by leading the reader though the basic analysis of a GFRP bridge deck panel.

2.2. Description of GFRP Panel

To help clarity the plan of analysis it is necessary to understand the overall beam geometry. The GFRP beam type considered in this chapter is based on the GFRP bridge deck panels developed by Kansas Structural Composites Inc., Kansas (KSCI). The GFRP deck panels fabricated by KSCI have been analyzed through numerous experimental and numerical testing evaluations, one of which was conducted under cold environmental conditions by Usha Choppali and documented in her thesis ”Experimental Investigation of Fiber-Reinforced Polymer Composite Bridge Deck Panel in Cold Regions” (Choppali, 2005). The bridge panel consisted of glass fiber reinforced polymer (GFRP), and had an overall geometry of 7’ length, 13.4” width, and 7” thickness. Internal geometry of the panel consisted of two face sheets each with a thickness of 0.5”, and a 6” core consisting of sinusoidal cells of 2” amplitude, 4” wavelength”, and 0.1” wall thickness (Figure 2.1). The overall panel was sealed with a layer of 3.0 oz chopped strand mat (CSM) for protection. The sinusoidal core while similar to traditional honeycomb sandwich construction was designed for increased stiffness, buckling response, and in particular ease of fabrication. The constituent materials used in the sandwich panel (both face laminates and core) consist of E-glass fibers, and polyester resin. The general material properties for the constituent materials are listed in Table 2.1 (Altenbach, et al. 2004).

2.3. Modeling Overview and Reference Systems

Successful modeling of fiber-reinforced composite structures requires an understanding of the micro-structural, micro-mechanical as well as the macro-mechanical properties involved. The following generalized procedure will begin at the constituent level then will build to the lamina level, laminate level and finally end with the overall sandwich beam geometry described in section **Error! Reference source not found.**. At that point we will look at the various stresses and strains throughout the beam, laminate, and lamina resulting from an arbitrary load on the beam. For a better understanding of the subsequent procedures and results it is advantageous to create separate global and local reference systems. For the global reference system we will use the subscript 1, 2, 3 for the longitudinal (beam

Table Error! No text of specified style in document.**.1 - Material Properties of Constituent Materials**

Material	Elastic Modulus E, [x10^6 psi]	Shear Modulus G, [x10^6 psi]	Poisson's Ratio v	Density ρ, [lb/in^3]
E-Glass Fiber	10.5	4.38	0.2	0.09176
Polyester Resin	0.522	0.196	0.33	0.04516

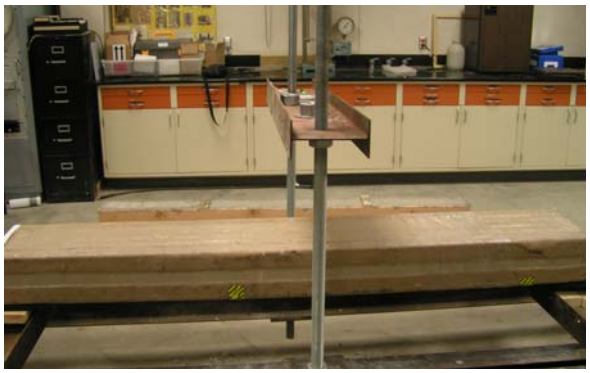

(A)

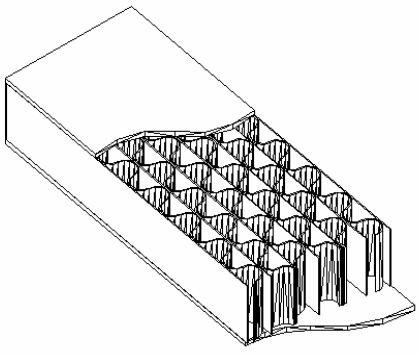

(B)

length), transverse (beam width), and vertical (beam height) directions respectively, and the subscripts 4, 5, 6 or 23, 13, 12 for the $\{x_2 - x_3\}$ (cross-section), $\{x_1 - x_3\}$ (profile), and $\{x_1 - x_2\}$ (plan) planes respectively. The local reference system will be used primarily for thin plane sections typically in the $(x_1 - x_2)$ plane and for the constituent materials, therefore we are primarily interested in the longitudinal and transverse directions, which will be subscripted by L, or T respectively or hyphenated when using the global reference syntax. For example σ_T and σ'_2 are the same but may not be the same as σ_2 (Figure 2.2).

2.4. Modeling the Microstructure Geometry

The microstructure of a ply or lamina within the GFRP panel consists of four fiber lay-up arrangements: (1) unidirectional layer of fiber bundles. (2) bi-directional stitched fabrics (SF) which in our case include equal off-angle unidirectional fibers (0°/90°).

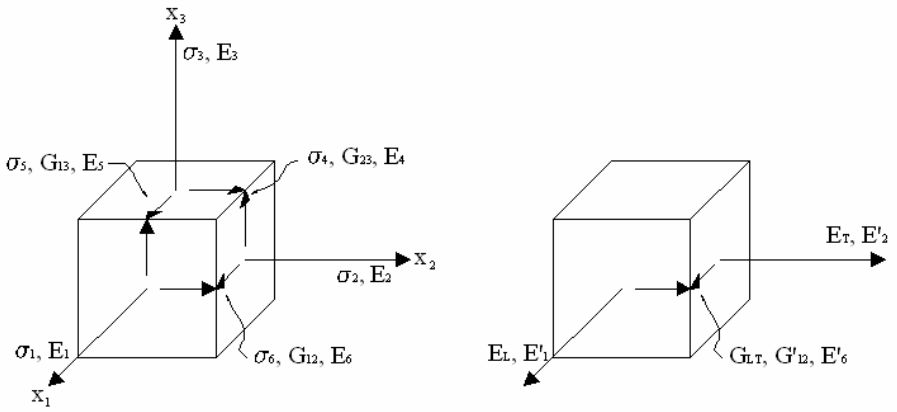

Figure 2.2 - Reference System Syntax
(A) Global reference system, (B) Local reference system

(3) Chopped Strand Mat (ChopSM), which is made of short non-continuous randomly orientated fibers giving nearly isotropic in-plane properties. (4) Continuous Strand Mat (ContSM) which is made of continuous randomly orientated fibers; this is a typical backing material for non-woven fibers and has characteristics similar to ChopSM.

In this analysis the ContSM backing layers will be neglected due to small relative strength and thickness. Also the bidirectional SF will be modeled as two layers of unidirectional fibers for ease of calculation. The top face sheet lay-up is shown in Figure 2.3 (Plunkett, 2006), and is symmetric for the bottom face sheet.

2.4.1. General Assumptions

A triclinic (three axes are unequal and intersect at oblique angles) anisotropic material based on the generalized three-dimensional Hooke's law theoretically would have 21 independent material constants. Due to the difficulty of dealing with that many constants it is necessary to make valid assumptions in order to reduce the number of independent material constants. If one plane of symmetry (Monoclinic) is assumed then the independent material constants are reduced down to 13. In our case each lamina

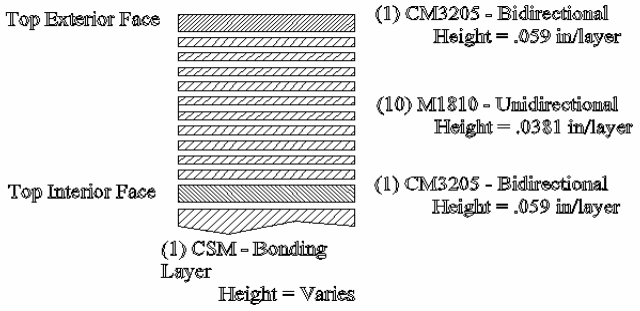

Figure 2.3 - Lay-up of the Face Sheets

behaves more like an orthotropic material, one axis along the longitudinal fiber direction and the other two transverse or orthogonal to the fibers. This yields just 9 independent material constants. By observing the behavior of the lamina when subjected to various loads it can be seen that the fibers contribute a large part of the stiffness when the lamina is subjected to a longitudinal load, but the resin or bonding matrix contributes most of the stiffness when the lamina is subjected to a transverse load. The resin by itself has an isotropic material behavior and therefore all material properties orthogonal to the fiber direction are essentially the same. This material behavior is transversely isotropic, with an axis in the fiber direction and an assumed isotropic behavior in the orthogonal cross-section. The independent material constants have now been reduced down to 5. Using the global reference syntax the fibers will be placed in the x_1 direction and the plane of isotropy will be in the ($x_2 - x_3$) plane. The 5 material constants E_1, E_2, G_{12}, ν_{12}, and G_{23} are related as shown,

$$E_1, \quad E_2 = E_3, \quad E_5 = G_{13} = G_{12} = E_6$$

$$\nu_{12} = \nu_{13}, \quad E_4 = G_{23} = \frac{E_2}{2 \cdot (1 + \nu_{23})}$$

Because each lamina is thin and is very weak in the vertical direction we make the assumption that out-of-plane shear forces are essentially zero and therefore we can neglect G_{23} (Altenbach, et al. 2004). This leaves only E_1, E_2, G_{12}, and ν_{12}, or in local reference syntax E_L, E_T, G_{LT}, and ν_{LT}.

Table 2.2 - Layer Properties of Each Lamina

Ply Name	Resin Type	Fiber weight [lb]	Resin Weight [lb]	Fiber Volume, V_f
CSM	Polyester	0.75	1	0.270
Bidirectional (cm3205) $_{0°}$	Polyester	1	0.75	0.396
Unidirectional(m1810)	Polyester	0.75	0.75	0.330

2.4.2. Fiber Volume Fraction

The properties of the individual lamina in a composite material are dependant on the amount of fibers used; this can be quantified using a relative fiber volume fraction (V_f) and matrix volume fraction (V_m). For a lamina V_f and V_m can be determined from,

$$V_f = \frac{\frac{\omega_f}{\rho_f}}{\frac{\omega_f}{\rho_f} + \frac{\omega_m}{\rho_m}} \qquad \text{(Equ. 2.1)}$$

$$V_m = \left(1 - V_f\right) \qquad \text{(Equ. 2.2)}$$

respectively where ω_f, and ω_m are the weight of the fibers and the matrix respectively, also ρ_f, and ρ_m are the density of the fibers and the matrix respectively. The weights and the fiber volume for each lamina in our beam are listed in Table 2.2.

2.4.3. Effective Elastic Lamina Properties

The elastic properties of each ply or lamina can be approximated using effective material properties obtained through micro-mechanical modeling. In essence micro-mechanical modeling correlates the constituent properties to the average effective

Table 2.3 - Effective Elastic Properties of Each Lamina

Ply Name/Type	Orientation	E_L, [x10^6 psi]	E_T, [x10^6 psi]	G^l_{LT}, [x10^6 psi]	v_{LT}	v_{TL}
CSM	Polyester	1.444	1.444	0.324	0.295	0.295
Bidirectional (cm3205) $_{0°}$	Polyester	4.473	0.837	0.418	0.279	0.052
Unidirectional(m1810)	Polyester	3.815	0.760	0.365	0.287	0.057

composite properties for each lamina. This paper will use the elementary rule of mixtures model although there are other more detailed models available such as periodic microstructure, and composite cylinders (Davalos, 2001). An example for determining the fiber volume fraction as well as the effective material properties for the E-glass/polyester material of interest can be found in Appendix 2.1, and the results are listed in Table 2.3.

2.4.3.1. Effective longitudinal modulus

When a unidirectional lamina is loaded parallel to the fibers, it can be assumed that the fiber and matrix strains are in parallel and therefore the same (ie. Iso-strain condition). By using Hooke's law for the fiber, the matrix, as well as the composite it is a simple matter to find the effective longitudinal modulus. The modulus is obtained simply by adding together the constituent properties in the proper ratio, as in the following equations:

$$\sigma_L = E_L \cdot \varepsilon_L, \qquad E_L = \frac{\sigma_L}{\varepsilon_L}$$

$$\sigma_L = V_f \cdot \sigma_{Lf} + V_m \cdot \sigma_{Lm} = V_f \cdot E_{Lf} \cdot \varepsilon_{Lf} + V_m \cdot E_{Lm} \cdot \varepsilon_{Lm} = V_f \cdot E_{Lf} \cdot \varepsilon_L + V_m \cdot E_{Lm} \cdot \varepsilon_L$$

$$\therefore E_L = \frac{\sigma_L}{\varepsilon_L} = E_f V_f + E_m \left(1 - V_f\right) \qquad \text{(Equ. 2.3)}$$

This concept can be expanded to include fiber orientations other than unidirectional by incorporating an appropriate correction factor (Zenkert, 1995),

$$E_L = \eta_L \eta_0 E_f V_f + E_m \left(1 - V_f\right) \qquad \text{(Equ. 2.4)}$$

where η_0 corrects for fiber orientation:

Uni-axial fibers	$\eta_0 = 1$
Equal Bidirectional woven fibers	$\eta_0 = .5$
Random in-plane (CSM)	$\eta_0 = .375$

As previously stated the bidirectional layers will be modeled as two half thickness unidirectional layers, so no correction is needed. It should also be noted that the effective longitudinal and the transverse moduli for CSM materials are the same because they are considered isotropic.

2.4.3.2. Effective transverse modulus

The micro-mechanical model for the effective transverse modulus of a unidirectional lay-up includes a fiber/matrix arrangement that acts in series when loaded. In other words when the lamina is subjected to a transverse load the stress is constant through the lamina and therefore the constituent materials are in a state of equal stress (ie. Iso-stress condition). The effective transverse modulus for a unidirectional layer is obtained by,

$$\sigma_T = E_T \cdot \varepsilon_T , \qquad \frac{1}{E_T} = \frac{\varepsilon_T}{\sigma_T}$$

$$\varepsilon_T = V_f \cdot \varepsilon_{Tf} + V_m \cdot \varepsilon_{Tm} = V_f \cdot \frac{\sigma_{Tf}}{E_{Tf}} + V_m \cdot \frac{\sigma_{Tm}}{E_{Tm}} = V_f \cdot \frac{\sigma_T}{E_{Tf}} + V_m \cdot \frac{\sigma_T}{E_{Tm}}$$

$$\frac{\varepsilon_T}{\sigma_T} = \frac{1}{E_T} = \frac{V_f}{E_{Tf}} + \frac{V_m}{E_{Tm}}$$

$$\therefore \frac{1}{E_T} = \frac{V_f}{E_f} + \frac{\left(1 - V_f\right)}{E_m} \qquad \text{(Equ. 2.5)}$$

2.4.3.3. Effective Poisson's ratio

The effective major Poisson's ratio of the composite material is obtained by using the previously developed longitudinal and transverse models (both iso-strain, and iso-stress). Also the effective minor Poisson's ratio can be obtained through symmetry based on its reciprocal relationship to the major Poisson's ratio. The major Poisson's ratio is obtained by,

$$\nu = -\frac{\varepsilon_T}{\varepsilon_L} , \qquad \varepsilon_T = -\nu \cdot \varepsilon_L$$

$$\varepsilon_T = V_f \cdot \varepsilon_{Tf} + V_m \cdot \varepsilon_{Tm} = -\left(V_f \cdot \nu_f \cdot \varepsilon_{Lf}\right) - \left(V_m \cdot \nu_m \cdot \varepsilon_{Lm}\right) = -\left(V_f \cdot \nu_f \cdot \varepsilon_L\right) - \left(V_m \cdot \nu_m \cdot \varepsilon_L\right)$$

$$-\frac{\varepsilon_T}{\varepsilon_L} = \nu_{LT} = \left(V_f \cdot \nu_f\right) + \left(V_m \cdot \nu_m\right)$$

$$\therefore \nu_{LT} = \nu_{TL} \cdot \frac{E_L}{E_T} = \left(\nu_f \cdot V_f + \nu_m \cdot \left(1 - V_f\right)\right) \qquad \text{(Equ. 2.6)}$$

2.4.3.4. Effective In-plane shear modulus

The micro-mechanical model used to determine the in-plane shear modulus involves subjecting a lamina to a pure shear stress. Ideally the shear stresses should be the same on both the fiber and the matrix, while the shear strains will vary between materials. Therefore the material is once again under a parallel model (Iso-stress condition). The effective in-plane shear modulus can be determined by,

$$\tau = \gamma \cdot G_{LT}, \quad \gamma = \frac{\tau}{G_{LT}}, \quad G_{LT} = \frac{\tau}{\gamma}$$

$$\gamma = \gamma_f \cdot V_f + \gamma_m \cdot V_m = \left(\frac{\tau}{G_{LTf}}\right) \cdot V_f + \left(\frac{\tau}{G_{LTm}}\right) \cdot V_m$$

$$\frac{\gamma}{\tau} = \frac{1}{G_{LT}} = \left(\frac{V_f}{G_{LTf}}\right) + \left(\frac{V_m}{G_{LTm}}\right)$$

$$\therefore \frac{1}{G_{LT}} = \frac{V_f}{G_{LTf}} + \frac{\left(1 - V_f\right)}{G_{LTm}} \qquad \text{(Equ. 2.7)}$$

Although the rule of mixture for effective longitudinal modulus, transverse modulus, and Poisson's ratio generally yields results that are comparable to experimental values, it does not give very accurate results for the effective in-plane shear modulus. A solution based on an elasticity model for a cylindrical elementary cell subjected to tension gives much better results, and should be used instead (Altenbach, et al. 2004). The improved effective in-plane shear modulus is given below without any detailed derivation,

$$G_{LT} = G_{LTm} \cdot \left(\frac{G_{LTf} \cdot \left(1 + V_f\right) + G_{LTm} \cdot \left(1 - V_f\right)}{G_{LTf} \cdot \left(1 - V_f\right) + G_{LTm} \cdot \left(1 + V_f\right)} \right) \qquad \text{(Equ. 2.8)}$$

2.5. Elastic Lamina Behavior

Now that the effective elastic properties for each lamina have been defined, it is necessary to develop the behavior of the individual lamina. The macro-mechanical modeling of a lamina is based on an assumed homogeneous behavior using the effective material properties obtained through the micro-mechanical model, or through experimentation. Also of the six components of stress within the material, three are considered to be much smaller then the rest. In particular the in-plane stresses σ'_1, σ'_2 and τ'_6 are much greater than the out-of-plane stresses σ'_3, τ'_4 and τ'_5, which are essentially zero leaving us with a plane stress condition. It should be noted that although the out-of-plane stresses are essentially zero the out-of-plane strains are not necessarily zero, and may need to be taken into account (Altenbach, et al. 2004).

If a lamina is subjected to an on-axis axial load then the axial stresses and strains do not affect on-axis shear stresses and strains and vise versa. Therefore the relationship between local stresses and local strains can be seen in the following on-axis or reduced lamina stiffness matrix,

$$\begin{bmatrix} \sigma'_1 \\ \sigma'_2 \\ \sigma'_6 \end{bmatrix} = \begin{bmatrix} Q'_{11} & Q'_{12} & 0 \\ Q'_{12} & Q'_{22} & 0 \\ 0 & 0 & Q'_{66} \end{bmatrix} \cdot \begin{bmatrix} \varepsilon'_1 \\ \varepsilon'_2 \\ \varepsilon'_6 \end{bmatrix} \qquad \text{(Equ. 2.9)}$$

where,

$$Q_{11}^{'} = \frac{E_L^{'}}{\left(1 - \nu_{LT}^{'} \cdot \nu_{TL}^{'}\right)}, \qquad Q_{22}^{'} = \frac{E_T^{'}}{\left(1 - \nu_{LT}^{'} \cdot \nu_{TL}^{'}\right)}$$

$$Q_{66}^{'} = E_6^{'} = G_{LT}^{'}, \qquad Q_{12}^{'} = \frac{E_T^{'} \cdot \nu_{LT}^{'}}{\left(1 - \nu_{LT}^{'} \cdot \nu_{TL}^{'}\right)}$$

It can be seen that the longitudinal and the transverse stresses and strains are now coupled, but the shear stresses and principle stresses remain uncoupled. It is important to note that although we are using the global reference syntax, we are still dealing with local orientations. Laminates are generally constructed by stacking together numerous laminas of various fiber orientations therefore it is necessary for us to reorient each lamina to the global coordinates system (Figure 2.4). This can be accomplished by using the reduced stiffness transformation matrix shown below,

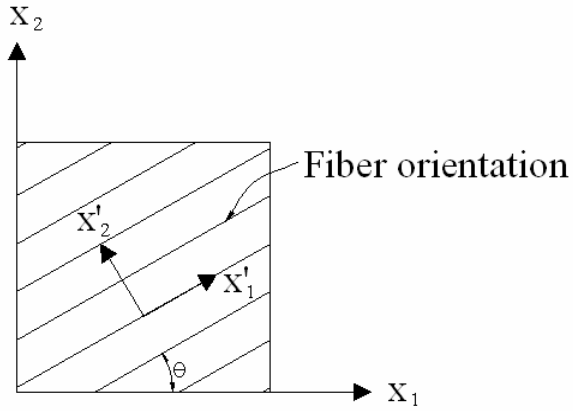

Figure 2.4 - Global and Local Axis Orientation

$$\begin{bmatrix} Q_{11} \\ Q_{12} \\ Q_{16} \\ Q_{22} \\ Q_{26} \\ Q_{66} \end{bmatrix} = \begin{bmatrix} c^4 & 2\cdot c^2\cdot s^2 & s^4 & 4\cdot c^2\cdot s^2 \\ c^2\cdot s^2 & c^4+s^4 & c^2\cdot s^2 & -4\cdot c^2\cdot s^2 \\ c^3\cdot s & -c\cdot s\cdot\left(c^2-s^2\right) & -c\cdot s^3 & -2\cdot c\cdot s\cdot\left(c^2-s^2\right) \\ s^4 & 2\cdot c^2\cdot s^2 & c^4 & 4\cdot c^2\cdot s^2 \\ c\cdot s^3 & c\cdot s\cdot\left(c^2-s^2\right) & -c^3\cdot s & 2\cdot c\cdot s\cdot\left(c^2-s^2\right) \\ c^2\cdot s^2 & -2\cdot c^2\cdot s^2 & c^2\cdot s^2 & \left(c^2-s^2\right)^2 \end{bmatrix} \cdot \begin{bmatrix} Q'_{11} \\ Q'_{12} \\ Q'_{22} \\ Q'_{66} \end{bmatrix} \quad \text{(Equ. 2.10)}$$

where,

$$c = \cos(\theta), \quad s = \sin(\theta)$$

The Q_{16} and Q_{26} terms are added due to shear coupling, they will remain zero if the lamina's local fiber orientation is parallel or perpendicular to the global principle axes ($\theta = 0°, 90°$), but will be non-zero for an off-axis orientation ($\theta \neq 0°, 90°$). Now due to shear coupling the axial stresses and strains do affect shear stresses and strains which can be seen in the standard lamina stiffness matrix,

$$\begin{bmatrix} \sigma_1 \\ \sigma_2 \\ \sigma_6 \end{bmatrix} = \begin{bmatrix} Q_{11} & Q_{12} & Q_{16} \\ Q_{12} & Q_{22} & Q_{26} \\ Q_{16} & Q_{26} & Q_{66} \end{bmatrix} \cdot \begin{bmatrix} \varepsilon_1 \\ \varepsilon_2 \\ \varepsilon_6 \end{bmatrix} \quad \text{(Equ. 2.11)}$$

The creation of the reduced lamina stiffness matrix as well as the standard lamina stiffness matrix for various E-glass/polyester lamina orientations can be found in an example in Appendix 2.2, and the results are listed in Table 2.4.

Although the stiffness matrixes [Q] and [Q'] provide lamina stresses for given lamina strains, due to the principles of matrix multiplication it is inadequate to provide lamina strains under given stresses. To do this it is advantageous to introduce the compliance matrix [S] and [S'] where $[S]=[Q]^{-1}$ and $[S']=[Q']^{-1}$, where,

Table 2.4 - Local and Gloabal Stiffness Matrices for Each Lamina

	Bidirectional $(cm3205)_{0°}$ [x10^6 psi]		Bidirectional $(cm3205)_{90°}$ [x10^6 psi]		Unidirectional(m1810) [x10^6 psi]	
	Local	Global	Local	Global	Local	Global
θ [°]	---	0	---	90	---	0
Q_{11}	4.539	4.539	4.539	0.849	3.878	3.878
Q_{12}	0.237	0.237	0.237	0.237	0.222	0.222
Q_{16}	---	0.000	---	0.000	---	0.000
Q_{22}	0.849	0.849	0.849	4.539	0.773	0.773
Q_{26}	---	0.000	---	0.000	---	0.000
Q_{66}	0.418	0.418	0.418	0.418	0.365	0.365

$$\begin{bmatrix} \varepsilon_1 \\ \varepsilon_2 \\ \varepsilon_6 \end{bmatrix} = \begin{bmatrix} S_{11} & S_{12} & S_{16} \\ S_{12} & S_{22} & S_{26} \\ S_{16} & S_{26} & S_{66} \end{bmatrix} \cdot \begin{bmatrix} \sigma_1 \\ \sigma_2 \\ \sigma_6 \end{bmatrix} \qquad \text{(Equ. 2.12)}$$

$$\begin{bmatrix} \varepsilon_1' \\ \varepsilon_2' \\ \varepsilon_6' \end{bmatrix} = \begin{bmatrix} S_{11}' & S_{12}' & 0 \\ S_{12}' & S_{22}' & 0 \\ 0 & 0 & S_{66}' \end{bmatrix} \cdot \begin{bmatrix} \sigma_1' \\ \sigma_2' \\ \sigma_6' \end{bmatrix} \qquad \text{(Equ. 2.13)}$$

It should also be noted that it is possible to reorient the local or global stresses and strains without using the reduced stiffness transformation matrix. With the transformations given below it should be possible to obtain any desired stress or strain in the lamina for either the local or global coordinate system when given the appropriate information,

$$\begin{bmatrix} \varepsilon_1' \\ \varepsilon_2' \\ \varepsilon_6' \end{bmatrix} = \begin{bmatrix} c^2 & s^2 & s \cdot c \\ s^2 & c^2 & -s \cdot c \\ -2 \cdot s \cdot c & 2 \cdot s \cdot c & c^2 - s^2 \end{bmatrix} \cdot \begin{bmatrix} \varepsilon_1 \\ \varepsilon_2 \\ \varepsilon_6 \end{bmatrix} \qquad \text{(Equ. 2.14)}$$

$$\begin{bmatrix} \varepsilon_1 \\ \varepsilon_2 \\ \varepsilon_6 \end{bmatrix} = \begin{bmatrix} c^2 & s^2 & -s \cdot c \\ s^2 & c^2 & s \cdot c \\ 2 \cdot s \cdot c & -2 \cdot s \cdot c & c^2 - s^2 \end{bmatrix} \cdot \begin{bmatrix} \varepsilon_1' \\ \varepsilon_2' \\ \varepsilon_6' \end{bmatrix} \qquad \text{(Equ. 2.15)}$$

And,

$$\begin{bmatrix} \sigma_1' \\ \sigma_2' \\ \sigma_6' \end{bmatrix} = \begin{bmatrix} c^2 & s^2 & 2 \cdot s \cdot c \\ s^2 & c^2 & -2 \cdot s \cdot c \\ -s \cdot c & s \cdot c & c^2 - s^2 \end{bmatrix} \cdot \begin{bmatrix} \sigma_1 \\ \sigma_2 \\ \sigma_6 \end{bmatrix} \qquad \text{(Equ. 2.16)}$$

$$\begin{bmatrix} \sigma_1 \\ \sigma_2 \\ \sigma_6 \end{bmatrix} = \begin{bmatrix} c^2 & s^2 & -2 \cdot s \cdot c \\ s^2 & c^2 & 2 \cdot s \cdot c \\ s \cdot c & -s \cdot c & c^2 - s^2 \end{bmatrix} \cdot \begin{bmatrix} \sigma_1' \\ \sigma_2' \\ \sigma_6' \end{bmatrix} \qquad \text{(Equ. 2.17)}$$

where,

$$c = \cos(\theta), \qquad s = \sin(\theta)$$

2.6. Elastic Laminate Behavior

The previous section developed the stress-strain relationships for a single lamina, but now our macro-mechanical model must be expanded to include the contribution of each lamina within a laminate to the overall laminate behavior. The assumptions for this new model include: (1) no slipping between lamina, (2) each lamina is homogeneous and has it's own material properties, and (3) the strains and displacements are continuous throughout the laminate, and vary linearly though the laminate thickness.

A brief note on laminate stacking codes should be added to help simplify lay-up sequencing. The top face sheet of the deck panel of interest as shown in Figure 2.3, would be denoted as [0/90/0/0/0/0/0/0/0/0/0/0/0/90/0]. The first [0/90] denotes the bidirectional layer, followed by ten unidirectional layers [0] and finally the bottom bidirectional layer [90/0]. This can be shortened to $[0/90/0/0/0/0/0]_s$, where the s subscript means that the laminate is symmetric about itself.

The assumption that the strains are linear through the laminate thickness means that the total strain is a sum of both axial strain (ε_a) and flexural strain ($x_3 \cdot \kappa$), in other words, $\varepsilon_{(x_1,x_3)} = \varepsilon_{a\,(x_1)} + x_3 \cdot \kappa_{(x_1)}$, where $\kappa_{(x_1)}$ is the curvature vector. A summation of the resulting in-plane stresses throughout a cross-section of the laminate will result in an in-plane force vector (N), and similarly a summation of the stress moments due to the in-plane forces will result in a moment vector (M), see Figure 2.5. The relationship between these resultant forces and moments and the corresponding axial and flexural strains can be shown in the generalized matrix,

$$\begin{bmatrix} N \\ M \end{bmatrix} = \begin{bmatrix} A & B \\ B & D \end{bmatrix} \cdot \begin{bmatrix} \varepsilon_a \\ \kappa \end{bmatrix}, \qquad \text{(Equ. 2.18)}$$

$$\begin{bmatrix} \varepsilon_a \\ \kappa \end{bmatrix} = \begin{bmatrix} a & b \\ c & d \end{bmatrix} \cdot \begin{bmatrix} N \\ M \end{bmatrix}, \qquad \text{(Equ. 2.19)}$$

where,

$$\begin{bmatrix} a & b \\ c & d \end{bmatrix} = \begin{bmatrix} A & B \\ C & D \end{bmatrix}^{-1} \qquad \text{(Equ. 2.20)}$$

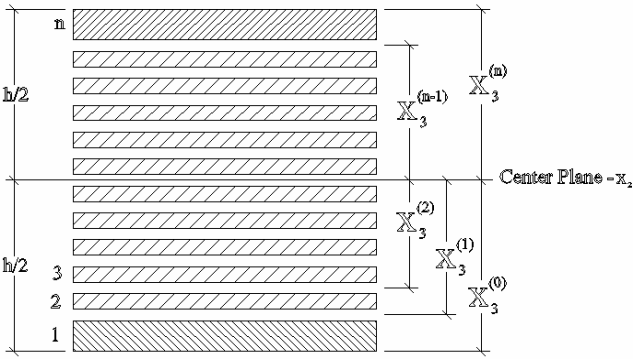

Figure 2.5 - General Laminate Lay-up and Reference Syntax

and where *A*, *B*, and *D* are the extensional, coupling, and flexural stiffness matrixes, while *a*, *b*, *d* are the extensional, coupling, and flexural elasticity matrixes. If a laminate has a symmetric lay-up then the coupling matrix [B] and [b] are both zero meaning that axial force does not cause flexural strains, and vice versa. An expanded [ABD] matrix can be seen below:

$$\begin{bmatrix} N_1 \\ N_2 \\ N_6 \\ \cdots \\ M_1 \\ M_2 \\ M_6 \end{bmatrix} = \begin{bmatrix} A_{11} & A_{12} & A_{16} & \vdots & B_{11} & B_{12} & B_{16} \\ A_{12} & A_{22} & A_{26} & \vdots & B_{12} & B_{22} & B_{26} \\ A_{16} & A_{26} & A_{66} & \vdots & B_{16} & B_{26} & B_{66} \\ \cdots & \cdots & \cdots & \cdots & \cdots & \cdots & \cdots \\ B_{11} & B_{12} & B_{16} & \vdots & D_{11} & D_{12} & D_{16} \\ B_{12} & B_{22} & B_{26} & \vdots & D_{12} & D_{22} & D_{26} \\ B_{16} & B_{26} & B_{66} & \vdots & D_{16} & D_{26} & D_{66} \end{bmatrix} \cdot \begin{bmatrix} \varepsilon_{a1} \\ \varepsilon_{a2} \\ \varepsilon_{a6} \\ \cdots \\ \kappa_1 \\ \kappa_2 \\ \kappa_6 \end{bmatrix}$$

where,

$$A_{ij} = \sum_{k=1}^{n} Q_{ij}^{(k)} \cdot \left(x_3^{(k)} - x_3^{(k-1)} \right) = \sum_{k=1}^{n} Q_{ij}^{(k)} \cdot h^{(k)} \qquad i, j = 1, 2, 6 \qquad \text{(Equ. 2.21)}$$

$$B_{ij} = \frac{1}{2} \cdot \sum_{k=1}^{n} Q_{ij}^{(k)} \cdot \left(x_3^{(k)^2} - x_3^{(k-1)^2} \right) = \sum_{k=1}^{n} Q_{ij}^{(k)} \cdot \bar{x}_3^{(k)} \cdot h^{(k)} \qquad i, j = 1, 2, 6 \qquad \text{(Equ. 2.22)}$$

$$D_{ij} = \frac{1}{3} \cdot \sum_{k=1}^{n} Q_{ij}^{(k)} \cdot \left(x_3^{(k)^3} - x_3^{(k-1)^3} \right) = \sum_{k=1}^{n} Q_{ij}^{(k)} \cdot h^{(k)} \cdot \left(\bar{x}_3^{(k)^2} + \frac{h^{(k)^2}}{12} \right) i, j = 1, 2, 6 \qquad \text{(Equ. 2.23)}$$

It should be noted that the [D] and [B] matrixes are dependant on the axis of bending similar to the moment of inertia. An example of creating the [ABD] constitutive matrix for the E-glass/polyester face sheet laminate in the deck panel has been provided in Appendix 2.3, and the results can be found in Table 2.5

Table 2.5 - ABD Matrix for Top and Bottom Face Sheets

Axial Stiffness	Coupling Stiffness	Flexural Stiffness
[x10^6 psi]	[x10^6 psi]	[x10^6 psi]
A_{11} = 1.796	B_{11} = 0.000	D_{11} = 0.035
A_{12} = 0.112	B_{12} = 0.000	D_{12} = 0.002
A_{16} = 0.000	B_{16} = 0.000	D_{16} = 0.000
A_{22} = 0.612	B_{22} = 0.000	D_{22} = 0.018
A_{26} = 0.000	B_{26} = 0.000	D_{26} = 0.000
A_{66} = 0.188	B_{66} = 0.000	D_{66} = 0.004

2.7. Sandwich Panel Behavior

Now that the behavior of an individual laminate has been determined, it is necessary to add the sandwich panel geometry into the mechanical model. Sandwich composites are a special group of laminated composites used in engineering applications. Sandwich panels consist of typically thin face sheets sandwiching a core. It can be seen by looking at the relative axial and flexural stiffness shown in Table 2.5, that the face sheets are orders of magnitude stiffer under in-plane axial loads than out-of-plane flexural loads due to their typically thin geometries. For this reason the faces should be situated at locations of maximum in-plane stress, which happen to be the top and bottom surface for beam or plate bending. The earlier assumption stating the lamina's out of plane shear stiffness is essentially zero still holds. While a more complicated micro-mechanical model accounting for this out-of-plane shear strength can be adopted, the shear strength tends to be small. Also because the beam center is generally the location of maximum shear stress it is simpler to allow the core to resist the out-of-plane shear forces alone. Although cores need to be stiff for out-of-plane shear forces, they are typically weak under in-plane stresses. Therefore the assumptions used for our mechanical model are:

(1) the thickness of the core is much greater than the thickness of the faces, (2) strains are linear over the thickness [$\varepsilon_{(x_1,x_3)} = \varepsilon_{a\,(x_1)} + x_3 \cdot \kappa_{(x_1)}$], (3) the faces only resist in-plane stresses, (4) the core only resist out-of-plane shear stresses, and (5) vertical strain in both faces and core is essentially zero.

2.7.1. Modeling Sinusoidal Core

Based on the previous assumptions the core alone resists the out-of-plane shear forces within a sandwich panel. It is typically fairly simple to develop equivalent elastic properties for a solid homogeneous core, but the core geometry within the panel currently under investigation is a more complicated periodic design composed of sinusoidal honeycomb cells. The sinusoidal honeycomb core consists of alternating vertical straight flats and vertical sinusoidal flutes, and therefore requires a more detailed approach. The equivalent elastic properties for this periodic structure are based on an analysis combining both energy methods and mechanics of materials. A complete walkthrough of this analysis would be overly complicated and beyond the scope of this thesis, but can be found in Davalos' paper "Modeling and Characterization of fiber-reinforced plastic honeycomb sandwich panels for highway bridge applications". A simplified procedure based on Davalos' results is explained below.

The honeycomb core geometry can be found in Figure 2.6.A, where t_1 is the thickness of the vertical flats, t_2 is the thickness of the vertical flutes, h is the sinusoidal amplitude, L is the wavelength, and H is the overall thickness of the repeating periodic structure. To help simplify the procedure the sinusoidal wave will be replaced with a

triangular section as shown in Figure 2.6.B. The general equations based on Davalos' procedure are,

$$G_{13} = G_{12}^{core}\left(\frac{2\cdot t_1}{H} + \frac{4\cdot t_2}{H\cdot L}\int_0^s \cos^2\theta\cdot ds\right) \qquad \text{(Equ. 2.24)}$$

$$G_{23} = G_{12}^{core}\left(\frac{4\cdot t_2}{H\cdot L}\int_0^s \sin^2\theta\cdot ds\right) \qquad \text{(Equ. 2.25)}$$

$$\int_0^s \cos^2\theta\cdot ds = \int_0^{S/2} \cos^2\theta_1\cdot ds + \int_{S/2}^s \cos^2\theta_2\cdot ds = \frac{S}{2}\cdot\left(\cos^2\theta_1 + \cos^2\theta_2\right)$$

$$\int_0^s \sin^2\theta\cdot ds = \int_0^s \sin^2\theta_1\cdot ds + \int_0^s \sin^2\theta_2\cdot ds = \frac{S}{2}\cdot\left(\sin^2\theta_1 + \sin^2\theta_2\right)$$

where,

$$\theta = \tan^{-1}\left(\frac{(H)}{(L/2)}\right),\quad \theta = \tan^{-1}\left(\frac{(-H)}{(L/2)}\right)\ ,\quad \frac{S}{2} = \sqrt{\left((L/2)^2 + (H)^2\right)}$$

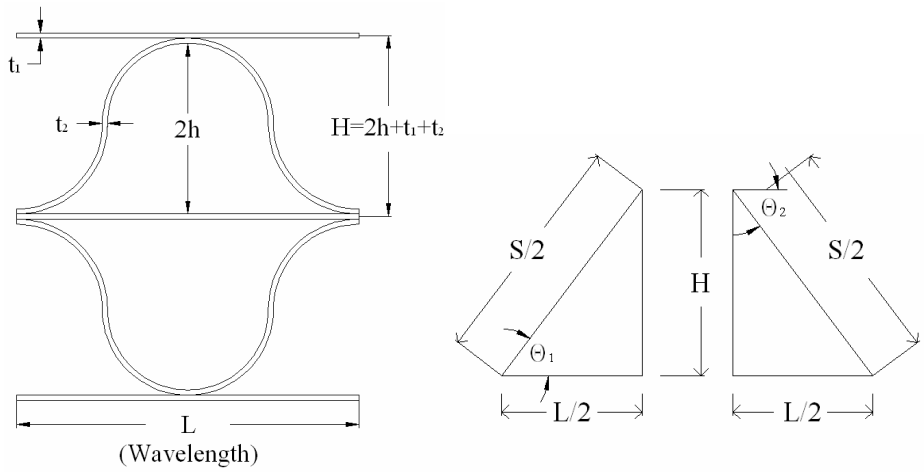

(A) **(B)**

Figure 2.6 -Honeycomb Core Geometry
(A) Actual Geometry and (B) Simplified Model

$$\therefore \quad G_{13} = G_{12}^{core}\left(\frac{2\cdot t_1}{H} + \frac{4\cdot t_2}{H\cdot L}\cdot\frac{S}{2}\cdot\left(\cos^2\theta_1 + \cos^2\theta_2\right)\right) \qquad \text{(Equ. 2.26)}$$

$$\therefore \quad G_{23} = G_{12}^{core}\left(\frac{4\cdot t_2}{H\cdot L}\cdot\frac{S}{2}\cdot\left(\sin^2\theta_1 + \sin^2\theta_2\right)\right) \qquad \text{(Equ. 2.27)}$$

Therefore both out-of-plane shear moduli are a function of the core geometry as well as the in-plane lamina shear modulus of the core material, in this case a CSM material.

Now that equivalent elastic out-of-plane shear properties have been determined it is necessary to create an equation relating out-of-plane shear strains with shear forces,

$$\begin{bmatrix} Q_4^s \\ Q_5^s \end{bmatrix} = \begin{bmatrix} A_{44}^s & A_{45}^s \\ A_{45}^s & A_{55}^s \end{bmatrix}\cdot\begin{bmatrix} \gamma_4^s \\ \gamma_5^s \end{bmatrix}, \quad \begin{bmatrix} \gamma_4^s \\ \gamma_5^s \end{bmatrix} = \begin{bmatrix} a_{44}^s & a_{45}^s \\ a_{45}^s & a_{55}^s \end{bmatrix}\cdot\begin{bmatrix} Q_4^s \\ Q_5^s \end{bmatrix} \qquad \text{(Equ. 2.28)}$$

where,

$$A_{ij}^s = \sum_{k=1}^{n} C_{ij}^{(k)}\cdot\left(x_3^{(k)} - x_3^{(k-1)}\right) = \sum_{k=1}^{n} C_{ij}^{(k)}\cdot h^{(k)} \quad i,j = 4,5 \qquad \text{(Equ. 2.29)}$$

and where Q^s is the transverse shear resultant, γ^s is the transverse shear strain, A^s is the transverse shear stiffness matrix, a^s is the transverse shear elasticity matrix and C_{44}, C_{45}, and C_{55} are the transverse shear stiffness coefficients. Like the lamina stiffness coefficients the transverse shear coefficients are calculated for the core layer,

$$C'_{44} = E_{44} = G_{23}; \quad C'_{55} = E_{55} = G_{13} \qquad \text{(Equ. 2.30)}$$

Then the core is reoriented to the global coordinate system using,

$$\begin{aligned} C_{44} &= C'_{44}\cdot\cos(\theta)^2 + C'_{55}\cdot\sin(\theta)^2 \\ C_{45} &= \left(C'_{55} - C'_{44}\right)\cdot\sin(\theta)\cdot\cos(\theta) \\ C_{55} &= C'_{44}\cdot\sin(\theta)^2 + C'_{55}\cdot\cos(\theta)^2 \end{aligned} \qquad \text{(Equ. 2.31)}$$

Table 2.6 - Equivalent Out-of-Plane Shear Properties

Shear Moduli	Transverse Shear Stiffness
[x10^6 psi]	[x10^6 psi]
G_{13} = 0.037	A_{44} = 0.288
G_{23} = 0.048	A_{55} = 0.222
	A_{45} = 0.000

An example for calculating the out-of-plane shear moduli and transverse shear stiffness matrix is located in Appendix 2.4.1, and the results can be found in Table 2.6.

2.7.2. Modeling Face Sheets

Based on the previous assumptions the in-plane forces in a sandwich panel are resisted by the face sheet laminates alone. The modeling of the face sheets can be approached a few ways. The first and perhaps most direct approach would involve simply skipping section 2.6 and instead calculate the sandwich [ABD] matrix in a manner similar to that used for the laminate. This works best with equally thick symmetric top and bottom face sheets because the neutral axis is located at the center of the beam, but for face sheets with a varying thickness or asymmetric lay-up it can be difficult to determine the neutral axis (Figure 2.7). An example for an E-glass/polyester sandwich panel can be found in Appendix 2.4.2.

Another approach would involve following section 2.6 and then create a set of equivalent material properties for each face sheet laminate. These material properties can then be used to calculate the sandwich [ABD] matrix for the three layer laminate (Top face sheet – Core – Bottom face sheet) in a manor similar to section 2.6. A set of equivalent laminate properties can only be developed for the laminate if the lay-up

sequence is symmetric or nearly symmetric. Meaning if the coupling stiffness matrix B is very small then the laminate is basically acting uncoupled, leaving two sets of equivalent material properties. The equivalent axial properties for the laminate are shown below,

$$E_1^N = \frac{A_{11} \cdot A_{22} - A_{12}^2}{h \cdot A_{22}}, \quad \text{(Equ. 2.32)}$$

$$E_2^N = \frac{A_{11} \cdot A_{22} - A_{12}^2}{h \cdot A_{11}}, \quad \text{(Equ. 2.33)}$$

$$E_6^N = G_{12}^N = \frac{A_{66}}{h}, \quad \text{(Equ. 2.34)}$$

$$\nu_{12}^N = \frac{A_{12}}{A_{22}}, \quad \text{(Equ. 2.35)}$$

$$\nu_{21}^N = \frac{A_{12}}{A_{11}} \quad \text{(Equ. 2.36)}$$

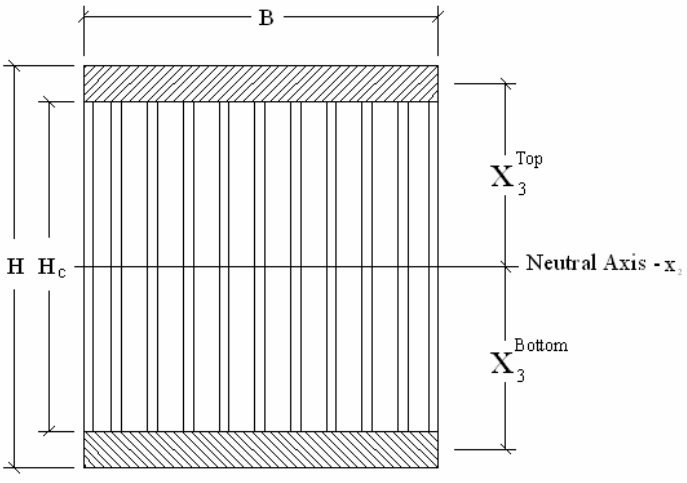

Figure 2.7 - Cross-Section of the Sandwich Panel

And the equivalent flexural properties are,

$$E_1^M = \frac{12 \cdot \left(D_{11} \cdot D_{22} - D_{12}{}^2 \right)}{D_{22} \cdot h^3}, \quad \text{(Equ. 2.37)}$$

$$E_2^M = \frac{12 \cdot \left(D_{11} \cdot D_{22} - D_{12}{}^2 \right)}{D_{11} \cdot h^3}, \quad \text{(Equ. 2.38)}$$

$$E_6^M = G_{12}^M = \frac{12 \cdot D_{66}}{h^3}, \quad \text{(Equ. 2.39)}$$

$$\nu_{12}^M = \frac{D_{12}}{D_{22}}, \quad \text{(Equ. 2.40)}$$

$$\nu_{21}^M = \frac{D_{12}}{D_{11}} \quad \text{(Equ. 2.41)}$$

The benefits of this approach include being able to use it when the face sheets are of unequal thickness. Although like the first approach the neutral axis will have to be found, but it is now a much simpler procedure involving a few simple sumations,

$$\bar{y}^k = \frac{\sum_{k=1}^{3} E_1^k \cdot t^k \cdot \bar{y}^k}{\sum_{k=1}^{3} E_1^k \cdot t^k} \quad \text{(Equ. 2.42)}$$

where E_1 is the equivalent axial modulus, t is the thickness of the layer, and $\bar{y}$ is the distance to an arbitrary datum. An example of this approach for a E-glass/polyester sandwich panel can be found in Appendix 2.4.3

The third approach involves using the [ABD] matrixes calculated for each face sheet in section 2.6 and then move the location of the axis of bending from the center of the laminate to the neutral axis of the sandwich panel. This can be accomplished using

the parallel axis theorem, which is shown below; a derivation of which can also be seen in Appendix 2.7.

$$A_{ij}^{S} = A_{ij}^{L}, \qquad \text{(Equ. 2.43)}$$

$$B_{ij}^{S} = B_{ij}^{L} + x_O \cdot A_{ij}^{L}, \qquad \text{(Equ. 2.44)}$$

$$D_{ij}^{S} = D_{ij}^{L} + 2 \cdot x_O \cdot B_{ij}^{L} + x_O^2 \cdot A_{ij}^{L} \qquad \text{(Equ. 2.45)}$$

Where A^s, B^s, and D^s are the [ABD] matrixes for the laminate bending about the sandwich neutral axis, A^L, B^L, and D^L are the [ABD] matrixes for the laminate bending about the center of the laminate, and x_o is the offset from the center of the laminate to the sandwich neutral axis. The benefit of this procedure is that it can be used with asymmetric face sheets of uneven thickness, and the sandwich neutral axis is,

$$\bar{y}^{k} = \frac{\sum_{k=1}^{2}\left(\frac{A_{11}^{k} \cdot A_{22}^{k} + A_{12}^{k\,2}}{A_{22}^{k}}\right) \cdot \bar{y}^{k}}{\sum_{k=1}^{2}\left(\frac{A_{11}^{k} \cdot A_{22}^{k} + A_{12}^{k\,2}}{A_{22}^{k}}\right)} \qquad \text{(Equ. 2.46)}$$

An example of this method for a E-glass/polyester sandwich panel is located in Appendix 2.4.4 and the results can be found in Table 2.7.

2.8. Sandwich Panel Reactions

Since the behavior of the entire sandwich panel has been determined it is necessary to evaluate the overall beam kinematics and equilibrium conditions in order to obtain the sandwich panel reactions under various conditions. Two main approaches available are classic beam theory (Euler-Bernoulli beam theory) and shear deformation beam theory (Timoshenko beam theory). The main difference between the theories arises

Table 2.7 - ABD Matrix for Sandwich Panel

Axial Stiffness [x10^6 psi]	Coupling Stiffness [x10^6 psi]	Flexural Stiffness [x10^6 psi]
A_{11} = 3.591	B_{11} = 0.000	D_{11} = 38.013
A_{12} = 0.225	B_{12} = 0.000	D_{12} = 2.381
A_{16} = 0.000	B_{16} = 0.000	D_{16} = 0.000
A_{22} = 1.225	B_{22} = 0.000	D_{22} = 12.974
A_{26} = 0.000	B_{26} = 0.000	D_{26} = 0.000
A_{66} = 0.377	B_{66} = 0.000	D_{66} = 3.989

from the Euler-Bernoulli assumption that plane cross-section will remain perpendicular to the neutral axis, $\psi = \frac{dw}{dx_1}$, under bending as seen in Figure 2.8. This means that the beam deflection is entirely due to flexure and shear deformation causes no deflection. The shear deformation theory on the other hand does not assume perpendicular cross-sections during bending and therefore allows deflection due to flexure as well as shear deformation. The Euler-Bernoulli theory is generally used for long slender beams, while the Timoshenko shear deformation theory is generally used for short, thick beams. The basic kinematics model for a beam subjected a flexural load with bending about the x_2 axis is shown in Figure 2.8. The general equilibrium equations for both theories are found Appendix 2.7, and can be modified to account for the sandwich panel stiffness. The equilibrium equations for a composite beam subjected to a flexural load with bending about the x_2 axis are:

Timoshenko Beam Theory

$$M^{T}_{(x_1)} = b \cdot \left(B_{11} \cdot \varepsilon_{a1} + D_{11} \cdot \frac{d\psi^{T}}{dx_1} \right)$$

$$Q^{T}_{(x_1)} = \frac{d}{dx_1}\left[b \cdot \left(B_{11} \cdot \varepsilon_{a1} + D_{11} \cdot \frac{d\psi^{T}}{dx_1} \right) \right]$$

$$q^{T}_{(x_1)} = \frac{d^2}{dx_1^{\,2}}\left[b \cdot \left(B_{11} \cdot \varepsilon_{a1} + D_{11} \cdot \frac{d\psi_1}{dx_1} \right) \right]$$

$$\frac{dw}{dx_1} - \psi^{T}_{(x_1)} = \frac{-Q^{T}_{(x_1)}}{k^s \cdot b \cdot A^s_{55}}$$

$$\kappa_1 = \frac{d\psi_1}{dx_1}$$

Euler-Bernoulli Theory

$$M^{E}_{(x_1)} = b \cdot \left(B_{11} \cdot \varepsilon_{a1} + D_{11} \cdot \frac{d^2 w}{dx_1^{\,2}} \right)$$

$$Q^{E}_{(x_1)} = \frac{d}{dx_1}\left[b \cdot \left(B_{11} \cdot \varepsilon_{a1} + D_{11} \cdot \frac{d^2 w}{dx_1^{\,2}} \right) \right]$$

$$q^{E}_{(x_1)} = \frac{d^2}{dx_1^{\,2}}\left[b \cdot \left(B_{11} \cdot \varepsilon_{a1} + D_{11} \cdot \frac{d^2 w}{dx_1^{\,2}} \right) \right]$$

$$\frac{dw}{dx_1} - \psi^{E}_{(x_1)} = \frac{-Q^{E}_{(x_1)}}{k^s \cdot b \cdot A^s_{55}} = \varepsilon_5 \approx 0$$

$$\psi^{E}_{(x_1)} = \frac{dw}{dx_1}$$

where M is the moment, Q is the shear, q is the distributed load, *w* is the vertical deflection, ψ_1 is the rotation about the x_2 axis, κ_1 is the curvature of bending, b is the beam width, B is the coupling stiffness matrix, D is the flexural stiffness matrix, A^s is the transverse shear stiffness matrix and k^s is the shear correction factor. The shear

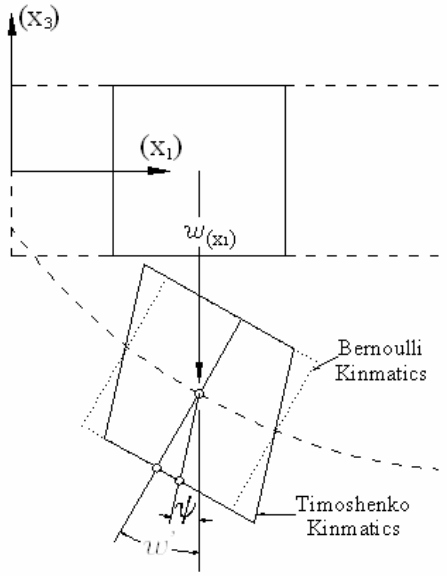

Figure 2.8 - Euler-Bernoulli and Timoshenko Beam Kinematics

correction factor k^s is needed because the Timoshenko beam theory inaccurately assumes the shear strain is uniform through the depth of the cross-section. The k^s factor for a general laminate depends on the lamina properties as well as the lay-up sequence, and is typically difficult to calculate. Birman recommends using k^s=1 as a first approximation for the analysis of both two-skinned and multi-skinned sandwich structures unless other methods yielding different values are available (Birman, 2002).

From this point on we will limit our attention to the special case of a symmetric simply supported beam subjected to 3-point bending about the x_2 axis. For this case the moment creates longitudinal curvature $\kappa_1 = d_{11} \cdot M_1$, as well as transverse curvature, $\kappa_2 = d_{12} \cdot M_1$. The transverse curvature can be visualized as bending of the cross-section, where the center sags when compared to the right-most and left-most sides of the beam. The d_{12} term is many orders of magnitude smaller than the d_{11} term; therefore it can be ignored. So for the current 3-point bending case the flexural stiffness is dependant only on the flexural stiffness coefficient D_{11}. At this point it is advantageous to combine the beam width and the coefficient D_{11}, which results in $\overline{D}_{11} = b \cdot D_{11}$. When using Timoshenko theory $\overline{A}^s_{55}$ should also be found in a similar manor. A useful derivation that relates Euler-Bernoulli bending to Timoshenko bending (Wang, 1995) for beams with a coupling stiffness [B] matrix equal to zero can be found in Appendix 2.8. The derivation for the deflection, shear and moment equations for a symmetric simply supported beam subjected to 3-point bending can be found in Appendix 2.9. The equations for maximum deflection and moment at the center of the beam are shown below,

Euler-Bernoulli Theory *Timoshenko Beam Theory*

$$w^E = \frac{P \cdot L^3}{48 \cdot \overline{D}_{11}} \quad \text{(Equ. 2.47)} \qquad w^T = \frac{P \cdot L^3}{48 \cdot \overline{D}_{11}} + \frac{P \cdot L}{4 \cdot k^s \cdot \overline{A}^s_{55}} \quad \text{(Equ. 2.48)}$$

$$M_1^E = \frac{P \cdot L}{4} \quad \text{(Equ. 2.49)} \qquad M_1^T = \frac{P \cdot L}{4} \quad \text{(Equ. 2.50)}$$

Using these equations a comparison was performed between both beam theories and a sample calculation can be found in Appendix 2.4.3. The comparison as well as results obtained from a detailed finite element analysis of the beam that was conducted separately can be found in Figure 2.9. The Euler-Bernoulli theory shows nearly 19% less deflection than the FE analysis, while the shear deformation theory neglecting the shear capacity of the face sheet laminates obtains nearly 17% more deflection than the FE analysis. When the shear capacity of the face sheet laminates is considered in the shear deformation theory the deflections are just 7% less than those obtained in the FE analysis. The load-verses-strain data results for the Euler-Bernoulli classic beam theory are compared to the FE analysis results in Figure 2.10. The classic beam theory only shows about 3% more strain in the extreme fiber at the mid-span. Even though the classic beam theory has significantly less deflection than a more detailed analysis, it seems to provide adequate strain data.

2.9. Internal Stresses and Strains

Although the overall beam behavior and reactions are essential parts of a good design, it is also useful and in most cases necessary to identify the internal stresses and

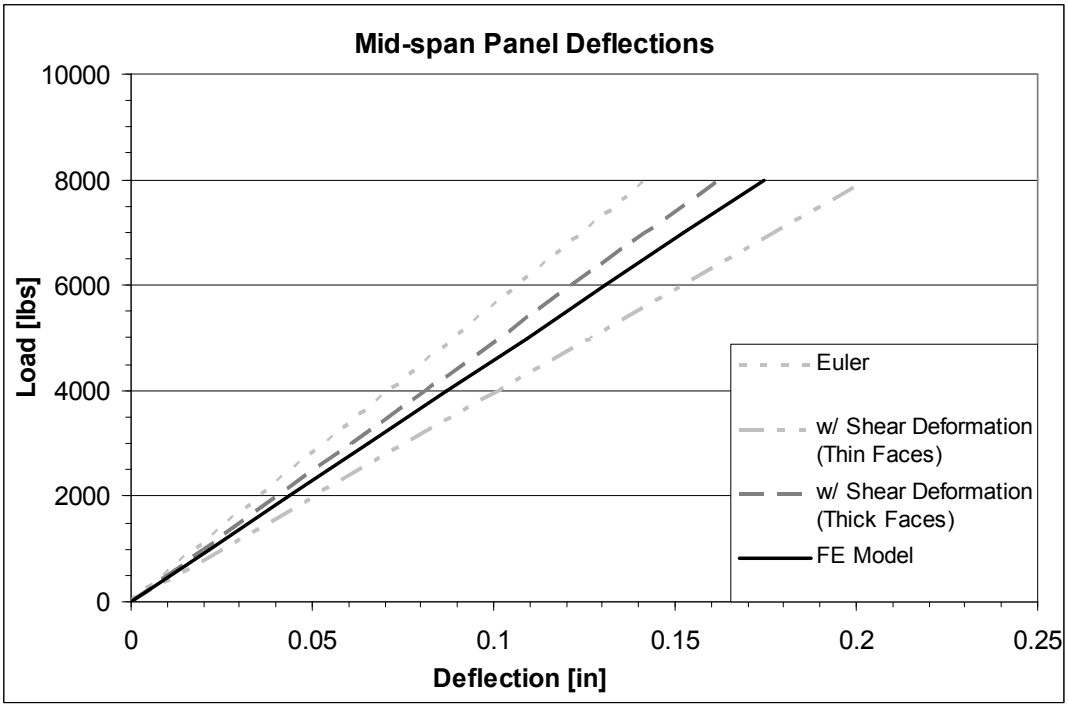

Figure 2.9 – Load-Deflection of Sandwich Panel

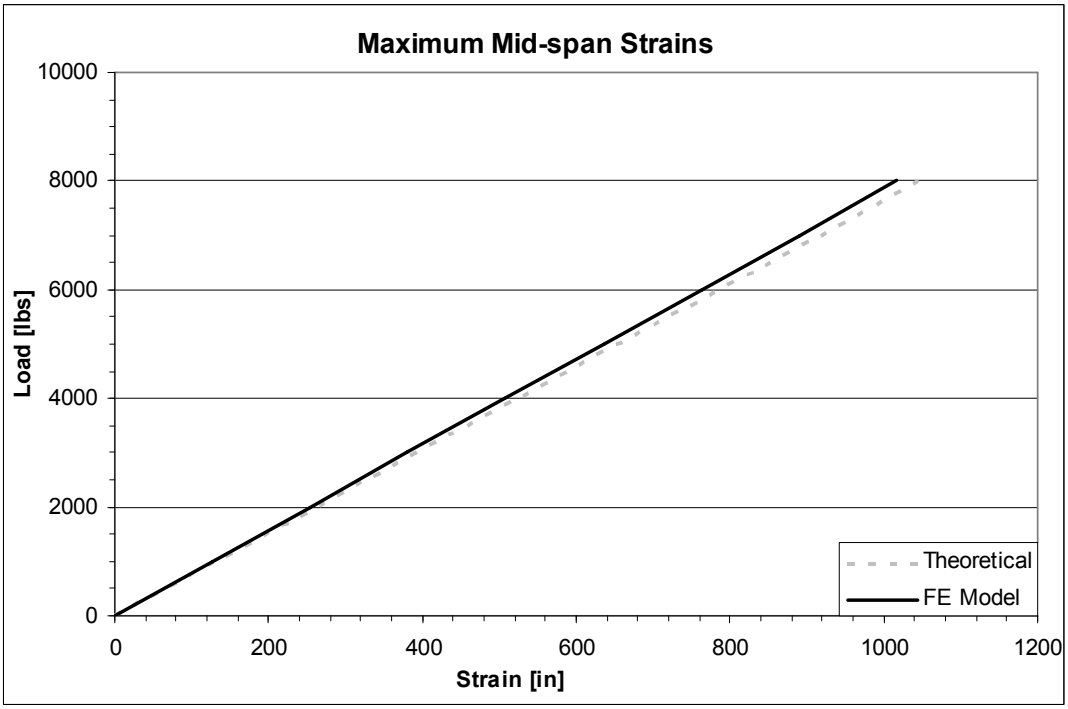

Figure 2.10 – Load-Strain for Sandwich Panel

strains throughout the sandwich cross-section as well as within each lamina. Although this has not been covered explicitly so far most of the tools needed for such an analysis have already been discussed. Due to the complex nature of periodic core geometries the stress-strain analysis will be limited to the flexural stress and strains within the face sheets.

Once the beam behavior as well as the reactions at the section of interest has been obtained it is a fairly simple matter to determine the strain profile through the cross-section. Although the [ABD] matrix can be used to calculate the axial forces and flexural moments due to given axial strains and flexural curvatures, it is not adequate to determine the strains and curvatures under known forces. It is therefore necessary to calculate the [abd] elasticity matrix, which as stated in section 2.6, does give strains and curvatures for given loads. The [abd] matrix can be obtained by simply inverting the [ABD] matrix, or for the special case where the [B] matrix is zero the [A] and [D] matrixes are uncoupled and can be inverted separately. Once the [abd] matrix has been calculated it can be used to calculate the axial strains (ε_a) and flexural curvatures (κ). Multiplying the curvature by x_3 obtains the flexural strains. An assumption that was made during the analysis of the sandwich panel behavior was that the strain profile was linear over the cross-section; this does not however mean that the stress profile is linear. In fact the stress profile is typically not linear because it jumps as the stiffness of each lamina changes throughout the thickness of the cross-section, this can be seen in Figure 2.11. Therefore it is necessary to calculate the strain in the top and bottom of each lamina so that the stresses at the lamina interfaces can be calculated. Once the strain has been calculated the lamina

stresses can be found using the standard lamina stiffness matrix (Equ. 2.11) for the specific type of lamina in question.

The stresses and strains calculated so far are oriented using the global coordinate system, but typically the local stresses and strains within each lamina are important. In other words it is important to know the stress and strain in the fiber direction or in the direction transverse to the fibers. Therefore use the transformations found in (Equ. 2.15) and (Equ. 2.17) to transform the global stresses and strains to local stresses and strains. An example of the procedures used to obtain the stress and strain profiles along the sandwich beam can be seen in Appendix 2.6.

2.10. Simplified Procedures

Typically the analytical procedures detailed in the previous sections are unnecessarily long and tend to calculate more information than is needed. Most

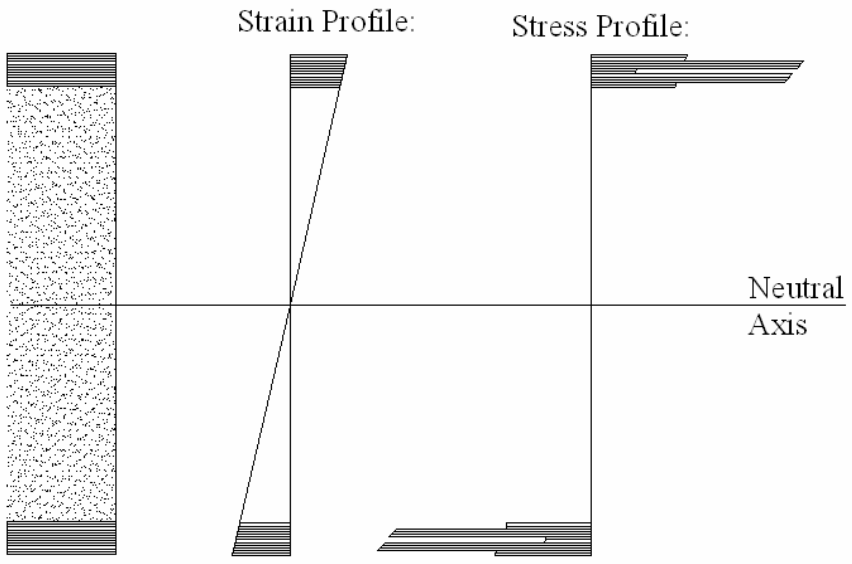

Figure 2.11 – Strain and Stress Profiles of a Typical Sandwich Panel

situations simplified procedures would be adequate and actually obtain data that is very comparable to the more complicated analysis. A brief simplified procedure for a symmetric sandwich panel with equally thick face sheet laminates is detailed here. This simplified method is based on the theoretical analysis of a three-part sandwich panel. The flexural stiffness $\overline{D}$ term calculated in section 2.8 can be obtained by observing that it is essentially the modulus of elasticity lumped together with the moment of inertia of the section. The assumption that the core modulus is much smaller than the modulus of the face sheets, and the flexural stiffness of the face sheets are much less than the stiffness due to offsetting them from the center of the beam. Therefore for the three-part sandwich panel the flexural stiffness $\overline{D}$ term can be calculated using the following,

$$\overline{D} = 2 \cdot E^f \cdot \frac{b \cdot \left(h^f\right)^3}{12} + 2 \cdot E^f \cdot b \cdot h^f \cdot \left(\frac{h^c + h^f}{2}\right)^2 + E^c \cdot \left(\frac{b \cdot \left(h^c\right)^3}{12}\right)$$

$$\overline{D} = 2\overline{D}_{face} + \overline{D}_{offset} + \overline{D}_{core} \approx \overline{D}_{offset}$$

$$\therefore \overline{D} \approx 2 \cdot E^f \cdot b \cdot h^f \cdot \left(\frac{h^c + h^f}{2}\right)^2 \qquad \text{(Equ. 2.51)}$$

where, E^f is the modulus of the face sheets, E^c is the modulus of the core, b is the beam width, h^f is the thickness of the face sheets, h^c is the thickness of the core, $\overline{D}_{face}$ is the flexural stiffness of the face sheets, $\overline{D}_{core}$ is the flexural stiffness of the core, and $\overline{D}_{offset}$ is the flexural stiffness due to the face sheet offsets. Now all that is needed is a few geometric properties and the effective modulus of elasticity of the face sheets.

The procedure to find the effective modulus of elasticity of the face sheets is the same as the methods presented above, but in section 2.6. Once the [A] matrix has been calculated use the following equation to calculate the effective modulus of elasticity of the face sheets due to an axial load,

$$E_1^N = \frac{A_{11} \cdot A_{22} - A_{12}^{\,2}}{h \cdot A_{22}} \qquad \text{(Equ. 2.52)}$$

Once the flexural stiffness $\overline{D}$ term has been calculated use the proper bending equations to obtain the moments and deflections. Now instead of calculating the [abd] matrix to obtain the curvatures due to a particular moment it is possible to use a simpler curvature equation,

$$\kappa_1^M = \frac{M}{\overline{D}} \qquad \text{(Equ. 2.53)}$$

And now the flexural strain and flexural stress profile can easily be calculated using the following two equations,

$$\varepsilon_1^{flex} = \frac{M}{\overline{D}} \cdot x_3 \qquad \text{(Equ. 2.54)}$$

$$\sigma_1^{flex} = M \cdot \frac{Q_{11}^{(\text{Lamina})}}{\overline{D}} \cdot x_3 \qquad \text{(Equ. 2.55)}$$

CHAPTER 3

EXPERIMENTAL TESTING PROCEDURES

3.1. Motivation for Research

Highway bridges have traditionally been constructed using structural steel or reinforced concrete, but these bridges have been plagued by costly maintenance and rehabilitation costs due to material degradation and corrosion caused by exposure to harsh natural environments as well as other man-made products such as deicers. This trend has lead to an increased amount of highway bridge repairs at a time when the reliance on the interstate system continues to grow. The need for structurally sound, low-maintenance materials as well as procedures and systems promoting rapidly constructible structures has lead to a renewed interest in high performance as well as nontraditional materials. Fiber-reinforced polymer (FRP) composites are one such nontraditional material that has received a large amount of interest in the last few years.

In order to obtain a sound structural design an engineer must have a though understanding of a materials behavior when subjected to various environments as well as extreme events. There are however numerous gaps in our understanding of the behavior of FRP materials under various natural environments. Because it is generally understood that FRP materials become stiffer at lower temperatures due to their polymer nature, the other, at times detrimental behavioral effects of low temperature environments are sometimes overlooked. Although research has been conducted and strides have been made in understanding the low-temperature behavior of FRP materials, a lack of comparable testing procedures and reproducible results has lead to confusion and a lack

of confidence in applying them. Therefore the overall motivation for the experimental regiment discussed within this thesis was to delve deeper into the material properties and behavior of FRP composites at low temperatures. In particular special attention was placed on expounding upon the results and conclusions of an experimental test previously conducted on a FRP bridge deck panel.

3.2. Previously Conducted Research

Usha Choppali previously conducted an experimental study observing the effects of low-temperature and low-temperature thermal cycling on the performance of an FRP composite bridge deck panel while at the University of Alaska Fairbanks. Kansas Structural Composites, Inc provided an e-glass/polyester honeycomb sandwich bridge deck panel, which had an overall geometry of 7' length, 13.4" width, and 7" thickness. The sandwich panel was fabricated by sandwiching a 6-inch sinusoidal core between two 0.5-inch face sheets. The face sheet laminates were comprised of ten unidirectional longitudinal layers or lamina sandwiched between two layers of biaxial stitched fabric. A more detailed description of the entire sandwich panel can be found in chapter 2. A total of 22 strain gages and 12 thermocouples were installed on the test specimen prior to testing. The panel specimen was tested under three-point bending at room temperature by loading the panel in 500 lb increments up to a service load of 8,000 lbs before unloading it. The test was repeated at 32 °F [0 °C], -4 °F [-20 °C], and 24 °F [-31 °C], after which the panel specimen was tested once again at room temperature. A final failure test was conducted on the specimen at a temperature of -55 °C (Ma, Choppali

2007). The results of the experimental tests on the FRP bridge deck sandwich panel are summarized as follows:

- Temperature plays an important role in the stiffness of the panel.
- Stiffness at lower temperatures is typically higher that at high temperatures, but a reversal in this trend was noted at temperatures below -4 ºF [-20 ºC].
- The loss in stiffness seemed to be permanent and was not regained when the panel was raised back to room temperature.
- The panel failure was due to the face sheets debonding from the core.

3.3. Testing Goals

The preliminary testing goals for the experimental tests outlined in this thesis were obtained after analyzing the results from Choppali's FRP bridge deck panel tests. Due to the fact that the face sheets within the sandwich panel provide most of the structural stiffness, it was decided a closer look at the properties of the face sheets would be a beneficial progression in understanding the low-temperature response of the FRP bridge deck panel. It was felt that a separate analysis of the uniaxial and biaxial layers could help simplify the interpretation of the final testing results. Also in order to standardize the testing results the longitudinal modulus of elasticity would be observed instead of the sample stiffness, thereby negating variances in the cross-sectional area. Therefore, the preliminary test goals included obtaining the overall behavior of the individual uniaxial and biaxial layers so that a more detailed numerical and FE model could be developed in the future and to determine if the stiffness transition seen in the

panel test at temperatures below -4 °F[-20 ºC] could be linked to the individual material properties or if it was a structural or bonding phenomenon.

A series of initial tests were conducted and showed an increase in the longitudinal modulus of elasticity as the temperature was decreased down to -31 ºF [-35 ºC] when subjected to 1000 micro-strain, strain levels equivalent those observed in the previous panel tests due to a service loading. Therefore the loss of stiffness seen in the panel test at temperatures below -4 ºF [-20 ºC] could not be attributed to the face sheet behavior. However when the test samples were subjected to two or three times the strain observed in the panel test a significant non-recoverable degradation in the modulus was observed and at times this degradation seemed to counteract any increase associated with a reduction in the temperature of the specimen. The final testing goals were therefore expanded to include an experimental analysis of how low-temperature coupled with various strain levels affect the longitudinal modulus of elasticity.

3.4. Description of Test Samples

Kansas Structural Composites Inc provided E-glass/polyester fiber reinforced polymer (GFRP) sheets with various fiber arrangements that were fabricated using a hand lay-up method. The constituent materials, fabrication method and mixing procedures were all similar to those used to fabricate the GFRP bridge deck panel previously mentioned. The sheets were smooth on the front side but had small groves and imperfections on the reverse side. This variation occurred because the E-glass fiber mats used in the fabrication of the sheets had a thin layer of random E-glass strands for mat stability. These random strands were laid down first and then impregnated with resin

thereby creating a smooth face, but the other face did not have the thin layer or the mold surface and therefore had the grooves and imperfections mentioned. It was also noted that the thickness varied roughly 10-15% at points. It was felt that more precise samples could be fabricated but would be of a different quality than those used in the actual deck panel, therefore the GFRP sheets supplied by KSCI were used in the fabrication of the test samples. The biaxial sheets had an overall geometry of 15" length, 15" width, and a thickness of roughly 0.15" while the uniaxial sheets had an overall geometry of 10" length, 10" width and a thickness of roughly 0.12". All the samples were comprised of Altek H834-R series polyester resin (Alpha/Owens-Corning) with E-glass reinforcement. Uniaxial sheets were fabricated using three longitudinal layers of UM-1810 unidirectional combo mat E-glass, while biaxial sheets were fabricated with two layers of CM-3205 non-woven bi-ply combo mat E-glass.

The test coupon geometry was chosen after consulting previously conducted research as well as ASTM D3039, "Standard Test Method for Tensile Properties of Polymer Matrix Composite Materials". While ASTM D3039 does not give exact sample requirements, it does provide some general requirements as well as some geometry recommendations. The requirements included a minimum length of gripping, a width tolerance of ± 1% and a thickness tolerance of ± 4%. It should be noted that the thickness tolerance of ± 4% was not achieved due to the varying nature of the materials supplied. ASTM D3039 recommended the sample geometry to be 10" length, .5" width, 0.04" thickness with 2.25" tabs. The recommendation for a balanced biaxial sample was 10" length, 1" width and a 0.1" thickness. Because it was desired that both uniaxial and biaxial samples had the same sample geometry and for ease of fabrication a one-inch

width was chosen. The fabrication equipment available could only facilitate up to a 9-inch sample length therefore a sample length of 9 inches was chosen, but the tab length was reduced to one and a half inches. The final sample geometry was 9" long and 1" wide with 1.5" end tabs; this left a 6" central gage length. The sample dimensions as well as some actual test samples are shown in Figure 3.1.

The individual test samples were initially rough-cut from the GFRP sheets provided by KCSI with a band saw to an overall geometry of 9" length and 1.5" width. After being rough cut the samples were cut to the final 9" x 1" strips using a Manhattan Supply Company 612 surface grinder equipped with a 1-inch flag strip guide. End tabs with a geometry of 1.5" x 1" x 0.06" were bonded to the ends of the samples to help ensure proper stress development within the gauge length. The end tabs were originally

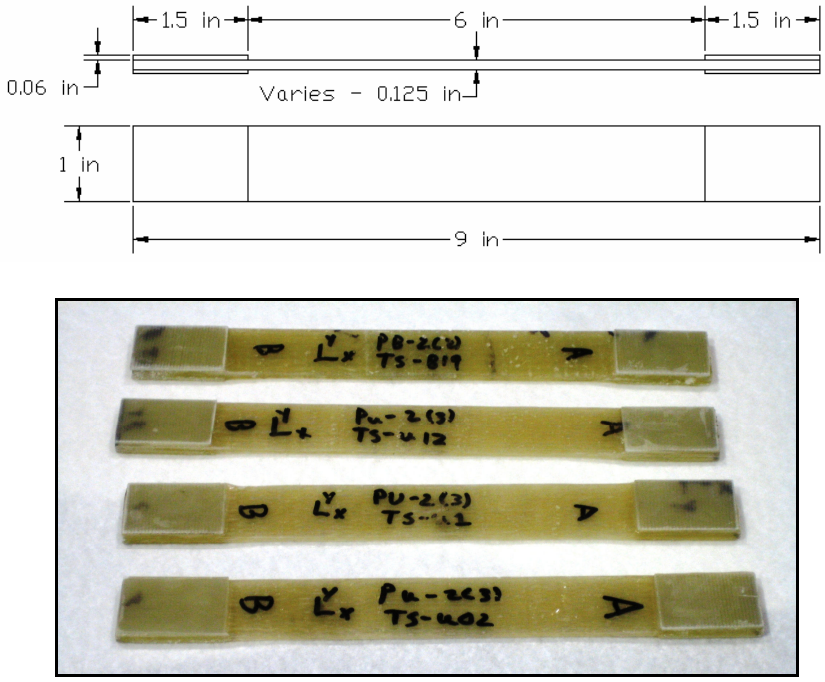

Figure 3.1 - Test Samples
(Top) Sample Geometry and (Bottom) Physical Samples

bonded to the samples using plastic epoxy from Loctite with a 24 hour cure time, but due to tab debonding and degradation on some of the original samples Hysol epoxy from Henkel with a 5 day cure time was used for all later samples. Each sample was labeled on the smooth front face and the top and bottom of the sample were designated A and B respectively.

3.5. Materials and Equipment Used

The testing procedures described in this paper used various equipment and sensors. At this point it is advantageous to briefly describe the equipment so that a more accurate understanding of the testing process can be obtained.

3.5.1. Load Frame

The entire testing regiment was conducted using an MTS 810.25 Material Testing System. The 810.25 system is capable of supplying up to 55 kips of force and was equipped with a MTS 609 alignment fixture, 661.22C01 axial force transducer (55 Kip), 661.20E02 axial force transducer (11 Kips), custom extension rods, 647 hydraulic wedge grips and 685.10 high temperature hydraulic grip supply. Although the load frame was larger than needed for testing the samples, it was the smallest frame capable of mounting the Applied Test System (ATS) environmental chamber. The 647 Grips had an operating temperature range of -40 to 350 °F with the high temperature grip supply. To help improve the force transducer data resolution, a smaller 11 kip load cell was piggybacked to the larger 55 kip cell. The load frame can be seen in Figure 3.2.A.

3.5.2. Force Transducer

As previously mentioned the 661.20E02 axial force transducer (11 Kips) was piggybacked onto the larger transducer so that an improved force resolution could be obtained. Both the 55 kip and 11 kip transducers are shown in Figure 3.2.B. The MTS 661 series high capacity force transducers are designed for both cyclic and monotonic testing applications and have a usable range of -50 °F to 200 °F and a compensated range of 50 °F to 150 °F.

3.5.3. Extensometer

An extensimeter is a device that is used to measure small changes in the length of a specific gauge length. A MTS model 634.31E-25 extensometer was used for the tests.

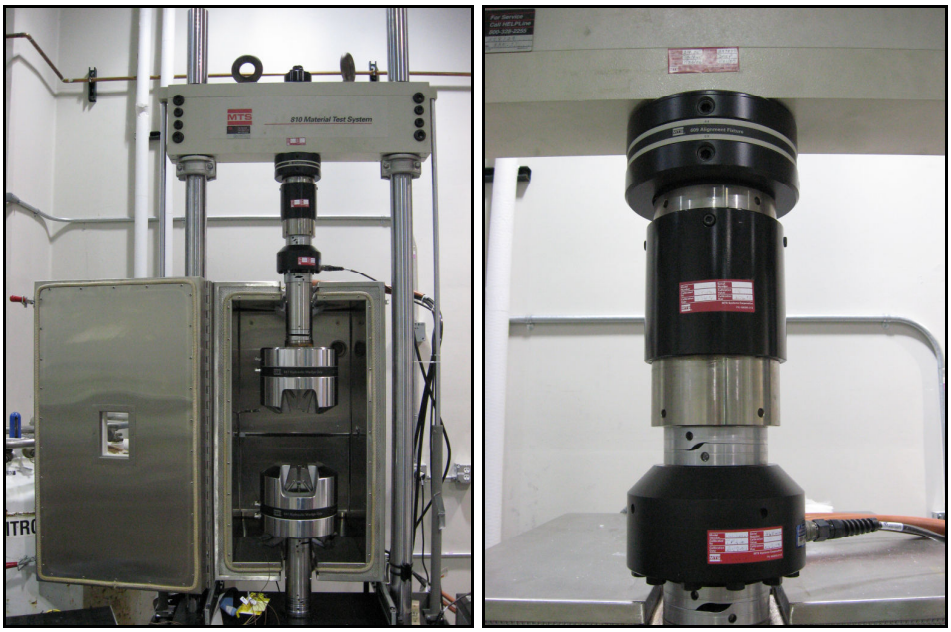

(A) **(B)**

Figure 3.2 - Load frame and Load Cells
(A) Load Frame and (B) 11 kip (lower) and 55 Kip Force Transducer (top)

The 643.31E-25 has a variable gauge length (0.5–2 inches), a travel range of +.200/-.100 inches, and a temperature range of -150 to 350 °F. The extensometer could be attached using either a set of spring arms included with it or by using rubber bands attached to each knife blade. The MTS controller was connected to the extensometer and it could be used to control the actuator under a strain control mode. Data was obtained directly from the MTS system along with force transducer and actuator position data. The extensometer was the primary strain sensor during the tests and was used with a one inch gage length. The extensometer was attached to the center of the 6 inch sample gage length using the spring arms.

3.5.4. Environmental Chamber

Due to the necessity of maintaining a cold controllable environment for the entire span of each samples testing life, it was determined that a small, enclosed environmental cooling chamber was needed. The environmental chamber was manufactured by Applied Test Systems and used liquid nitrogen (LN2) for cooling. The chamber was a series 3710 box oven with a liquid nitrogen injector assembly and cryogenic solenoid. The LN2 was supplied to the system by 160 liter 22 psi liquid nitrogen tanks. Each tank could last roughly 12 to14 hours under system operation. Both the chamber and the LN2 tanks are shown in Figure 3.3. The overall chamber geometry was 23.5” wide, 30” deep, and 41.5” high, and the internal dimensions were 18” wide, 18” deep, and 36” high. The chamber included two load train ports with inserts, a 4” x 6” view port, and an internal light. The chamber is rated for a temperature range of -245 to 570 °F. The camber also came with a

series AB-900 temperature control system that included an Allen-Bradley 900-TC16 digital controller.

3.5.5. MEGADAC Data Acquisition System

A standalone data acquisition system was used to obtain the thermocouple data during testing. The data acquisition system used was a MEGADAC 3145AC, which was manufactured by Optim Electronics Corporation. The MEGADAC system is capable of a sample rate of 25,000 with accommodations for both dynamic analog and digital data signals. To obtain the analog thermocouple data an AD-816TC Thermocouple Input Module with 16 independent channels was used. The 816TC module was attached to a

(A) **(B)**

Figure 3.3 - Cooling Chamber Setup
(A) Environmental Chamber and (B) 160 Liter Liquid Nitrogen Tanks

JP 816TC Type K jack panel with 16 thermocouple jacks. The MEGADAC system was controlled and logged by TCS software being run on a Dell Latitude laptop. The MEGADAC setup is shown in Figure 3.4.

3.5.6. Thermocouples

Thermocouples were used to obtain temperature data, a total of 4 thermocouples were used during the experiments. One of the four thermocouples was used to obtain the temperature of the chamber while the other three were attached to the test sample. One thermocouple was attached roughly one-inch from either tab and the third was installed at the center of the gage length. Cooper-Atkins bare-tip probe (39138-K) Type-K thermocouples were used during testing and can be seen in Figure 3.5. The 39138-K bare-tip probes can measure immersion, air, or surface temperatures and have a response time around 9 sec in air. The thermocouples were wired into the MEGADAC JP 816TC Type K jack panel and all temperature data was recorded through the MEGADAC.

3.5.7. Strain Gauge

Strain gauges were used at times to confirm the extensometer data. Strain gages measure the deformation or strain over the active length of the gauge by measuring the change in electrical resistance. The gauge factor (G.F.) is the quotient of the change in the strain gauge resistance and the product of the unstrained gauge resistance and the strain. This gauge factor is fairly stable at the normal operating temperature, but varies significantly outside the intended range. Also changing temperatures effect the apparent strain seen in the gauge because the strain gage is naturally changing volume with the

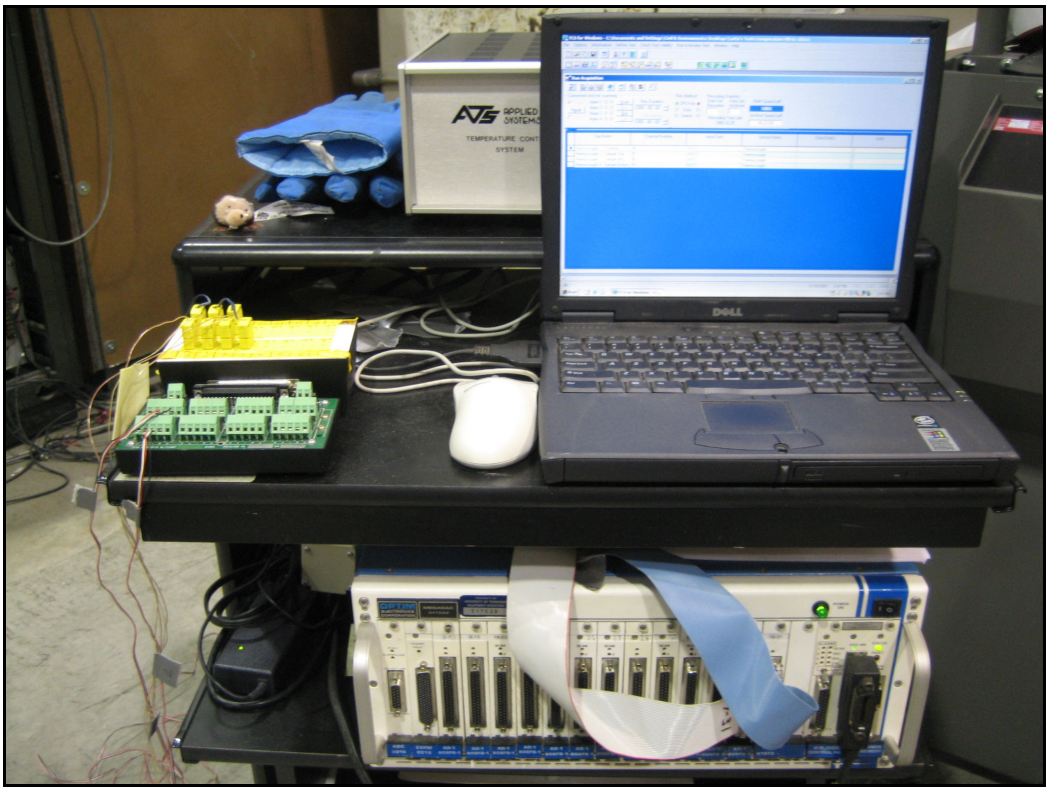

Figure 3.4 - MEGADAC Data Aquisition System

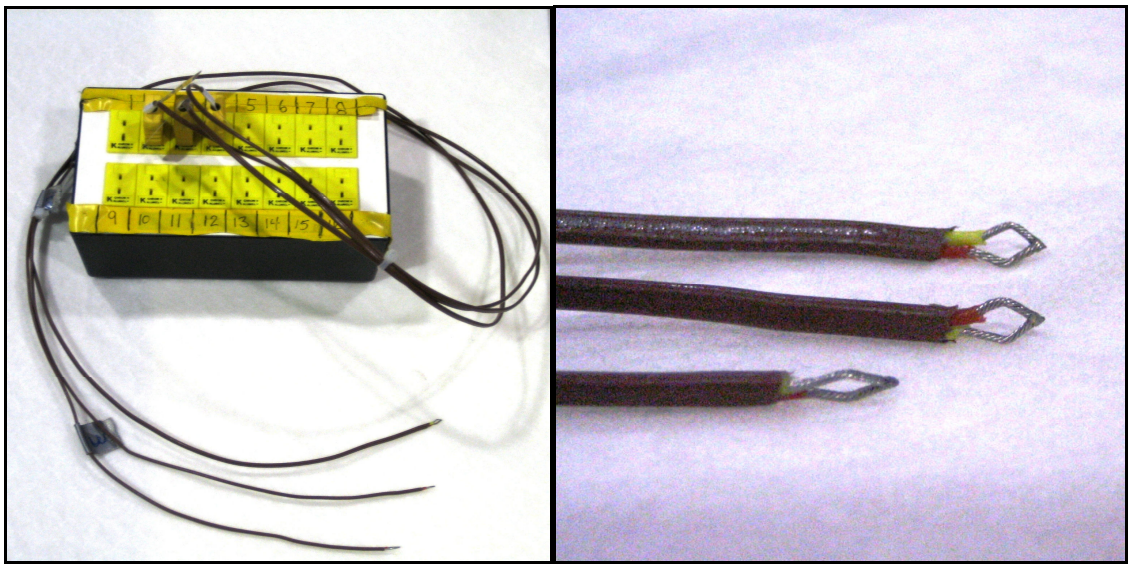

(A) **(B)**

Figure 3.5 - Type-K Thermocouples
(A) Thermocouples with jack panel and (B) Bare Tips of Thermocouples

temperature based on its coefficient of thermal expansion. So if a strain gauge and the sample material have similar coefficients then no thermal expansion strain will be recorded.

Due to the problems associated with strain gages and low temperatures it was decided not to use strain gages as the primary strain measuring method, but only to verify the strain data obtained from the extensometer at various times. All the strain data presented is from the extensometer if not specifically noted. Strain gauges were the only strain sensor used during the final portion of the ultimate strength tests so that the extensometer would not be damaged during sample failure. Overall two types of strain gauges were used in the testing process. The low temperature testes used TML Type: CFLA-6-350-23 gauges because the variation in the G.F. was fairly small for cryogenic temperatures. The ultimate strength tests used Vishay type: L2A-06-125LW-350 gauges because of their availability. A TML gauge mounted on a sample is shown in Figure 3.6.

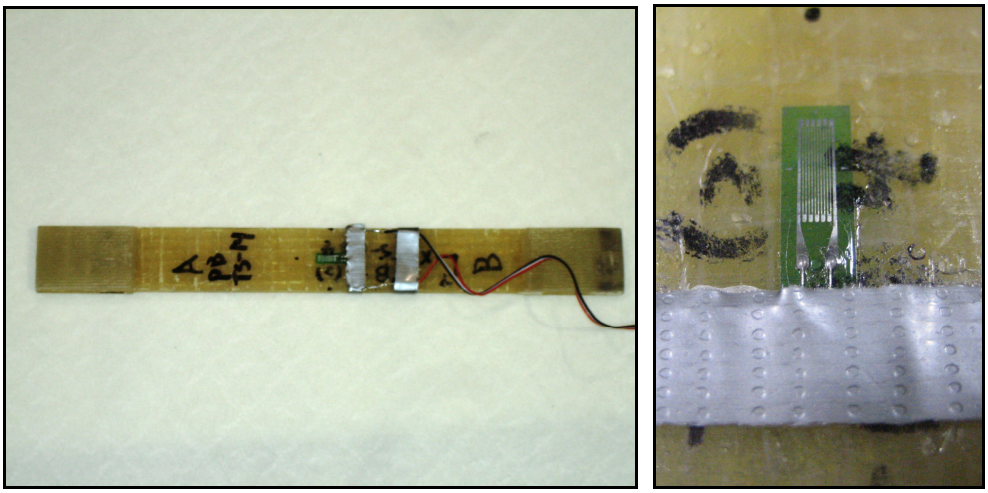

(A) **(B)**

Figure 3.6 - Strain Gauges
(A) Strain Gauge on sample and (B) close-up of Strain Gage (TLM)

3.6. Testing Procedures

The experimental tests outlined in this thesis are broken into three main categories: initial material tests, overall sample behavior and ultimate strength tests, and low-temperature coupled with strain tests. As previously stated the testing goals were to obtaining the overall behavior of the individual uniaxial and biaxial layers as well as observe the low-temperature coupled with various strain levels affected the longitudinal modulus of elasticity. All tests used the sample geometry and fabrication methods previously described.

3.6.1. Initial Material Tests

Due to the flexible nature of the preliminary testing goals a series of initial material tests were conducted to attain a rough understanding of the properties and responses of the various materials that were to be tested. The ultimate strength and basic effects of temperature on the longitudinal modulus of elasticity were roughly determined so that a more detailed testing plan could be created. These tests were also used to work the kinks out of the testing equipment and procedures to be used in later tests. The preliminary test procedures varied with each specific test and therefore a detailed description would be unnecessary and cumbersome. While the testing results for these tests will not be examined in detail they were used to develop latter testing procedures. The initial results for a sample subjected to 1000 micro-strain, service load strains similar to those seen in Ma and Choppali's bridge deck panel test, did not show a reduction in the longitudinal modulus of elasticity near -4 °F [-20 °C] but showed a steady increase in stiffness as the temperature was lowered. Also there was no significant degradation in

the modulus when the samples were returned to room temperature and retested. However strains two or three times the service load levels showed a noticeable reduction in the longitudinal modulus when the samples were returned to room temperature and retested.

3.6.2. Overall Sample Behavior and Ultimate Strength Tests

The overall sample behavior and ultimate strength tests were conducted to provide a better understanding of the stiffness response of the GFRP test samples throughout the entire stress-strain envelope. The ultimate strength tests included both biaxial as well as uniaxial test samples. A 0.25" Vishay strain gauge was attached to the center font side of the sample, and the extensometer using a one-inch gauge length was attached directly over the strain gauge. The strength test procedure was comprised of four main steps. First the sample was loaded at a rate of 25 micro-strain per second up to 3,000 micro-strain after which it was unloaded at the same rate. The previous step was repeated for both 5,000 and 10,000 micro-strain, except the sample was not unloaded after reaching 10,000 micro-strain. The extensometer was removed at this point and the sample was loaded using a displacement control mode at a rate of 0.02 inches per minute until it broke. Strain data was obtained from both the extensometer and the strain gauge up to 10,000 micro-strain but was only obtained for the strain gauge from there up to failure.

3.6.3. Low-Temperature Coupled with Strain Tests

The low-temperature coupled with strain tests can be broken down into two main categories. The first category was concerned with obtaining the longitudinal modulus of

elasticity for both the uniaxial and biaxial e-glass/polyester samples at various low temperatures under strain levels similar to the service load strains observed in Choppali's panel tests, which were just under 1,000 micro-strain. The second category involved elevated strain levels up to 2,000 and 3,000 micro-strain.

Each sample had three thermocouples attached to it. One of the thermocouples was attached in the middle on the reverse side and the other two were attached roughly an inch from each tab on the front side. Also one thermocouple was loose in the chamber and recorded the overall chamber temperature. The extensometer was attached to the center of the front 6" sample gage length, and cryogenic stain gages were installed on a select number of samples.

The overall testing procedure was similar for all the tests and involved subjecting the sample to axial tension to obtain the longitudinal modulus of elasticity at the following temperatures: room temperature, 32 ° F [0 °C], -4 °F [-20 °C], -31 °F [-35 °C]. The sample was held at zero force between tests to reduce the variations in the strain data due to re-gripping the sample and so that the chamber would not have to be opened once the procedure started. The temperature was held for roughly four hours between temperatures to allow the sample and chamber temperature to equalize. After testing the longitudinal modulus of the sample at -32 °F the chamber was allowed to warm up overnight and the modulus was retested at room temperature. Each test involved loading the specimen at a rate of 5 micro-strain/sec up to the target strain and then unloading the specimen at the same rate. This was repeated three times at each temperature so that an average stiffness could be obtained and repeatability of the data could be verified.

CHAPTER 4

EXPERIMENTAL TESTING RESULTS AND DISCUSSION

4.1. Testing Overview and Goals

As mentioned in chapter 3 the preliminary testing goals were to obtain the overall behavior of individual uniaxial and biaxial layers similar to those used in the face sheets of a glass fiber-reinforced polymer (GFRP) bridge deck panel fabricated by Kansas Structural Composites Inc. (KSCI). It was hoped the sample behavior would allow a more detailed numerical and FE model to be developed in the future and also to determine if the stiffness transition seen in the deck panel test around -4°F [-20 °C] (Ma, Choppali 2007) could be linked to the material properties of the face sheet components or if it was a structural or bonding phenomenon. After the initial tests failed to show stiffness transition similar to Ma and Choppali's the testing goals were expanded to include an analysis of how low-temperature coupled with various strain levels affect the longitudinal modulus of elasticity. This chapter presents the analytical procedures used to formulate the testing results, the overall performance and ultimate strength testing results of the GFRP test samples at room temperature, the testing results used to help determine the effect of low-temperatures coupled with various strain levels on the degradation of the longitudinal modulus of elasticity, and an analysis of the entire testing process and results.

4.2. General Testing Nomenclature and Analytical Procedures

For clarity a brief summary of all the test samples can be seen in Table 4.1. The sample nomenclature is simply "P" for polyester and "B" or "U" for biaxial or uiniaxial then "-ts-" which stands for test sample, and finally a number signifying the order of fabrication. It should be noted that as mentioned in chapter 3 the samples had small grooves on the reverse side, and therefore an exact cross-sectional area could not be obtained directly. Calipers were used to measure the thickness of the outer grooves, as well as the average valley depth for the grooves so that a more accurate cross-sectional area could be calculated. The sample cross-sectional area was measured one inch above the center of the gauge length, at the gauge length, and one inch below the gauge length. The average of the three cross-sectional areas was then used as the sample cross-sectional area in all later calculations.

Typically each unique experimental value of the longitudinal modulus of elasticity was verified by three separate loading/unloading or ramping cycles. The average stress data for each cycle was calculated by dividing the force transducer data by the average cross-sectional area of the sample. The average stress data along with the strain data from the extensometer were obtained every second and were later analyzed. Every stress-strain data reading was taken as one data-point, which was then plotted and fitted with a linear regression line. Figure 4.1.B shows the number of data points for each ramping cycle as well as the slope of the regression line, the R^2 fit of the regression line, and the associated 95% confidence intervals. The longitudinal modulus of elasticity for each cycle is equivalent to the value of the slope as long as the behavior remains linear elastic. It should be noted that typically the test samples showed a linear elastic behavior

Table 4.1 - Summary of Test Samples

Sample	Material	Nominal Fiber Volume	Width [in]	Thickness [in]	Test Type
PB-ts-01	Biaxial	0.396	1.007	0.142	Preliminary Test
PB-ts-02	Biaxial	0.396	1.003	0.146	Preliminary Test
PB-ts-03	Biaxial	0.396	1.001	0.149	Preliminary Test
PB-ts-04	Biaxial	0.396	---	---	Sample Damaged
PB-ts-05	Biaxial	0.396	1.002	0.149	Preliminary Test
PB-ts-06	Biaxial	0.396	1.001	0.149	Preliminary Test
PB-ts-07	Biaxial	0.396	---	---	Sample Not Used
PB-ts-08	Biaxial	0.396	---	---	Sample Not Used
PB-ts-09	Biaxial	0.396	---	---	Sample Not Used
PB-ts-10	Biaxial	0.396	0.999	0.139	1000 με Low Temp.
PB-ts-11	Biaxial	0.396	0.993	0.142	1000 με Low Temp.
PB-ts-12	Biaxial	0.396	0.999	0.148	3000 με Low Temp.
PB-ts-13	Biaxial	0.396	1	0.144	3000 με Low Temp.
PB-ts-14	Biaxial	0.396	0.998	0.147	2000 με Low Temp.
PB-ts-15	Biaxial	0.396	0.999	0.151	2000 με Low Temp.
PB-ts-16	Biaxial	0.396	0.999	0.136	3000 με Control Sample
PB-ts-17	Biaxial	0.396	0.999	0.151	2000 με Control Sample
PB-ts-18	Biaxial	0.396	1.002	0.15	3000 με Low Temp.
PB-ts-19	Biaxial	0.396	---	---	Sample Not Used
PB-ts-20	Biaxial	0.396	1	0.154	Ultimate Strength Test
PU-ts-01	Uniaxial	0.33	---	---	Sample Not Used
PU-ts-02	Uniaxial	0.33	1	0.111	Ultimate Strength Test
PU-ts-03	Uniaxial	0.33	1	0.115	Sample Damaged
PU-ts-04	Uniaxial	0.33	1	0.113	1000 με Low Temp.
PU-ts-05	Uniaxial	0.33	1	0.12	1000 με Low Temp.
PU-ts-06	Uniaxial	0.33	0.999	0.116	2000 με Low Temp.
PU-ts-07	Uniaxial	0.33	0.999	0.119	2000 με Low Temp.
PU-ts-08	Uniaxial	0.33	0.994	0.122	2000 με Control Sample
PU-ts-09	Uniaxial	0.33	1	0.122	3000 με Low Temp.
PU-ts-10	Uniaxial	0.33	---	---	Sample Damaged
PU-ts-11	Uniaxial	0.33	1	0.116	3000 με Control Sample
PU-ts-12	Uniaxial	0.33			3000 με Low Temp.

during testing, but periodically a brief period of non-linear elastic behavior was encountered when excessive sample damage occurred. For consistency all stiffness calculations use this linear method unless stated otherwise. The standard error of the slope for each ramping cycle was obtained and used to calculate the 95% confidence interval, which was used to gauge the accuracy associated with each experimental value of the modulus.

After three ramping cycles were conducted at each unique testing point the values of the longitudinal modulus of elasticity at the top and bottom of the 95% confidence interval for each cycle were used to calculate the average modulus as well as the 95% confidence interval for that value. This method was used so that the uncertainty of each

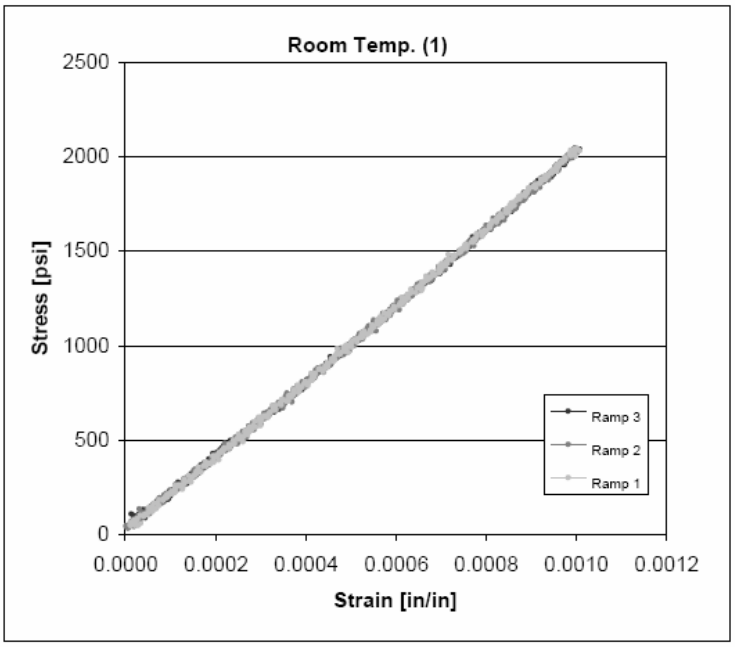

Ramp 1	N = 407
Slope =	2018.704 ksi
R^2 =	0.9994
SE_{slope} =	2.535 ksi
95% CI =	4.9825 ksi

Ramp 2	N = 406
Slope =	2000.611 ksi
R^2 =	0.9993
SE_{slope} =	2.670 ksi
95% CI =	5.2491 ksi

Ramp 3	N = 406
Slope =	2002.649 ksi
R^2 =	0.9993
SE_{slope} =	2.649 ksi
95% CI =	5.2070 ksi

Total	N = 1219
Slope =	2007.3216 ksi
SD =	10.5055 ksi
SE =	4.28884522 ksi
95% CI =	11.0248 ksi

(A) **(B)**

Figure 4.1 - Example of Three Ramping Cycles and Obtained Analytical Data (A) Graph of Each Ramp Cycle and (B) Analytical Data That Was Obtained

ramping cycle would migrate to the 95% confidence intervals used with the overall average experimental value of the modulus. This can be seen in practice in Figure 4.7 and Figure 4.8.

4.3. Overall Sample Behavior and Ultimate Strength

The overall behavior and ultimate strength tests were conducted to provide a better understanding of the stiffness response of the GFRP samples throughout the entire stress-strain envelope. As mentioned in chapter 3 the ultimate strength test first loaded and unloaded the sample to 3000, 5000, and 10,000 micro-strain. The testing results showed a steady degradation in the longitudinal modulus of elasticity as the strain level increased for both fiber arrangements, although a more severe degradation was seen in the biaxial samples. The results of a representative biaxial and uniaxial sample can be seen in Figure 4.2 and Figure 4.3 respectively. It should be pointed out that the modulus used here was based on only one ramping cycle and that the sample at times did not show true linear elastic behavior. Both the biaxial and uniaxial test samples show a slight curve inwards when loaded to 10,000 micro-strain, although the curve in the biaxial sample is more sever. Therefore the longitudinal modulus of elasticity and subsequently the percent change in the modulus are not truly accurate. Due to the fact that the stress-strain curve showed a steeper slope at the beginning and a slightly flatter slope near 10,000 micro-strain it can be assumed the degree of degradation to the modulus is larger than the calculated values.

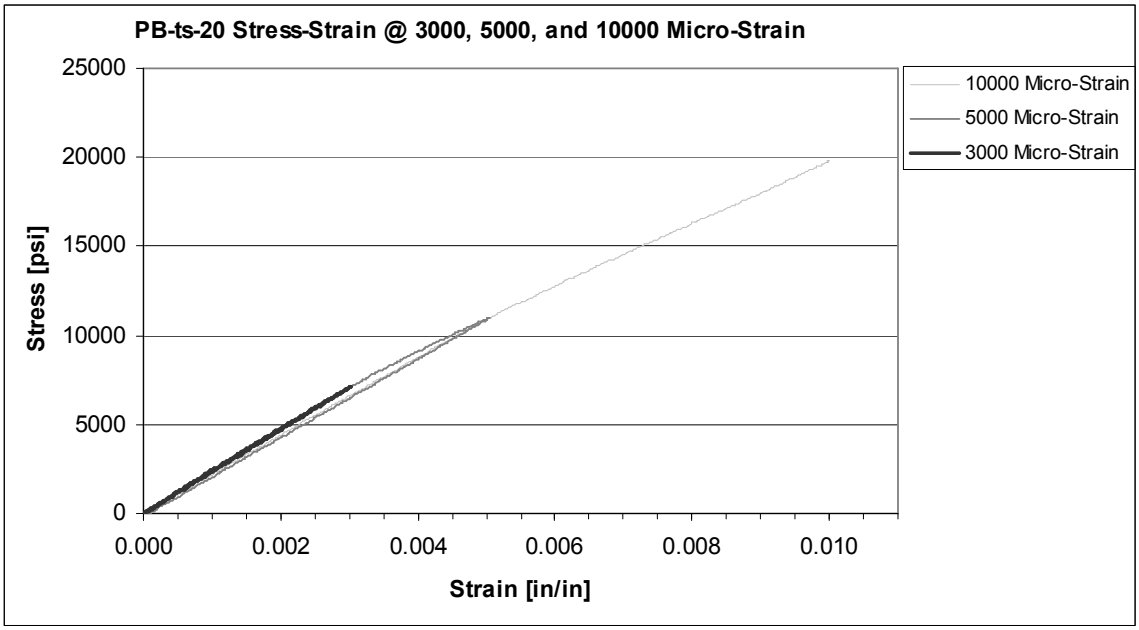

(A)

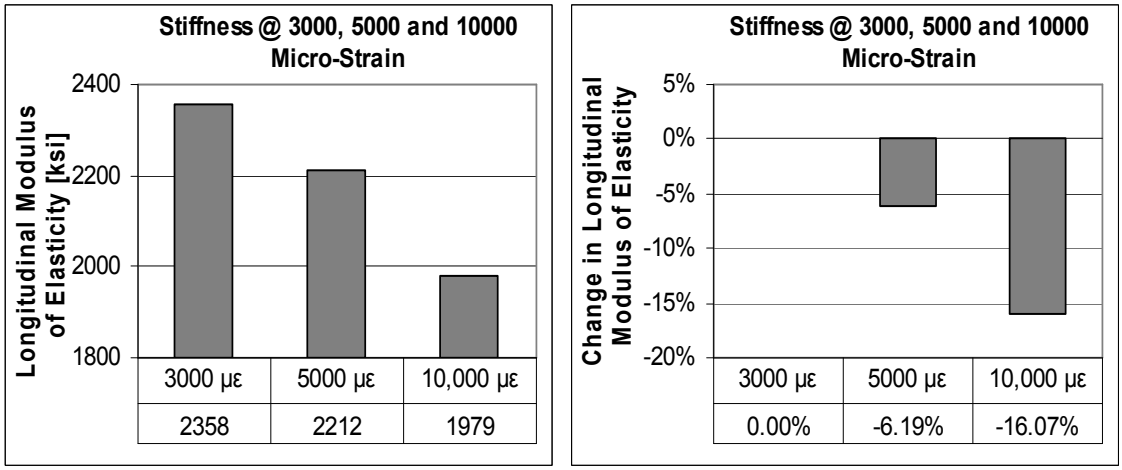

(B)

Figure 4.2 - Longitudinal Modulus of Elasticity For Strength Sample PB-ts-20
(A) Stress-Strain Graph, and (B) Stiffness Values and Degradation

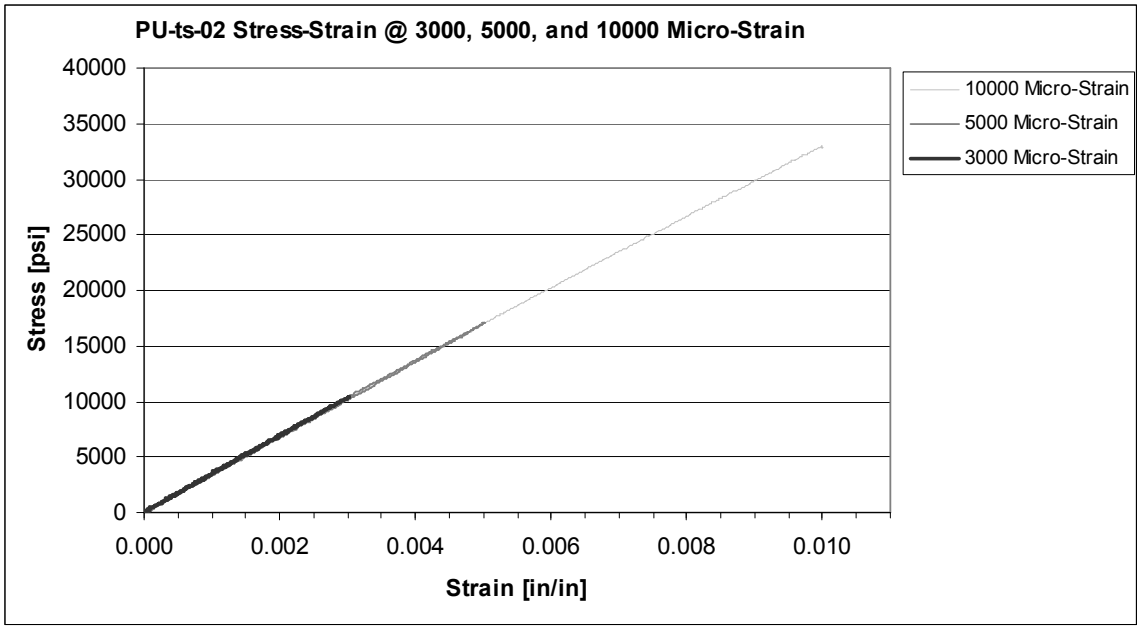

(A)

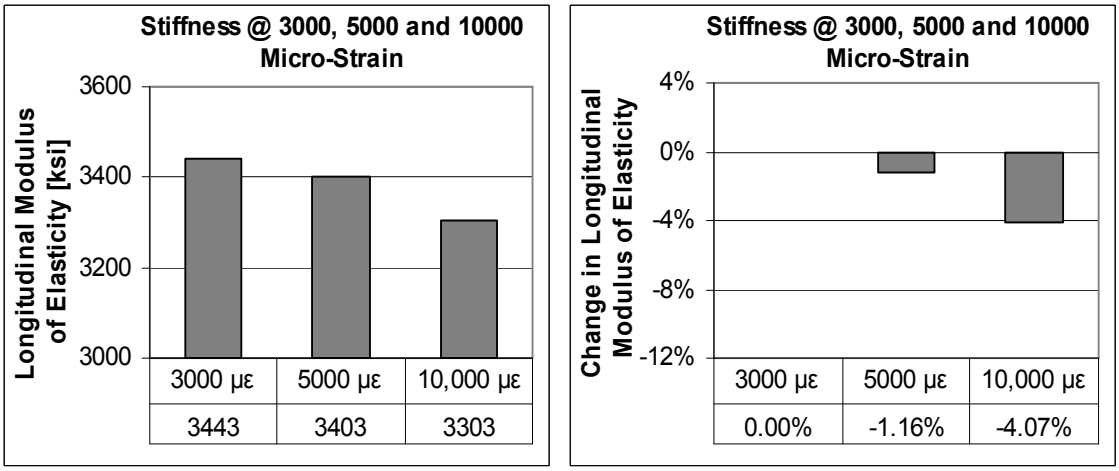

(B)

Figure 4.3 -Longitudinal Modulus of Elasticity for Strength Sample PU-ts-02
(A) Stress-Strain Graph, and (B) Stiffness Values and Degradation

After reaching 10,000 micro-strain each strength sample was loaded to failure. The overall stress-strain curve up to sample failure as well as a post failure picture for the same biaxial and uniaxial samples can be seen in Figure 4.4 and Figure 4.5 respectively. The stress-strain relationship for the GFRP samples remain fairly linear up to failure, but evidence of small areas of localized failure or sample damage can be seen at various places. During the tests a moderately consistent popping noise could be discerned at most strains above 5000 micro-strain, and periodic sharp pops were noted during the last 5000 to 7000 micro-strain. These sharp pops seem to correspond to the localized failures seen in the overall stress-strain failure curves. It should also be noted that the sample failure was typically explosive on the reverse side, but the failure on the smooth front of the sample was usually moderately localized. This phenomenon occurred due to the fabrication process involved in creating the sample sheets. When the samples were made a thin layer of continuous strand mat (CSM) was used as a bonding layer, and created a smooth face while the reverse side lacked this layer and left the fibers unprotected. The unprotected fibers failed explosively while the CSM layer protected the fibers on the front, but evidence of the front fibers debonding from the CSM layer is evident in the post failure pictures.

4.4. Low-Temperature Coupled with Strain Tests

The low-temperature coupled with strain tests can be arranged into two main categories. The first category was concerned with obtaining the longitudinal modulus of elasticity for both the uniaxial and biaxial e-glass/polyester samples at various low temperatures under strain levels similar to the service load strains observed in Choppali's

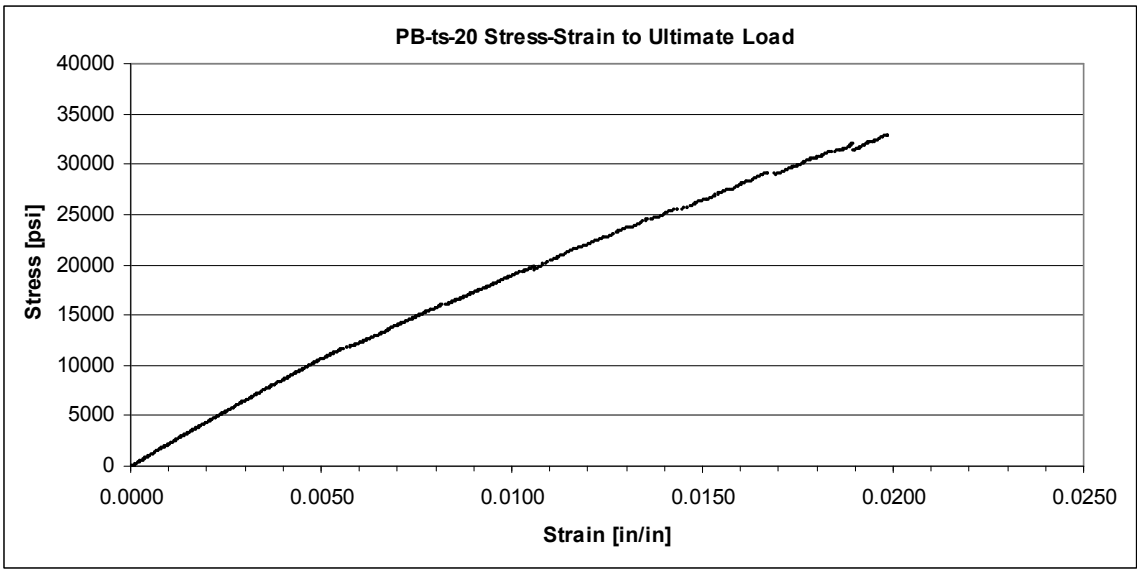

(A)

(B)

Figure 4.4 - Biaxial Strength Sample PB-ts-20
(A) Stress-Strain to Ultimate Load and (B) Post Failure Picture

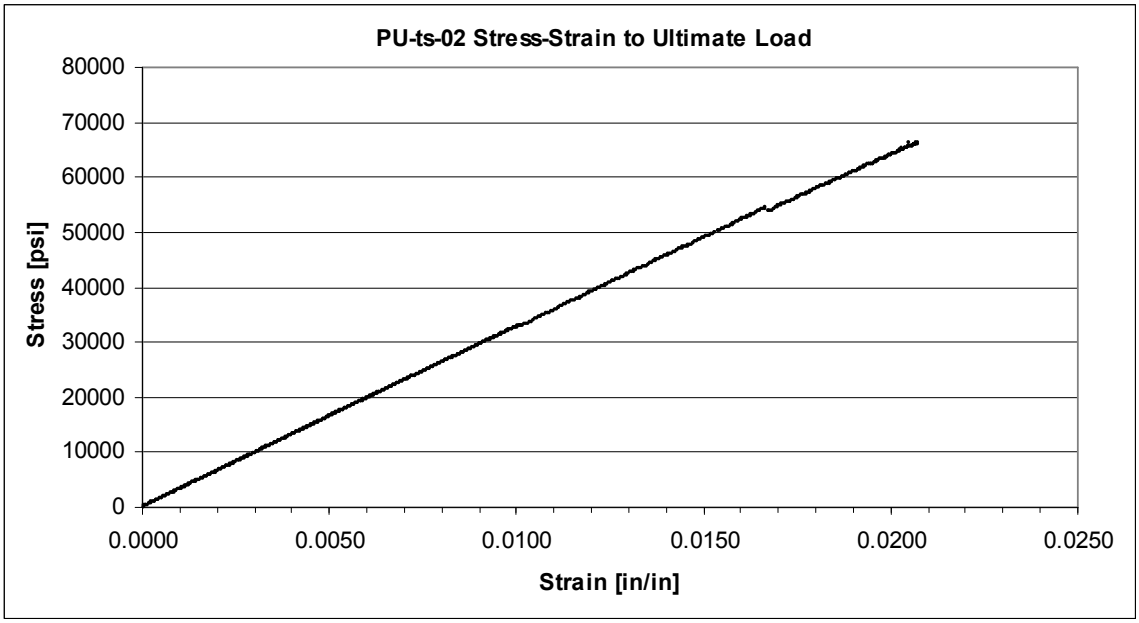

(A)

(B)

Figure 4.5 - Uniaxial Strength Sample PU-ts-02
(A) Stress-Strain to Ultimate Load and (B) Post Failure Picture

panel tests which were just under 1,000 micro-strain. The second category involved raising the strain levels up to 2,000 and then 3,000 micro-strain so that the affect on the longitudinal modulus of elasticity from low temperatures coupled with various elevated strain levels could be determined.

4.4.1. Detailed Overview of One Test Sample

To help clarify the testing results it is advantageous to present a detailed analysis of one test sample, in this case the biaxial test sample PB-ts-11, which was tested to 1000 micro-strain. The sample was inserted into the grips of an MTS testing system equipped with a cooling chamber, and then the sample was tested using a strain controlled procedure. Axial tension was applied to the test sample to maintain a constant axial strain increase of 25 micro-strain per second. The sample was loaded until the axial strain reached 1000 micro-strain, after which the sample was unloaded at the same rate until the axial strain reached zero. This ramp up and down cycle was repeated two more times so that the reproducibility of the experimental data could be verified. After all three ramping cycles were completed the MTS system was switched over to a force controlled holding procedure where the test sample was held at zero force. At this time the cooling chamber was sealed and the chamber temperature was reduced to 32 °F and then allowed to equalize for roughly three hours. After the chamber equalized the test sample was again subjected to the three ramping cycles previously mentioned. The whole procedure was repeated at -4 °F and -31 °F. After the -31 °F test the sample was removed and the whole MTS system and cooling chamber were warmed back up to room temperature and allowed to sit overnight. The sample was tested a final time at room to

determine if any permanent degradation in the modulus had occurred during the low temperature tests. The test sample was fitted with three thermocouples, two thermocouples roughly an inch from each grip and a third thermocouple at the center of the gauge length, the temperature profile for the PB-ts-11 test sample can be seen in Figure 4.6. It should be noted that while the chamber thermocouple and the center thermocouple both typically remained very close to the target temperature, the two thermocouples near each grip showed a noticeably slower response and difficulty reaching -31 °F. This was most likely due to the large thermo mass of each grip.

After the test was completed the load transducer and extensometer data were used to compute the longitudinal modulus of elasticity as well as the 95% confidence intervals

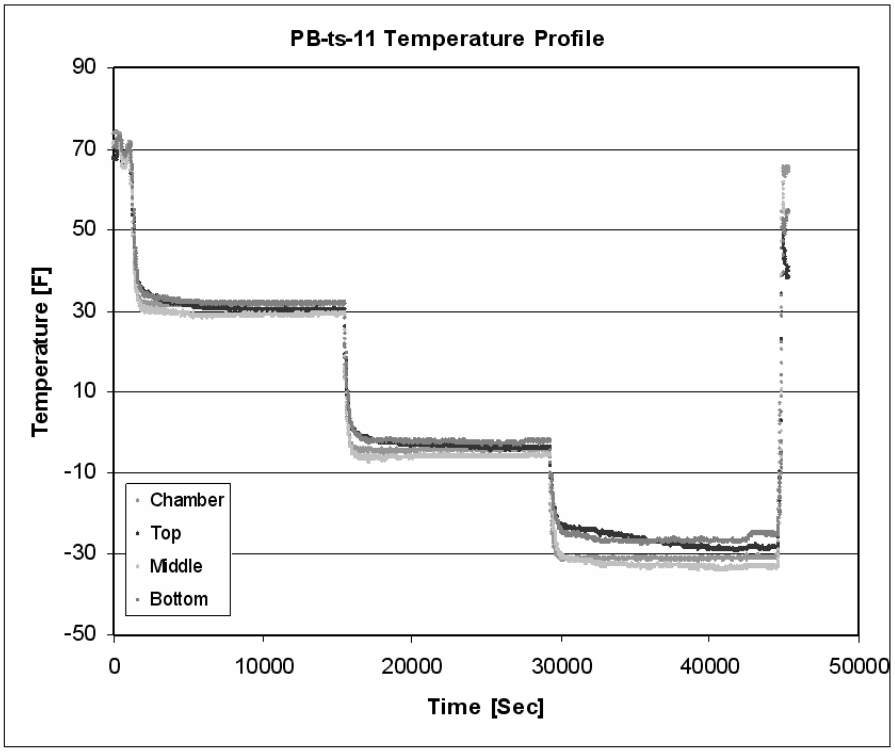

Figure 4.6 – Temperature Profile of Test Sample PB-ts-11

of each ramping cycle as described in section 4.2. The results of each ramping cycle for test sample PB-ts-11 can be seen in Figure 4.7. It can be seen that the modulus of each ramping cycle at a given temperature typically matches closely with the other two cycles, and that the error bars signifying 95% confidence range are fairly small. The small confidence range means a linear model generally accounts for all the data obtained. The fact that each of the three ramping cycles match closely with each other show that the modulus values obtained could be reproduced if tested again, meaning there was not a testing fluke or other event that cause an erroneous data reading. These trends are similar throughout all the other test samples.

To ease the presentation of the test data the three individual ramping cycles were averaged and new confidence intervals were calculated for the average value. The average longitudinal modulus of elasticity of each cycle for test sample PB-ts-11 is shown in Figure 4.8. When compared with Figure 4.7 it can be seen that the confidence intervals of the average modulus is small for temperatures where all three cycles showed a small confidence interval and the individual longitudinal modulus of each cycle closely matched. Where this is not the case a larger confidence interval is shown, signifying either large uncertainty in the individual cycles or a discrepancy between the modulus values obtained from each cycle.

The test sample was retested at room temperature to determine if the longitudinal modulus of elasticity showed any degradation and if so to what degree. The test sample showed minimal degradation of the modulus (Figure 4.9) as was typical for the service load strains, which are further detailed in section 4.4.2.

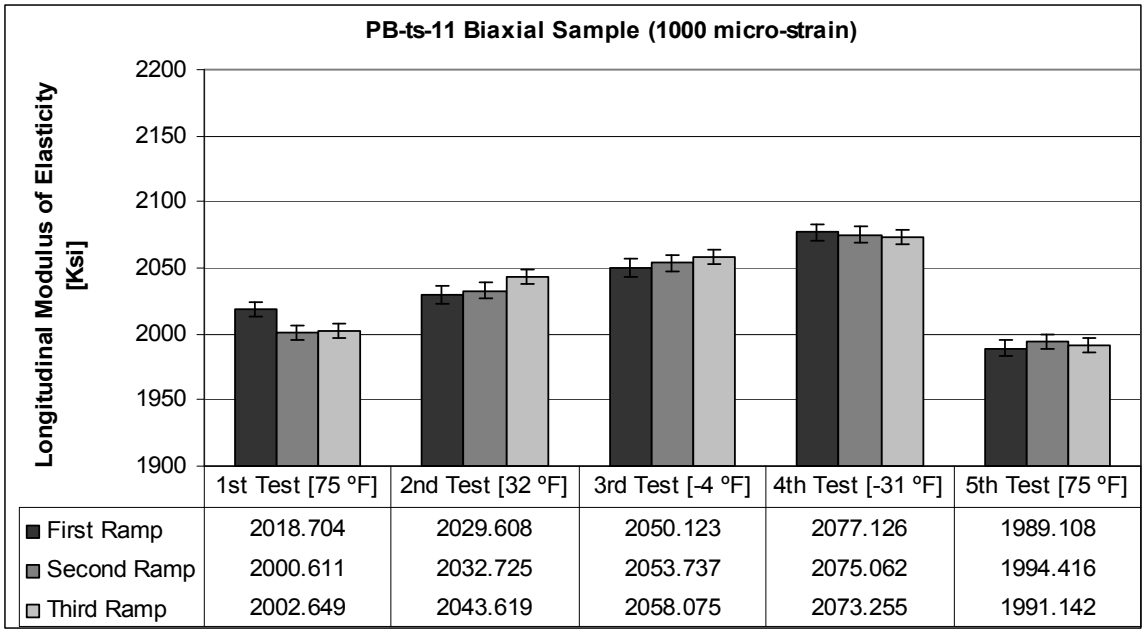

Figure 4.7 - Longitudinal Modulus of Elasticity for Test Sample PB-ts-11

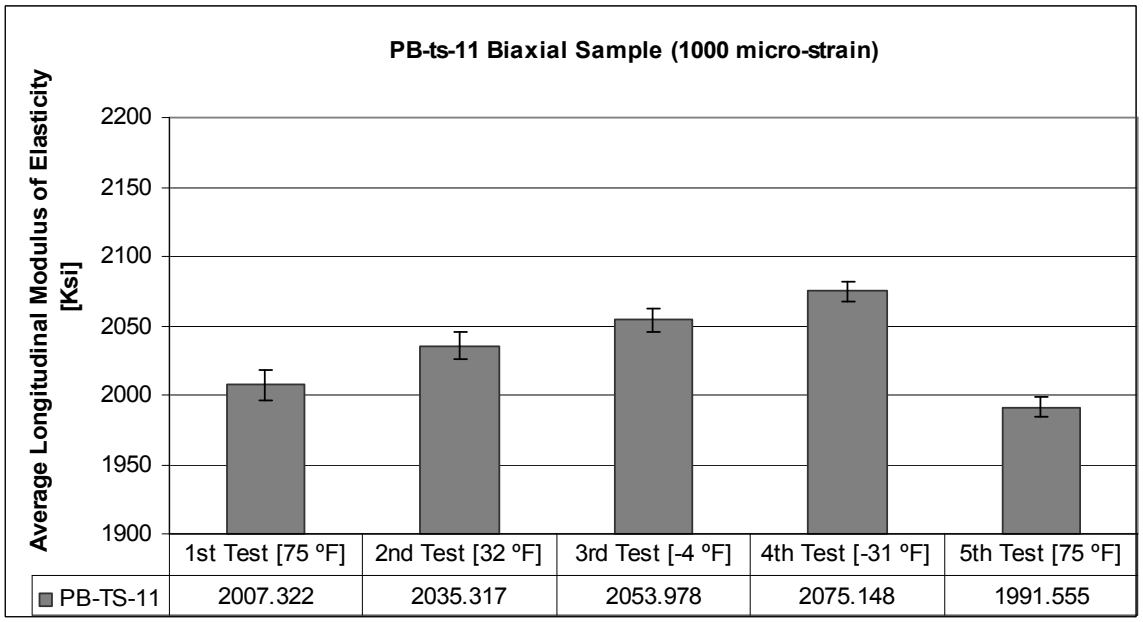

Figure 4.8 - Average Longitudinal Modulus of Elasticity for Test Sample PB-ts-11

4.4.2. Effects of Low-Temperature Coupled with Service Load Strains

The low temperature effects on the longitudinal modulus of elasticity were tested at the service load strains seen in Ma and Choppali's deck panel test (Ma, Choppali 2007). These service load strains were roughly 1000 micro-strain which is very small in comparison to the ultimate strain levels seen in the strength tests. In fact service load levels are roughly 6% of the ultimate strain levels. The low temperature tests involved loading and unloading a sample to 1000 micro-strain three times at each temperature and then warming the sample back up to room temperature to check for degradation in the modulus. Therefore during the entire test the sample was subjected to 15 load cycles. The average modulus of elasticity for both biaxial samples is shown in Figure 4.10. Both samples show a steady increase in the longitudinal modulus as the temperature is reduced, and seem to show no permanent degradation of the modulus. This can be seen

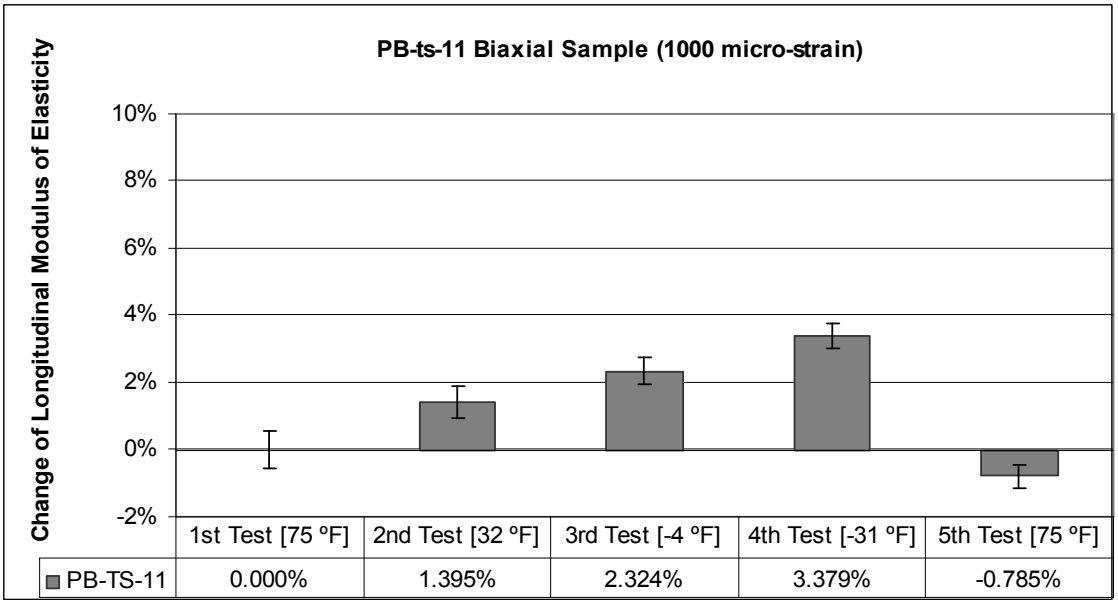

Figure 4.9 - Change in Modulus of Elasticisty for Test Sample PB-ts-11

clearer when the percent change in the longitudinal modulus of the same biaxial samples is shown in Figure 4.11. When returned to room temperature and retested there is less than 1% difference between the first and last test. This same trend is seen when the results of the uniaxial samples are observed. The average modulus of elasticity and the percent change in modulus for the uniaxial samples can be seen in Figure 4.12 and Figure 4.13 respectively. It is evident that both biaxial and uniaxial fiber arrangements show a continual increase in the longitudinal modulus of elasticity as the temperature decreases, and nether fiber arrangement show any degradation of the modulus after being tested. This shows that the stiffness transition and degradation seen in Ma and Choppali's panel test around -4°F was most likely not due to a degradation in the stiffness of the face sheets within the sandwich panel.

Although there is a consistent increase in the modulus as the temperature is lowered, the rate of increase does not seem to be the same between samples. The percent change in modulus verses the temperature for both biaxial and uniaxial samples can be seen in Figure 4.14. The rate the longitudinal modulus of elasticity increases seems to be fairly linear for all the test samples, but the slope of the increase varies drastically between each sample. Once again the consistency of the uniaxial samples seems to be greater than the biaxial samples but overall neither type shows close enough convergence to determine a typical rate of increase.

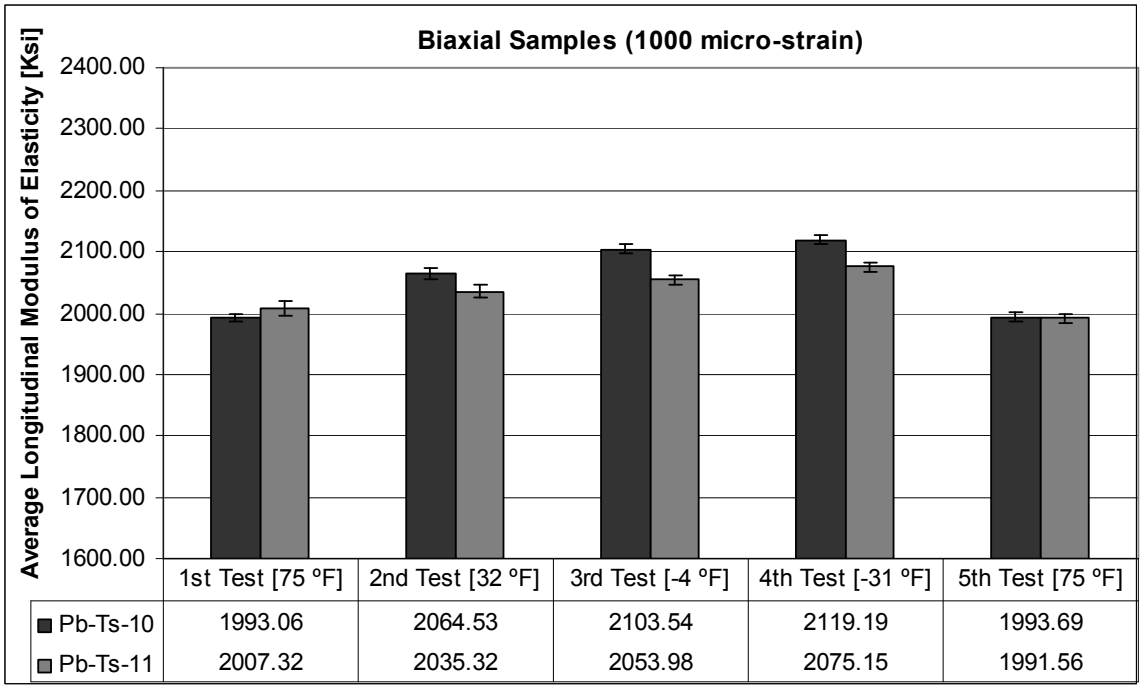

Figure 4.10 – Average Modulus for Biaxial Samples at 1000 Micro-Strain

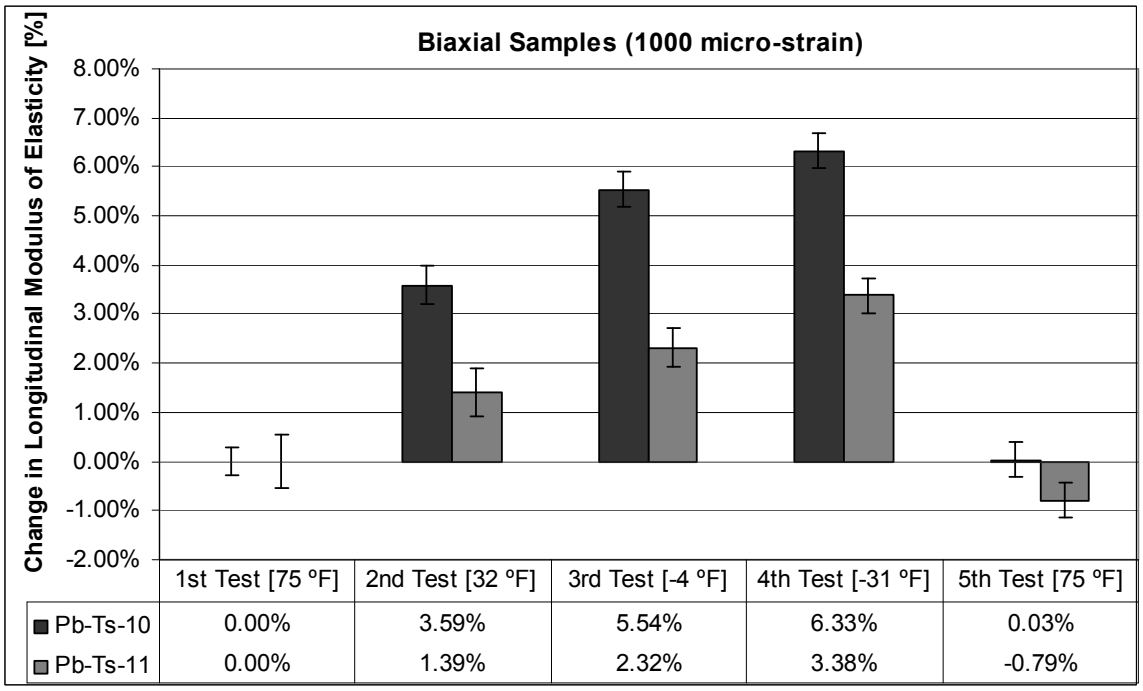

Figure 4.11 – Change in Modulus for Biaxial Samples at 1000 Micro-Strain

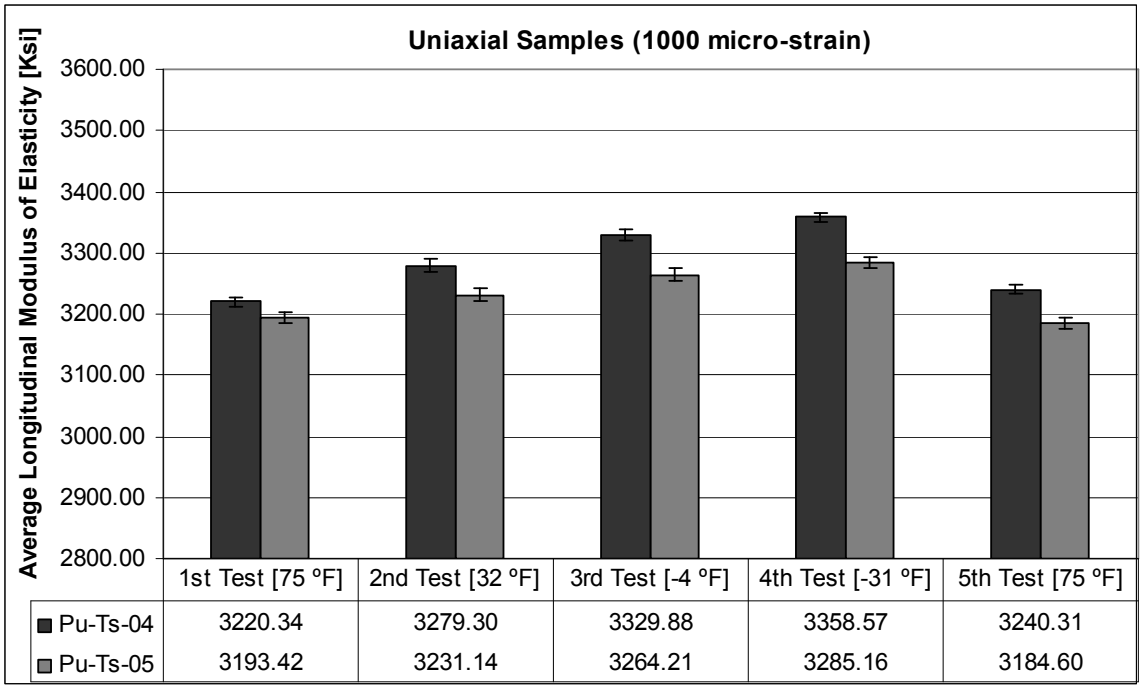

Figure 4.12 - Average Modulus for Uniaxial Samples at 1000 Micro-Strain

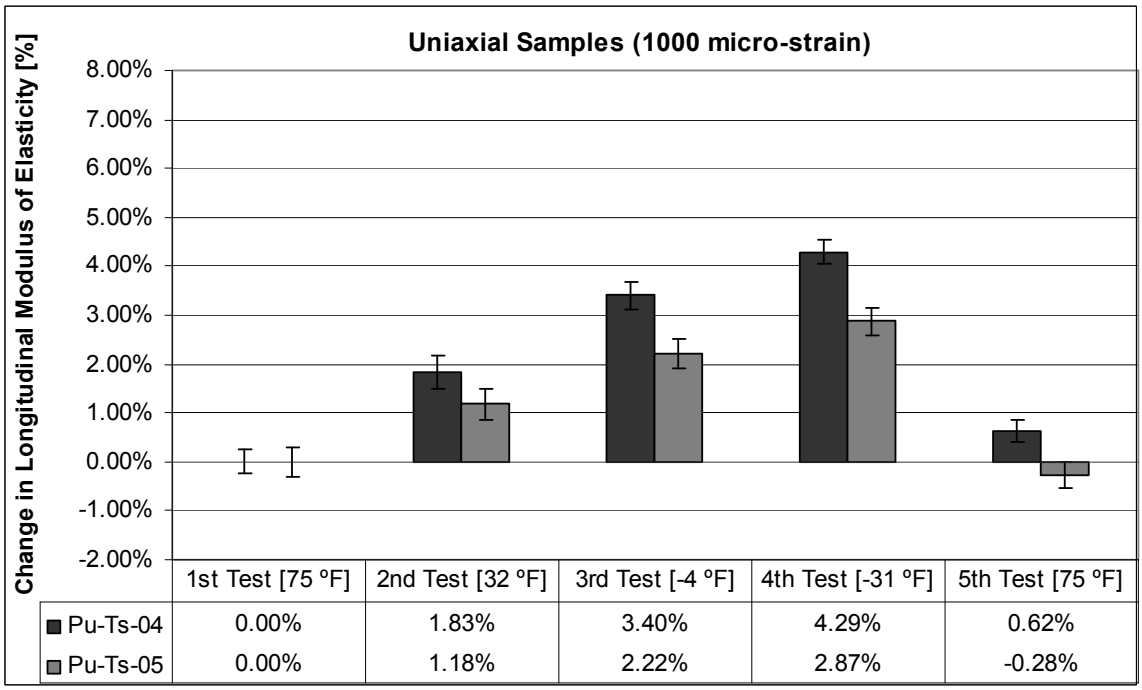

Figure 4.13 – Change in Modulus for Uniaxial Samples at 1000 Micro-Strain

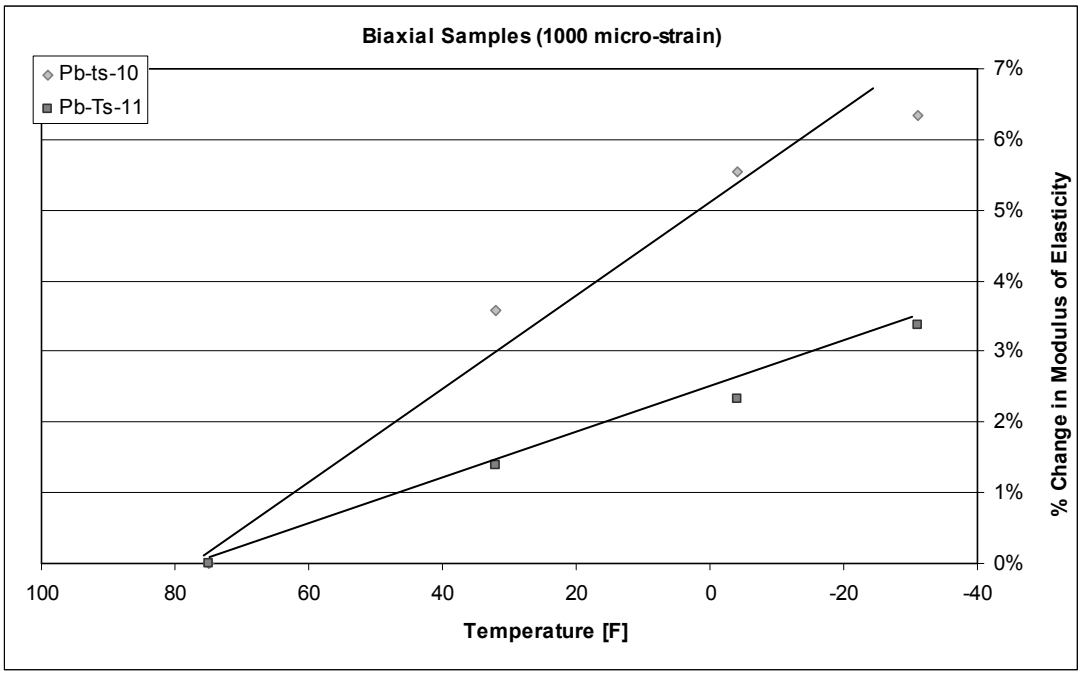

(A)

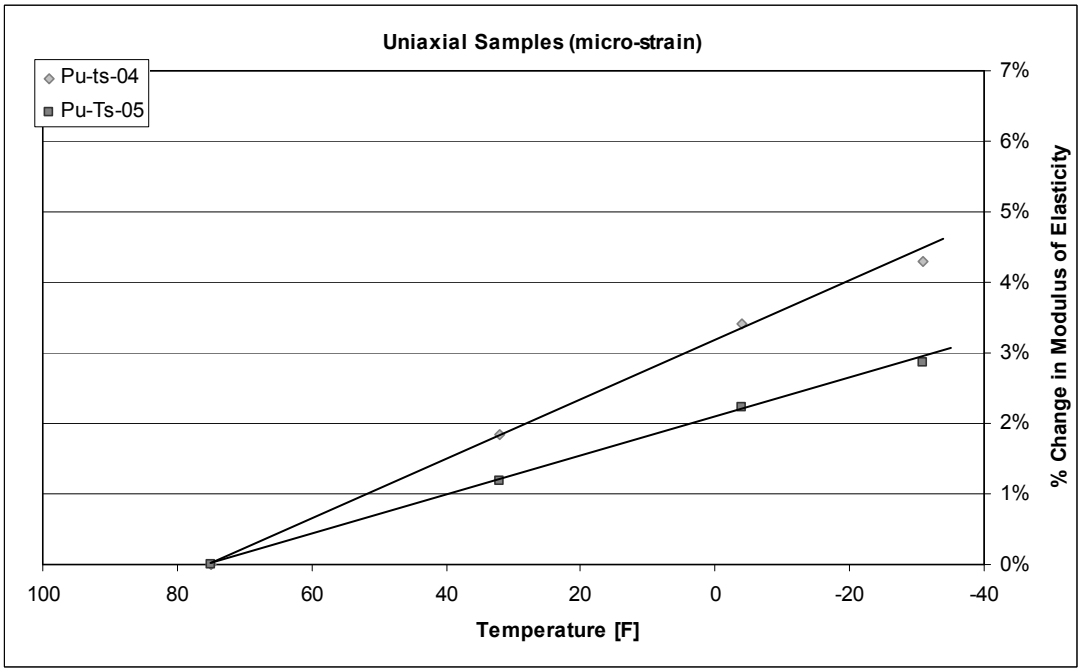

(B)

Figure 4.14 – Change in Modulus of Elasticity vs. Temperature
(A) Biaxial Samples and, (B) Uniaxial Samples

4.4.3. Effects of Low-Temperature Coupled with Elevated Stain Levels

The impact of both low temperatures and increased strain levels was investigated by repeating the same type of tests used to observe the effects of low temperature coupled with service load strains but at higher strain levels. The strain levels were chosen after initial tests showed a significant degradation in the longitudinal modulus of elasticity after subjecting initial test samples to strains up to 3000 micro-strain. It was decided that the 2000 and 3000 micro-strain levels should give a decent view of the material response around the strain levels that will typically be seen in structural applications. 2000 micro-strain is roughly 12% of the ultimate strain and 3000 micro-strain corresponds to nearly 18% of the ultimate. The change in the modulus of elasticity for both biaxial and uniaxial test samples subjected to 2000 micro-strain can be seen in Figure 4.15. A noticeable degradation in the modulus can be seen when comparing the first and last room temperature tests. The longitudinal modulus is roughly 3-5% lower after testing the biaxial samples and is around 2-4% lower after testing the uniaxial samples. In general the error bars denoting a 95% confidence interval were small signifying a low level of uncertainty associated with the data collected. The change in the longitudinal modulus of elasticity for the test samples subjected to 3000 micro-strain can be seen in Figure 4.16. Once again a degradation in the modulus is seen. The longitudinal modulus is roughly 9-16% lower after testing the biaxial samples and is around 3-5% lower after testing the uniaxial samples.

During the ultimate strength test it was noticed that the longitudinal modulus degraded as the strain level increased so it can be assumed that the modulus would degrade to some degree during the 15 loading cycles each sample was subjected to even

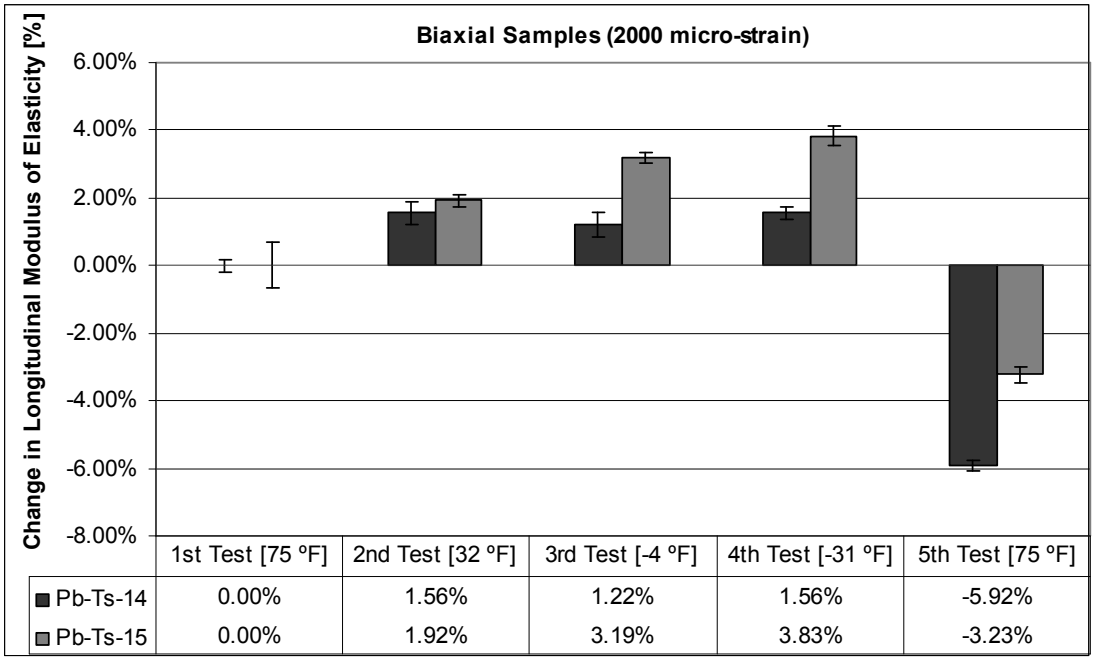

	1st Test [75 ºF]	2nd Test [32 ºF]	3rd Test [-4 ºF]	4th Test [-31 ºF]	5th Test [75 ºF]
Pb-Ts-14	0.00%	1.56%	1.22%	1.56%	-5.92%
Pb-Ts-15	0.00%	1.92%	3.19%	3.83%	-3.23%

(A)

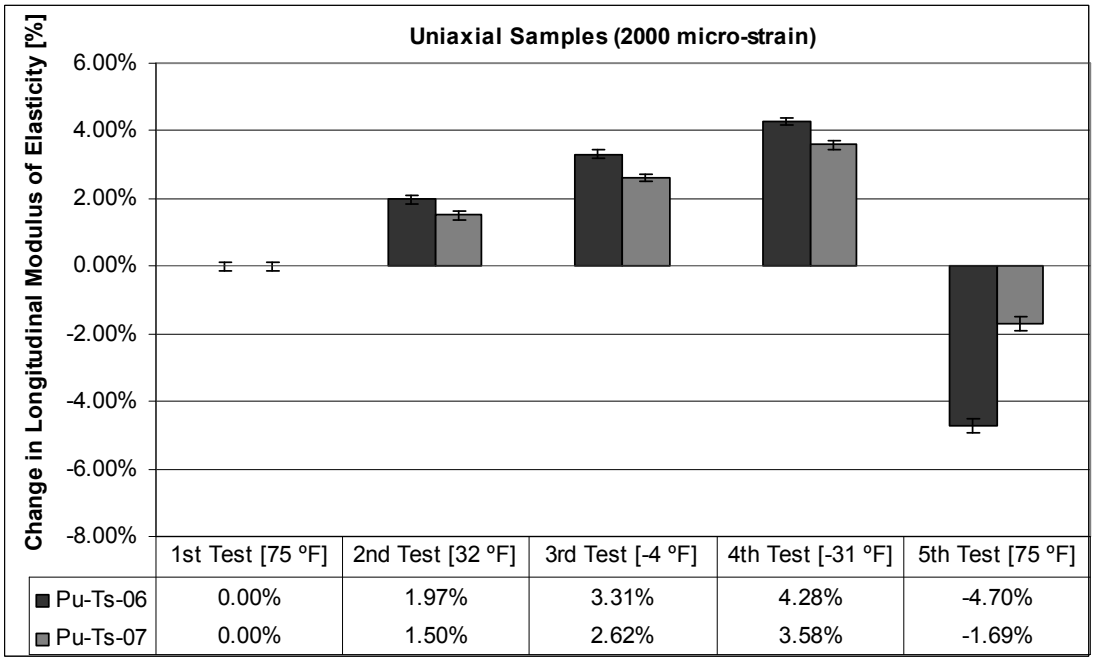

	1st Test [75 ºF]	2nd Test [32 ºF]	3rd Test [-4 ºF]	4th Test [-31 ºF]	5th Test [75 ºF]
Pu-Ts-06	0.00%	1.97%	3.31%	4.28%	-4.70%
Pu-Ts-07	0.00%	1.50%	2.62%	3.58%	-1.69%

(B)

Figure 4.15 – Change in Modulus of Elasticity for Samples at 2000 Micro-Strain (A)Biaxial Samples and, (B) Uniaxial Samples

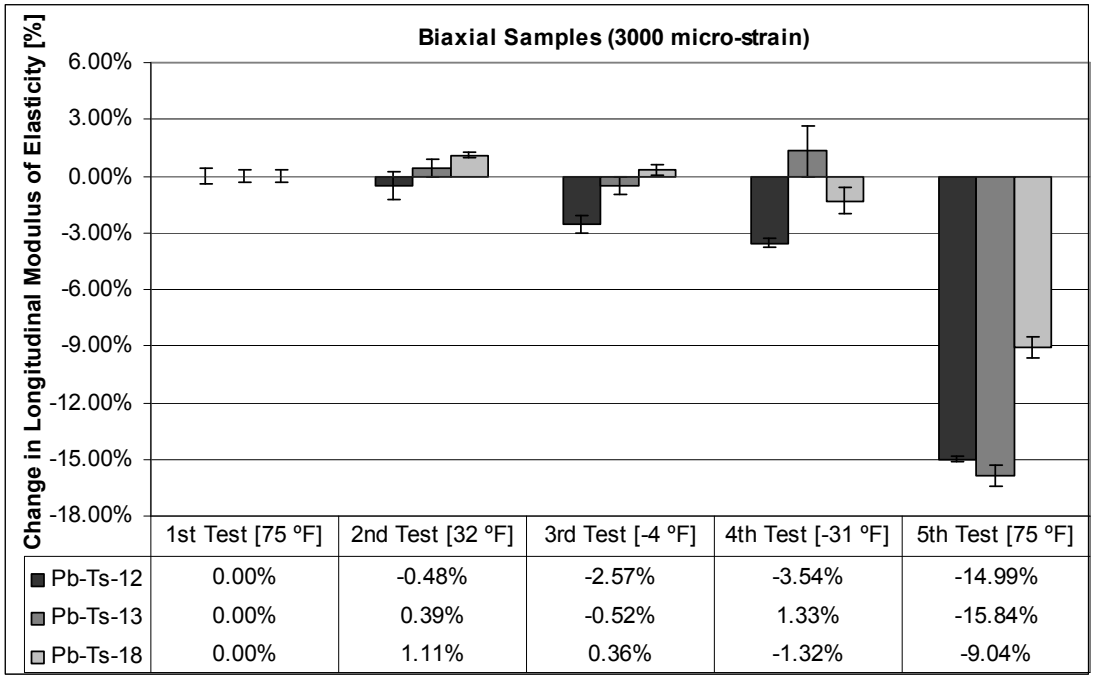

	1st Test [75 ºF]	2nd Test [32 ºF]	3rd Test [-4 ºF]	4th Test [-31 ºF]	5th Test [75 ºF]
Pb-Ts-12	0.00%	-0.48%	-2.57%	-3.54%	-14.99%
Pb-Ts-13	0.00%	0.39%	-0.52%	1.33%	-15.84%
Pb-Ts-18	0.00%	1.11%	0.36%	-1.32%	-9.04%

(A)

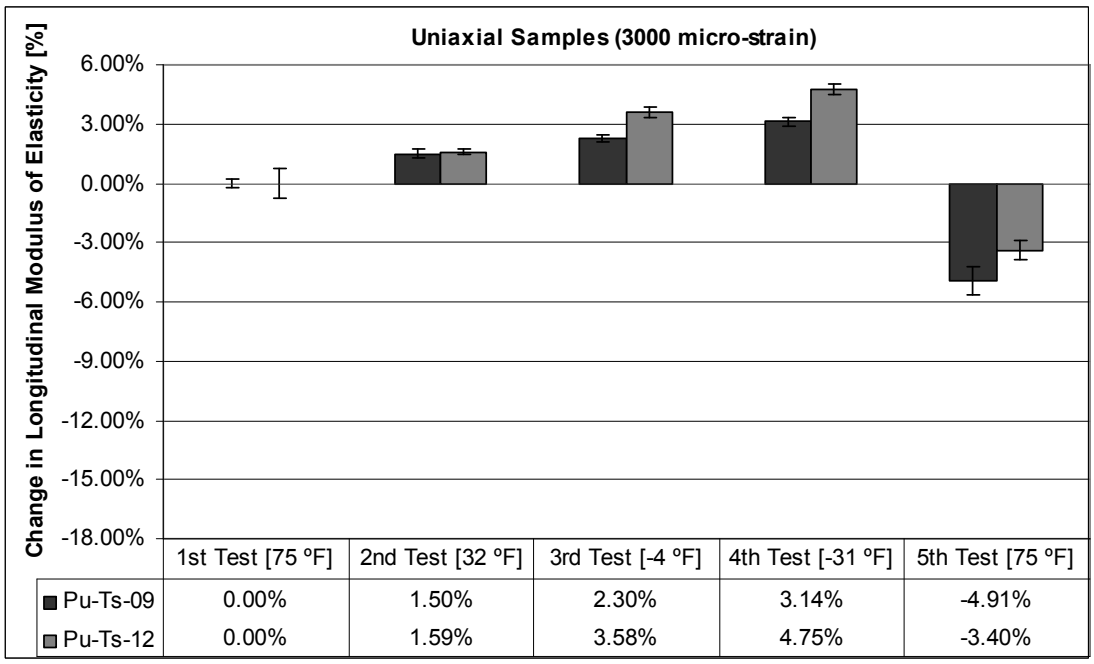

	1st Test [75 ºF]	2nd Test [32 ºF]	3rd Test [-4 ºF]	4th Test [-31 ºF]	5th Test [75 ºF]
Pu-Ts-09	0.00%	1.50%	2.30%	3.14%	-4.91%
Pu-Ts-12	0.00%	1.59%	3.58%	4.75%	-3.40%

(B)

Figure 4.16 - Change in Modulus of Elasticity for Samples at 3000 Micro-Strain (A)Biaxial Samples and, (B) Uniaxial Samples

if the samples were kept at room temperatures. Therefore a control sample of each fiber arrangement was tested for the 15 load cycles at room temperature. Control samples for both 2000 and 3000 micro-strain levels were tested in a manor similar to the low-temperature tests. Although the biaxial sample showed a small degree of degradation to the modulus, the uniaxial sample showed very little degradation. When compared to the low temperature test the degradation seen in the control samples was significantly less than that seen during the low temperature tests. The change in the longitudinal modulus of elasticity of the biaxial samples when compared to the control samples for each strain level can be seen in Figure 4.17. The overall results of the uniaxial samples can be seen in Figure 4.18.

4.5. Analysis of the Testing Results

The overall testing program showed that the stiffness of GFRP samples increased as the temperature was lowered and did not show degradation in the longitudinal modulus when the strains remained below 1000 micro-strain. These results show that the transition from increasing to decreasing stiffness seen in a low-temperature GFRP deck panel test conducted by Choppali was likely due to partial debonding or some other structural phenomenon. The steady increase in modulus as temperature decreases is also consistent with the literature review that was conducted. Dutta and Hui found that pultruded E-glass samples showed a trend of increased stiffness at lower temperatures (Dutta, Hui 1996). Only two samples of each material type were tested at 1000 micro-strain, and although both samples showed a nearly linear increase in stiffness with temperature the slope of the increase varied quiet significantly between the samples.

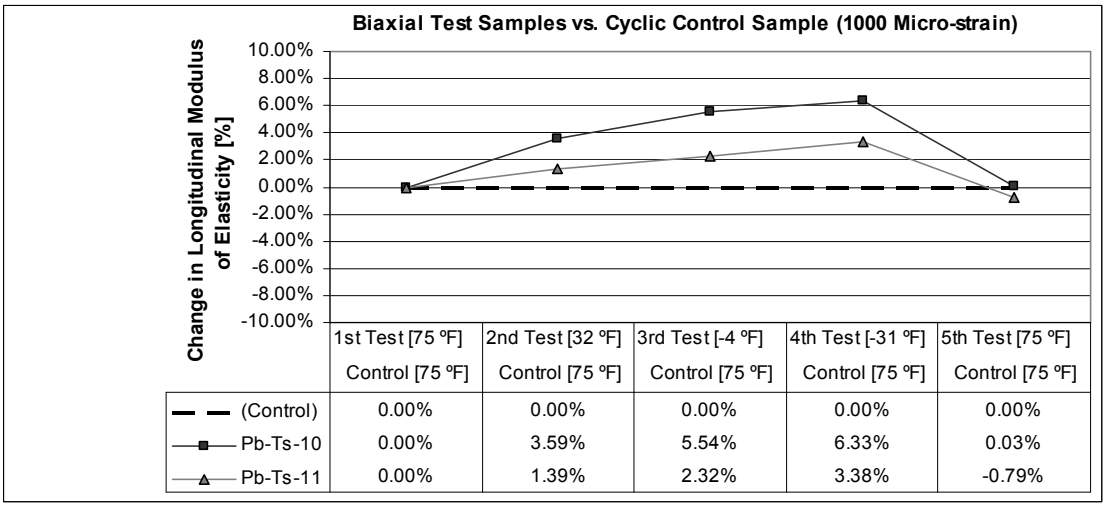

	1st Test [75 ºF] Control [75 ºF]	2nd Test [32 ºF] Control [75 ºF]	3rd Test [-4 ºF] Control [75 ºF]	4th Test [-31 ºF] Control [75 ºF]	5th Test [75 ºF] Control [75 ºF]
(Control)	0.00%	0.00%	0.00%	0.00%	0.00%
Pb-Ts-10	0.00%	3.59%	5.54%	6.33%	0.03%
Pb-Ts-11	0.00%	1.39%	2.32%	3.38%	-0.79%

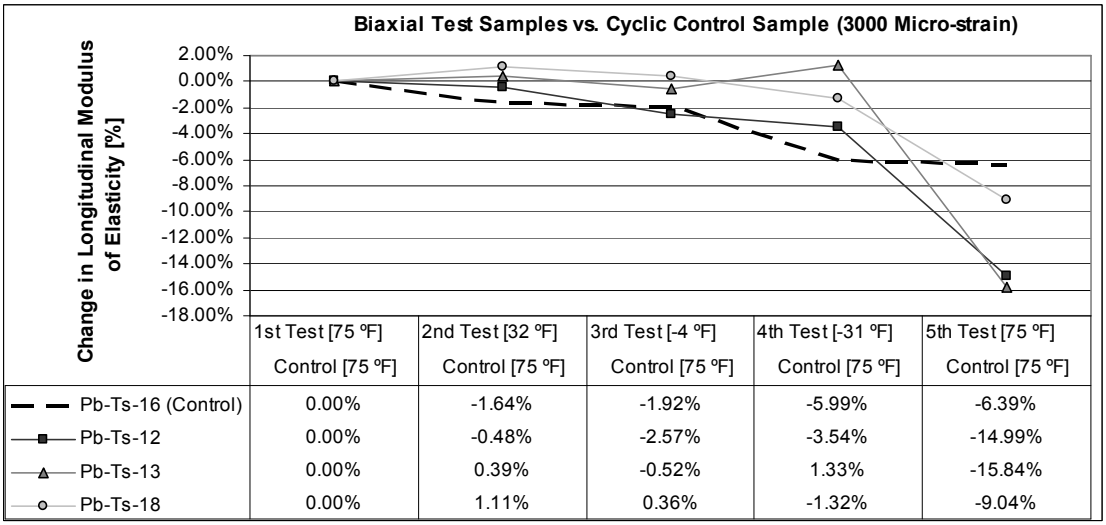

	1st Test [75 ºF] Control [75 ºF]	2nd Test [32 ºF] Control [75 ºF]	3rd Test [-4 ºF] Control [75 ºF]	4th Test [-31 ºF] Control [75 ºF]	5th Test [75 ºF] Control [75 ºF]
Pb-Ts-16 (Control)	0.00%	-1.64%	-1.92%	-5.99%	-6.39%
Pb-Ts-12	0.00%	-0.48%	-2.57%	-3.54%	-14.99%
Pb-Ts-13	0.00%	0.39%	-0.52%	1.33%	-15.84%
Pb-Ts-18	0.00%	1.11%	0.36%	-1.32%	-9.04%

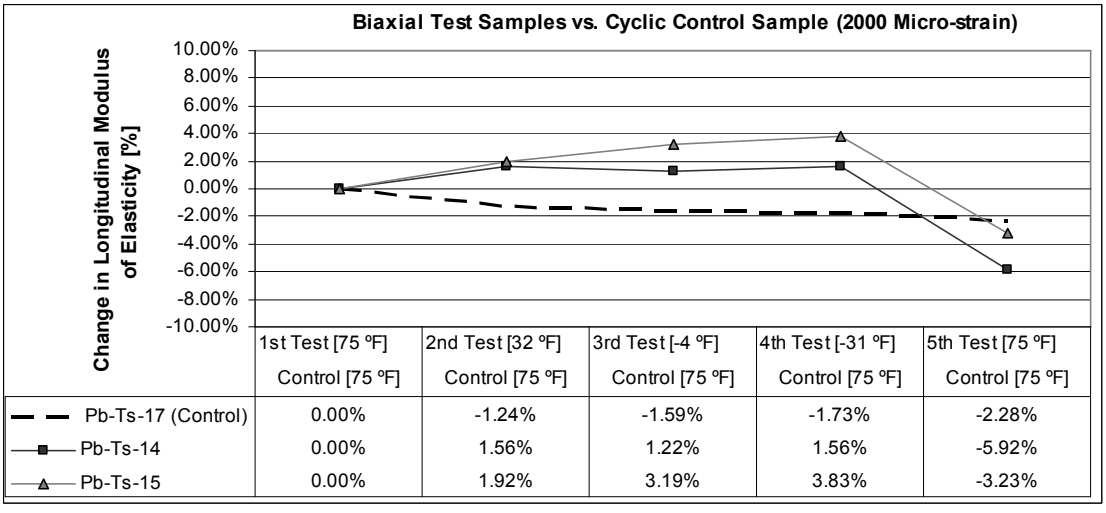

	1st Test [75 ºF] Control [75 ºF]	2nd Test [32 ºF] Control [75 ºF]	3rd Test [-4 ºF] Control [75 ºF]	4th Test [-31 ºF] Control [75 ºF]	5th Test [75 ºF] Control [75 ºF]
Pb-Ts-17 (Control)	0.00%	-1.24%	-1.59%	-1.73%	-2.28%
Pb-Ts-14	0.00%	1.56%	1.22%	1.56%	-5.92%
Pb-Ts-15	0.00%	1.92%	3.19%	3.83%	-3.23%

Figure 4.17 – Degradation of Modulus for Biaxial Samples at Various Strains

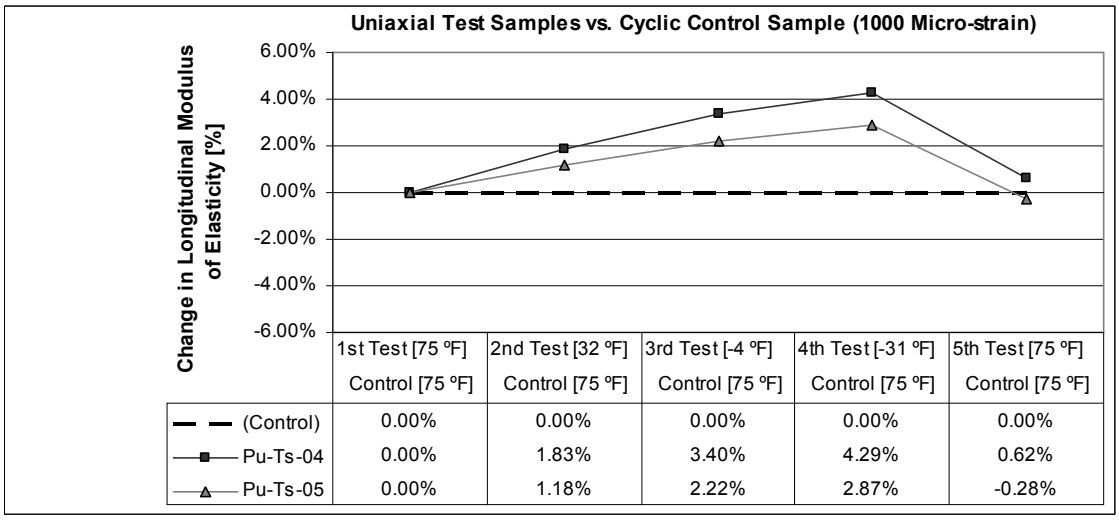

	1st Test [75 ºF] Control [75 ºF]	2nd Test [32 ºF] Control [75 ºF]	3rd Test [-4 ºF] Control [75 ºF]	4th Test [-31 ºF] Control [75 ºF]	5th Test [75 ºF] Control [75 ºF]
(Control)	0.00%	0.00%	0.00%	0.00%	0.00%
Pu-Ts-04	0.00%	1.83%	3.40%	4.29%	0.62%
Pu-Ts-05	0.00%	1.18%	2.22%	2.87%	-0.28%

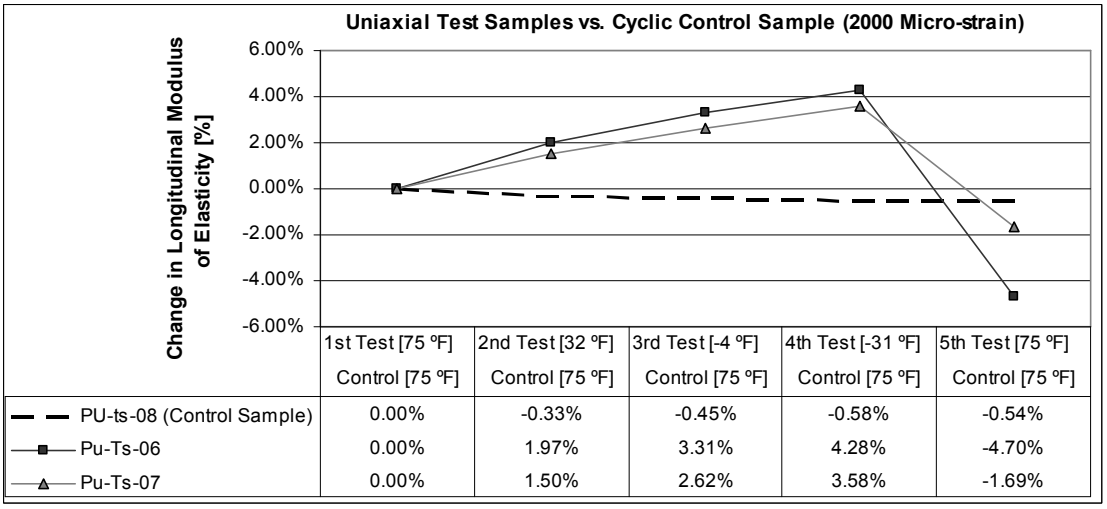

	1st Test [75 ºF] Control [75 ºF]	2nd Test [32 ºF] Control [75 ºF]	3rd Test [-4 ºF] Control [75 ºF]	4th Test [-31 ºF] Control [75 ºF]	5th Test [75 ºF] Control [75 ºF]
PU-ts-08 (Control Sample)	0.00%	-0.33%	-0.45%	-0.58%	-0.54%
Pu-Ts-06	0.00%	1.97%	3.31%	4.28%	-4.70%
Pu-Ts-07	0.00%	1.50%	2.62%	3.58%	-1.69%

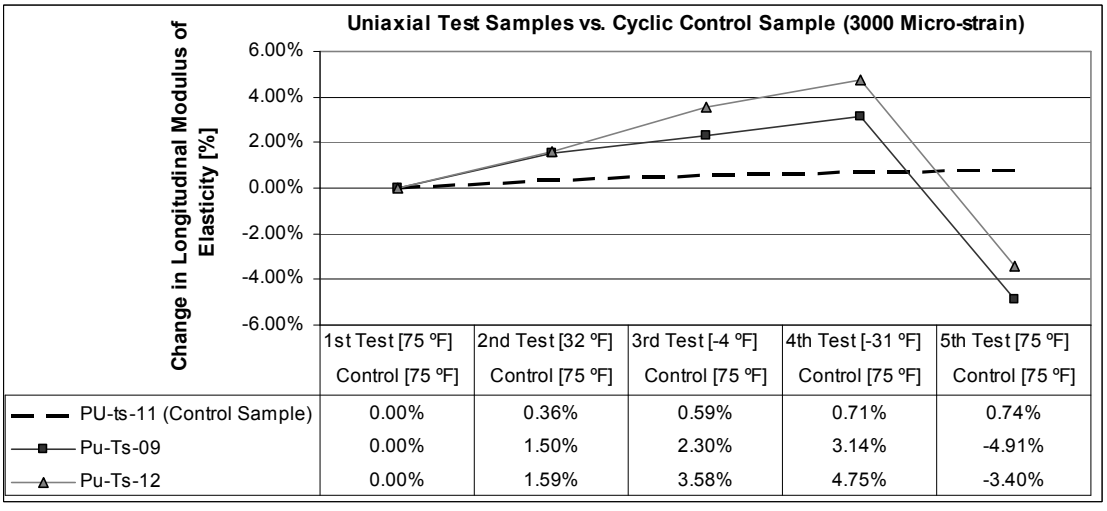

	1st Test [75 ºF] Control [75 ºF]	2nd Test [32 ºF] Control [75 ºF]	3rd Test [-4 ºF] Control [75 ºF]	4th Test [-31 ºF] Control [75 ºF]	5th Test [75 ºF] Control [75 ºF]
PU-ts-11 (Control Sample)	0.00%	0.36%	0.59%	0.71%	0.74%
Pu-Ts-09	0.00%	1.50%	2.30%	3.14%	-4.91%
Pu-Ts-12	0.00%	1.59%	3.58%	4.75%	-3.40%

Figure 4.18 – Degradation of Modulus for Uniaxial Samples at Various Strains

Observing the Figure 4.14 it seems that the rate of stiffness increase in general seems to be less for the uniaxial sample than the matrix dominated biaxial sample.

The average room temperature modulus of elasticity for the uniaxial test samples was 3282 ksi, but the values ranged from 3117 ksi to 3466 ksi. The theoretical estimate based on the rule of mixtures was 3815 ksi. While average room temperature modulus of elasticity for the biaxial test samples was 2116 ksi, but the values ranged from 1981 ksi to 2334 ksi. The theoretical estimate based on the rule of mixtures was 2394 ksi. It should be noted that the values used in the theoretical estimate were the average standard values found during the literature review. The rule of mixture is typically a decent tool for obtaining rough composite material properties, but one of the main assumptions is that there are no voids. A close examination of the GFRP samples show imperfections and small voids periodically throughout the material. The culmination of all the uncertainties associated with the original estimate can account for the variation between the experimental and theoretical values for the modulus of elasticity.

Both uniaxial and biaxial control samples were tested at room temperature in a manor that subjected them to 15 strain load cycles, this is equivalent to the number of ramping cycles seen by the low-temperature samples. The control samples were used to compare any degradation in the modulus of elasticity due strictly to the cyclic strain loads. The test data shows that the uniaxial samples suffered no noticeable degradation in the modulus, while the biaxial samples showed roughly a 6% reduction to the modulus after being tested with a strain limit of 3000 micro-strain.

The effects of low-temperature coupled with various strain levels on the longitudinal modulus of elasticity of GFRP laminates were analyzed by comparing the

room temperature control tests with low-temperature tests conducted at 2000 and 3000 micro-strain. Permanent damage to the modulus was observed in the room temperature control tests when the strain levels were above 2000 micro-strain. When the low-temperature tests were compared to the room temperature tests, noticeably higher levels of degradation of the modulus were observed for the low-temperature tests. Degradation in the longitudinal modulus of elasticity of roughly 15% was observed in the low-temperature biaxial samples that were subjected to a strain level of 3000 micro-strain. When this is compared to the 6% reduction in the modulus observed in the room temperature control samples due strictly to strain-cycling it can be seen that 8% to 9% more degradation occurred due to the combined effect of low-temperature and strain. The uniaxial samples at the 3000 micro-strain limit showed roughly 4% reduction in the modulus of elasticity. The room temperature control samples showed no loss, in fact the modulus slightly increased afterwards, so therefore the entire 4% degradation can be attributed to the combined effect of low-temperature and strain.

The uniaxial test samples showed less degradation of the modulus of elasticity during all phases of testing. This is most likely due to the fact that the uniaxial samples are not controlled by the behavior of the matrix as much as the biaxial samples. The biaxial samples had a significantly larger amount of resin per longitudinal fibers because half of the fibers are oriented in the perpendicular axis. It is commonly understood that resin hardening due to a reduction in temperature causes the matrix to become brittle and therefore increases the potential for permanent damage due to micro-cracking and other phenomena. Although the resin is not the primary strength in FRP materials, the resin does provide a significant part of the strength. If the matrix stiffness is ignored than the

entire stiffness of the sample is reduced. This can be seen in theory by looking at the theoretical modulus of elasticity for both uniaxial and biaxial samples when the matrix is ignored. Based on the rule of mixtures the uniaxial samples had a theoretical modulus of 3815 kis, but if the resin was neglected in the calculations the modulus dropes to 3500 ksi. This is essentially a 8% drop. The biaxial samples on the other hand have a theoretical modulus of 2395 ksi and that drops to 2079 ksi when the matrix is ignored. The biaxial samples see a drop of about 14%. Therefore anything that positively or negatively affects the performance of the resin will typically be more exaggerated in matrix-dominated samples. This helps explain the fact that the biaxial samples seemed to have a larger increase in stiffness as the temperature was reduced. It also helps explain why the biaxial samples showed significantly larger reduction in modulus after testing them at low-temperatures.

The test results for each individual sample fit the linear model with very little variation and each of the three ramping cycles showed a high level of agreement when compared to the other two. However the variation between test samples was significantly large enough to limit the interpretation of the testing result to general trends. For ecample the degradation of the longitudinal modulus for the two uniaxial samples at 2000 micro-strain (Figure 4.18) should be fairly close, but were 1.69% and 4.70%. While these values show a general trend od degradation, a prediction of the degree of degradation would not be possible so to the uncertainty associated with the scatter between the two samples. Therefore many more test samples would have to be tested at each temperature/strain condition in order to develop an accurate predictive model.

These large variations can be attributed to the hand lay-up fabrication method used to create the samples. Hand lay-up fabrication requires a high degree of skill and knowledge as well as good quality control to create quality parts (Bank, 2006). The samples used did show some voids and had uneven sections as mentioned in chapter 3.

CHAPTER 5

CONCLUSIONS AND RECOMMENDATIONS

5.1. Conclusions

An analytical and experimental study was conducted on GFRP laminates, in particular the laminates that typically are incorporated in the face sheets of FRP sandwich panels. The analytical study detailed the composite theory used to design a GFRP sandwich bridge desk panel as well as equivalent simplified procedures. The experimental study involved observing the GFRP behavior up to failure as well as observing the effects of low-temperature and low-temperature coupled with various tensile strain levels on the longitudinal modulus of elasticity. Based on the outcome of the analytical and experimental investigations documented within this thesis, the following conclusions were obtained:

- Both uniaxial and biaxial GFRP laminates showed nearly linear elastic behavior up to failure at room temperature.
- Low-temperature played a significant role in the longitudinal modulus of elasticity of GFRP laminates.
- Both uniaxail and biaxial samples showed a steady nearly linear increase in the longitudinal modulus of elasticity as the sample temperature was decreased down to -31°F, when the strain level was below 1000 micro-strain. The rate of increase however was not consistent between the uniaxial nor the biaxial samples.

- Repeated load cycles of 2000 and 3000 micro-strain at room temperature for biaxial samples caused a degradation of the longitudinal modulus up to 6%, but showed no noticeable degradation of the modulus for uniaxial samples.
- Low-temperatures down to -31°F, coupled with strain levels of 2000 and 3000 micro-strain showed noticeably larger degradation of the longitudinal modulus than the room temperature control tests subjected to the same strain levels. A total degradation of 15% was observed in the low-temperature biaxial samples while the low-temperature uniaxial samples showed 4% degradation.
- The uniaxial test samples showed less degradation of the modulus of elasticity than the biaxial samples throughout all phases of testing, but the biaxial samples showed a greater increase in stiffness as the temperature was reduced. This can be attributed to the fact that the overall laminate behavior of the biaxial samples was affected by the resin properties to a larger extent than the uniaxial samples. Due to the polymer mature of the resin it is more sensitive to low-temperature effects than the E-glass reinforcement.
- Although the theoretical analysis and design of FRP composite materials can be overly complex, in general there are drastically simplified modeling procedures that can be applied to the specific cases generally seen during a design.

5.2. Recommendations

Although the results obtained during the experimental study documented within this thesis obtained some generalized trends, a number of other questions were

introduced. Further research is needed in order to fully understand the responses of FRP materials under naturally harsh environments, this includes:

- More samples at each temperature/strain level need to be tested in order to refine the prediction of GFRP materials to low-temperature and low-temperature coupled with various strain levels.
- The strain levels tested were 1000 to 3000 micro-strain which correspond to roughly 6% to 18% of the ultimate strain level, therefore strain levels even greater than these need to be tested so that a true response throughout the strain envelope can be determined.
- Although 1000 micro-strain corresponds to the service level strain within a GFRP sandwich deck panel fabricated by KSCI, maximum strains in other panels and applications need to be determined.
- Low-temperature and low-temperature coupled with various strain levels need to be fatigue tested so that the durability of the samples can be established and to determine if the degradation of the modulus continues with repeated cycles or approaches a type of equilibrium.

LIST OF REFERENCES

LIST OF REFERENCES

Altenbach, H., et al. (2004). "Mechanics of Composite Structural Elements." New York, Springer-Verlag, 486 pp.

Birman, V., Bert, C. (2002). "On the Choice of Shear Correction Factor in Sandwich Structures." J. of Sandwich Structures and Materials, 4(1), 83-95.

Chen, A., Davalos, J. F. (2004). "Behavior of Honeycomb FRP Sandwich Sinusoidal Core Panels with Skin Effect." *Proc. of 9th ASCE Aerospace Division International Conference on Engineering, Construction, and Operations in Challenging Environments*, Houston, TX, 625-632.

Cheng, L., et al. (2005). "Assessment of Steel-Free Reinforced Polymer-Composite Modular Bridge System." J. Struct. Engrg., 131(3), 498-506.

Cusson, R., Xi Y. (2002). "The Behavior of Fiber-Reinforced Polymer Reinforcement in Low Temperature Environmental Climates." *Report No. CDOT-DTD-R-2003-4*, Colorado Department of Transportation, Denver, Colorado.

Davalos, J. F., et al. (2001). "Modeling and Characterization of Fiber-Reinforced Plastic Honeycomb Sandwich Panels for Highway Bridge Applications." Composite Structures, 52(3-4), 441-452.

Dutta, P. K., Hui, D. (1996). "Low-Temperature and Freeze-Thaw Durability of Thick Composites." Composites: Part B, 27(3-4), 371-379.

Dutta, P. K., Lampo, R. G. (1993). "Behavior of Fiber-Reinforced Plastics as Construction Materials in Extreme Environments." *Proc. of the Third International Offshore and Polar Engineering Conference*, Singapore, 339-344.

Dutta, P. K., Porter, M. L. (2004). "Effects of Cold Regions Climate on the Tensile Strengths of Aged Composite Reinforced Bars." *Proc. of the Fourteenth international Offshore and Polar Engineering Conference*, Toulon, France, 263-268.

Helbling, C., et al. (2005). "Issues of Variability and Durability Under Synergistic Exposure Conditions Related to Advanced Polymer Composites in the Civil Infrastructure." Composites: Part A, 37(8), 1102-1110.

Johansen, G. E., et al. (1996). "Design and construction of two FRP pedestrian bridges in Haleakala National Park, Maui, Hawaii." *Proc., Advanced Composites Materials in Bridges and Structures*, Canadian Society for Civil Engineering, Montreal, 975–982.

Ma, Z., Choppali, U., Li, L. (2007). "Cycling Tests of a Fibre-Reinforced Polymer Honeycomb Sandwich Deck Panel at Very Cold Temperatures." Int. J. Materials and Product Technology, 28(½)

Plunkett, J., (2006). Personal Communication

Reising, M. W., et al. (2004). "Close Look at Construction Issues and Performance of Four Fiber-Reinforced Polymer Composite Bridge Decks." J. Compo. For Constr., 8(1), 33-42.

Reising, R. M., et al. (2004). "Performance Comparison of Four Fiber-Reinforced Polymer Deck Panels." J. Compos. for Constr., 8(3), 265-274.

Rightman, J., et al. (2004). "Development of an Efficent Connector System for Fiber Reinforced Polymer Bridge Decks to Steel Girder." J. Compos. for Constr., 8(4), 279-288.

Rivera, J., Karbhari, V. M. (2001). "Characterization of Sub-Zero Response of Vinylester FRP in Civil Infrastructure Renewal." *Proc. of the Eleventh International Offshore and Polar Engineering Conference*, Stavanger, Norway, 124-130.

Shao, Y., Darchis, F. (2007). "Low Temperature Response of Pultruded Composites at Saturation." Int. J. Materials and Product Technology, 28(1-2),46-65.

Sorathia, U., et al. (2001). Chapter 9: Effects of Fire. In Gap Analysis for Durability of Fibre Reinforced Polymer Composites in Civil Infrastructure. American Society of Civil Engineers, pp. 100-121.

Wang, C. M. (1995). "Timoshenko Beam-Bending Solutions in Terms of Euler-Bernoulli Solutions." J. Engrg. Mech., 121(6), 763-765.

Williams, B. K., (2004). "Fire Performance of FRP-Strengthened Reinforced Concrete Flexural Members," PhD thesis, Department of Civil Engineering, Queen's University, Kingston, Ontario, Canada, 389 pp.

Zenkert, D. (1995). "An Intoduction to Sandwich Construction." London, Chameleon Press LTD., 277 pp.

Zhou, A., et al. (2005). "Laboratory and Field Performance of Cellular Fiber-Reinforced Polymer Composite Bridge Deck Systems." J. Compos. for Constr., 9(5), 458-467.

APPENDICES

Appendix 2.1

Fiber Volume Fraction and Elastic Lamina Properties

2.1.1 - E-Glass/Polyester – Unidirectional (m1810)

Engineering Constants (E_L, E_T, ν_{LT},G_{LT})

$E_f = 10.5\times10^6$ psi

$G_f = 4.38\times10^6$ psi

$\nu_f = 0.20$

$E_m = 0.522\times10^6$ psi

$G_m = 0.196\times10^6$ psi

$\nu_m = 0.33$

$\eta_L = 1$ (Fibers Longer than 10 mm)

$\eta_0 = 1$ (Unidirectional Fibers)

Fiber volume fraction (V_f)

$$\omega_f = \left(0.75\ lb - fibers\right) \Big/ \left(1.5\ lb - product\right) = .5$$

$$\rho_f = 0.09176\ \ lb/in^3$$

$$\omega_m = \left(0.75\ lb - resin\right) \Big/ \left(1.5\ lb - product\right) = .5$$

$$\rho_m = 0.04516\ \ lb/in^3$$

$$V_f = \frac{\frac{\omega_f}{\rho_f}}{\frac{\omega_f}{\rho_f} + \frac{\omega_m}{\rho_m}} = \frac{\frac{0.5}{0.09176}}{\frac{0.5}{0.09176} + \frac{0.5}{0.04516}} = 0.330$$

Effective Longitudinal Modulus

$$E_L = \eta_L \cdot \eta_0 \cdot E_f \cdot V_f + E_m\left(1 - V_f\right)$$
$$= (1)\cdot(1)\cdot\left(10.5\times10^6 \text{ psi}\right)\cdot(0.330) + \left(0.522\times10^6 \text{ psi}\right)\cdot\left(1-(0.330)\right)$$
$$= 3.815\times10^6 \text{ psi}$$

Effective Transverse Modulus

$$\frac{1}{E_T} = \frac{\left(1-V_f\right)}{E_m} + \frac{V_f}{E_f} = \frac{\left(1-(0.330)\right)}{\left(0.522\times10^6 \text{ psi}\right)} + \frac{(0.330)}{\left(10.5\times10^6 \text{ psi}\right)}$$
$$= \frac{1}{\left(0.760\times10^6 \text{ psi}\right)} \qquad \therefore E_T = 0.760\times10^6 \text{ psi}$$

Effective Major and Minor Poisson's Ratio

$$\nu_{LT} = \left(\nu_f \cdot V_f + \nu_m \cdot \left(1 - V_f\right)\right) = \left((0.20)\cdot(0.330) + (0.33)\cdot\left(1-(0.330)\right)\right) = 0.287$$
$$\nu_{TL} = \nu_{LT}\cdot\frac{E_T}{E_L} = (0.2871)\cdot\frac{\left(0.760\times10^6 \text{ psi}\right)}{\left(3.815\times10^6 \text{ psi}\right)} = 0.057$$

Effective In-Plane Shear Modulus (Simplified)

$$\frac{1}{G_{LT}^S} = \frac{\left(1-V_f\right)}{G_m} + \frac{V_f}{G_f} = \frac{\left(1-(0.330)\right)}{\left(0.196\times10^6 \text{ psi}\right)} + \frac{(0.330)}{\left(4.38\times10^6 \text{ psi}\right)}$$
$$= \frac{1}{\left(0.286\times10^6 \text{ psi}\right)} \qquad \therefore G_{LT}^S = 0.286\times10^6 \text{ psi}$$

Effective In-Plane Shear Modulus (Improved)

$$G_{LT}^{I} = G_m \cdot \left(\frac{G_f \cdot (1+V_f) + G_m \cdot (1-V_f)}{G_f \cdot (1-V_f) + G_m \cdot (1+V_f)} \right) = (0.196\times10^6 \text{ psi})$$

$$\cdot \left(\frac{(4.38\times10^6 \text{ psi}) \cdot (1+(0.330)) + (0.196\times10^6 \text{ psi}) \cdot (1-(0.330))}{(4.38\times10^6 \text{ psi}) \cdot (1-(0.330)) + (0.196\times10^6 \text{ psi}) \cdot (1+(0.330))} \right)$$

$$= 0.365\times10^6 \text{ psi} \quad G_{LT}^{I} \neq G_{LT}^{S} \quad \therefore G_{LT} = G_{LT}^{I} = 0.365\times10^6 \text{ psi}$$

2.1.2 - E-Glass/Polyester – Bidirectional (cm3205)

Engineering Constants (E_L, E_T, ν_{LT},G_{LT})

$E_f = 10.5\times10^6$ psi

$G_f = 4.38\times10^6$ psi

$\nu_f = 0.20$

$E_m = 0.522\times10^6$ psi

$G_m = 0.196\times10^6$ psi

$\nu_m = 0.33$

$\eta_L = 1$ (Fibers Longer than 10 mm)

$\eta_0 = 1$ (Unidirectional Fibers)

Fiber volume fraction (V_f)

$$\omega_f = (1\ lb - fibers) \Big/ (1.75\ lb - product) = 0.5714$$

$$\rho_f = 0.09176\ \ lb/in^3$$

$$\omega_m = (0.75\ lb - fiber) \Big/ (1.75\ lb - product) = 0.4286$$

$$\rho_m = 0.04516\ \ lb/in^3$$

$$V_f = \frac{\frac{\omega_f}{\rho_f}}{\frac{\omega_f}{\rho_f} + \frac{\omega_m}{\rho_m}} = \frac{\frac{0.5714}{0.09176}}{\frac{0.5714}{0.09176} + \frac{0.4286}{0.04516}} = 0.396$$

Effective Longitudinal Modulus (1/2 Layer)

$$E_L = \eta_L \cdot \eta_0 \cdot E_f \cdot V_f + E_m\left(1 - V_f\right)$$
$$= (1)\cdot(1)\cdot\left(10.5\times10^6 \text{ psi}\right)\cdot(0.396) + \left(0.522\times10^6 \text{ psi}\right)\cdot\left(1-(0.396)\right)$$
$$= 4.473\times10^6 \text{ psi}$$

Alternate Effective Longitudinal and Transverse Modulus(1 layer)

$$E_L = \eta_L \cdot \eta_0 \cdot E_f \cdot V_f + E_m\left(1 - V_f\right)$$
$$= (1)\cdot(0.5)\cdot\left(10.5\times10^6 \text{ psi}\right)\cdot(0.396) + \left(0.522\times10^6 \text{ psi}\right)\cdot\left(1-(0.396)\right)$$
$$= 2.394\times10^6 \text{ psi}$$
$$E_L = E_T = 2.394\times10^6 \text{ psi}$$

Effective Transverse Modulus (1/2 Layer)

$$\frac{1}{E_T} = \frac{\left(1-V_f\right)}{E_m} + \frac{V_f}{E_f} = \frac{\left(1-(0.396)\right)}{\left(0.522\times10^6 \text{ psi}\right)} + \frac{(0.396)}{\left(10.5\times10^6 \text{ psi}\right)}$$
$$= \frac{1}{\left(0.837\times10^6 \text{ psi}\right)} \qquad \therefore E_T = 0.837\times10^6 \text{ psi}$$

Effective Major and Minor Poisson's Ratio (1/2 Layer)

$$\nu_{LT} = \left(\nu_f \cdot V_f + \nu_m \cdot \left(1 - V_f\right)\right) = \left((0.20)\cdot(0.396) + (0.33)\cdot\left(1-(0.396)\right)\right) = 0.279$$
$$\nu_{TL} = \nu_{LT} \cdot \frac{E_T}{E_L} = (0.279)\cdot\frac{\left(0.837\times10^6 \text{ psi}\right)}{\left(4.473\times10^6 \text{ psi}\right)} = 0.052$$

Effective In-Plane Shear Modulus (Simplified) (1/2 Layer)

$$\frac{1}{G_{LT}^{S}} = \frac{\left(1-V_f\right)}{G_m} + \frac{V_f}{G_f} = \frac{\left(1-\left(0.396\right)\right)}{\left(0.196\times10^{6}\ \text{psi}\right)} + \frac{\left(0.396\right)}{\left(4.38\times10^{6}\ \text{psi}\right)}$$

$$= \frac{1}{\left(0.315\times10^{6}\ \ \text{psi}\right)} \qquad \therefore G_{LT}^{S} = 0.315\times10^{6}\ \ \text{psi}$$

Effective In-Plane Shear Modulus (Improved) (1/2 Layer)

$$G_{LT}^{I} = G_m \cdot \left(\frac{G_f \cdot \left(1+V_f\right) + G_m \cdot \left(1-V_f\right)}{G_f \cdot \left(1-V_f\right) + G_m \cdot \left(1+V_f\right)} \right) = \left(0.196\times10^{6}\ \text{psi}\right)$$

$$\cdot \left(\frac{\left(4.38\times10^{6}\ \text{psi}\right)\cdot\left(1+\left(0.396\right)\right) + \left(0.196\times10^{6}\ \text{psi}\right)\cdot\left(1-\left(0.396\right)\right)}{\left(4.38\times10^{6}\ \text{psi}\right)\cdot\left(1-\left(0.396\right)\right) + \left(0.196\times10^{6}\ \text{psi}\right)\cdot\left(1+\left(0.396\right)\right)} \right)$$

$$= 0.418\times10^{6}\ \ \text{psi} \quad G_{LT}^{I} \neq G_{LT}^{S} \qquad \therefore G_{LT} = G_{LT}^{I} = 0.418\times10^{6}\ \ \text{psi}$$

2.1.3 - E-Glass/Polyester – CSM

Engineering Constants (E_L, E_T, ν_{LT},G_{LT})

$E_f = 10.5\times10^{6}$ psi

$G_f = 4.38\times10^{6}$ psi

$\nu_f = 0.20$

$E_m = 0.522\times10^{6}$ psi

$G_m = 0.196\times10^{6}$ psi

$\nu_m = 0.33$

$\eta_L = 1$ (Fibers Longer than 10 mm)

$\eta_0 = 0.375$ (Unidirectional Fibers)

Fiber volume fraction (V_f)

$$\omega_f = \left(0.75\ lb-fiber\right) \Big/ \left(1.75\ lb-product\right) = 0.4286$$

$$\rho_f = 0.09176\ \ lb/in^3$$

$$\omega_m = \left(1\ lb-fiber\right) \Big/ \left(1.75\ lb-product\right) = 0.5714$$

$$\rho_m = 0.04516\ \ lb/in^3$$

$$V_f = \frac{\frac{\omega_f}{\rho_f}}{\frac{\omega_f}{\rho_f}+\frac{\omega_m}{\rho_m}} = \frac{\frac{0.4286}{0.09176}}{\frac{0.4286}{0.09176}+\frac{0.5714}{0.04516}} = 0.270$$

Effective Longitudinal Modulus

$$E_L = \eta_L \cdot \eta_0 \cdot E_f \cdot V_f + E_m\left(1-V_f\right)$$
$$= (1)\cdot\left(0.375\right)\cdot\left(10.5\times10^6\ \text{psi}\right)\cdot\left(0.270\right)+\left(0.522\times10^6\ \text{psi}\right)\cdot\left(1-\left(0.270\right)\right)$$
$$= 1.444\times10^6\ \text{psi}$$

Effective Transverse Modulus

Isotropic Material $\therefore\ \ E_T = E_L = 1.444\times10^6$ psi

Effective Major and Minor Poisson's Ratio

$$\nu_{LT} = \left(\nu_f \cdot V_f + \nu_m \cdot \left(1-V_f\right)\right) = \left(\left(0.20\right)\cdot\left(0.270\right)+\left(0.33\right)\cdot\left(1-\left(0.270\right)\right)\right) = 0.295$$

$$\nu_{TL} = \nu_{LT}\cdot\frac{E_T}{E_L} = \left(0.295\right)\cdot\frac{\left(1.444\times10^6\ \text{psi}\right)}{\left(1.444\times10^6\ \text{psi}\right)} = 0.295$$

Effective In-Plane Shear Modulus (Simplified)

$$\frac{1}{G_{LT}^{S}} = \frac{\left(1-V_f\right)}{G_m} + \frac{V_f}{G_f} = \frac{\left(1-\left(0.270\right)\right)}{\left(0.196\times10^{6}\ \text{psi}\right)} + \frac{\left(0.270\right)}{\left(4.38\times10^{6}\ \text{psi}\right)}$$

$$= \frac{1}{\left(0.264\times10^{6}\ \ \text{psi}\right)} \qquad \therefore G_{LT}^{S} = 0.264\times10^{6}\ \ \text{psi}$$

Effective In-Plane Shear Modulus (Improved)

$$G_{LT}^{I} = G_m \cdot \left(\frac{G_f \cdot \left(1+V_f\right) + G_m \cdot \left(1-V_f\right)}{G_f \cdot \left(1-V_f\right) + G_m \cdot \left(1+V_f\right)} \right) = \left(0.196\times10^{6}\ \text{psi}\right)$$

$$\cdot \left(\frac{\left(4.38\times10^{6}\ \text{psi}\right)\cdot\left(1+\left(0.270\right)\right) + \left(0.196\times10^{6}\ \text{psi}\right)\cdot\left(1-\left(0.270\right)\right)}{\left(4.38\times10^{6}\ \text{psi}\right)\cdot\left(1-\left(0.270\right)\right) + \left(0.196\times10^{6}\ \text{psi}\right)\cdot\left(1+\left(0.270\right)\right)} \right)$$

$$= 0.324\times10^{6}\ \ \text{psi} \qquad G_{LT}^{I} \neq G_{LT}^{S} \qquad \therefore G_{LT} = G_{LT}^{I} = 0.324\times10^{6}\ \ \text{psi}$$

Appendix 2.2

Elastic Lamina Behavior: Stiffness Matrixes

2.2.1 – (E-Glass/Polyester) Bidirectional $(cm3205)_{0^\circ}$

$$E_L = 4.473\times10^6 \text{ psi}$$
$$E_T = 0.837\times10^6 \text{ psi}$$
$$G_{LT} = 0.418\times10^6 \text{ psi}$$
$$\nu_{LT} = 0.279$$
$$\nu_{TL} = 0.052$$

Lamina Reduced Stiffness Coefficients Q'_{ij}

$$Q'_{11} = \frac{E'_1}{\left(1-\nu'_{12}\cdot\nu'_{21}\right)} = \frac{E_L}{\left(1-\nu_{LT}\cdot\nu_{TL}\right)} = \frac{\left(4.473\times10^6 \text{ psi}\right)}{\left(1-\left(0.279\right)\cdot\left(0.052\right)\right)} = 4.539\times10^6 \text{ psi}$$

$$Q'_{22} = \frac{E'_2}{\left(1-\nu'_{12}\cdot\nu'_{21}\right)} = \frac{E_T}{\left(1-\nu_{LT}\cdot\nu_{TL}\right)} = \frac{\left(0.837\times10^6 \text{ psi}\right)}{\left(1-\left(0.279\right)\cdot\left(0.052\right)\right)} = 0.849\times10^6 \text{ psi}$$

$$Q'_{66} = G'_{12} = E'_6 = G_{LT} = 0.418\times10^6 \text{ psi}$$

$$Q'_{12} = \frac{E'_2\cdot\nu'_{12}}{\left(1-\nu'_{12}\cdot\nu'_{21}\right)} = \frac{E_T\cdot\nu_{LT}}{\left(1-\nu_{LT}\cdot\nu_{TL}\right)} = \frac{\left(0.837\times10^6 \text{ psi}\right)\cdot\left(0.279\right)}{\left(1-\left(0.279\right)\cdot\left(0.052\right)\right)} = 0.237\times10^6 \text{ psi}$$

Lamina Transformed Stiffness Coefficients Q_{ij}

$$Q_{11} = Q'_{11} = 4.539\times10^6 \text{ psi}$$
$$Q_{22} = Q'_{22} = 0.849\times10^6 \text{ psi}$$
$$Q_{66} = Q'_{66} = 0.418\times10^6 \text{ psi}$$
$$Q_{12} = Q'_{12} = 0.237\times10^6 \text{ psi}$$

* Due to lamina coordinates being the same as the global coordinates.

2.2.2 – (E-Glass/Polyester) Bidirectional (cm3205)$_{90°}$

$E_L = 4.473\times10^6$ psi

$E_T = 0.837\times10^6$ psi

$G_{LT} = 0.418\times10^6$ psi

$\nu_{LT} = 0.279$

$\nu_{TL} = 0.052$

Lamina Reduced Stiffness Coefficients Q'$_{ij}$

$Q'_{11} = 4.539\times10^6$ psi

$Q'_{22} = 0.849\times10^6$ psi

$Q'_{66} = 0.418\times10^6$ psi

$Q'_{12} = 0.237\times10^6$ psi

*Due to lamina coordinates being the same in both layers.

Lamina Transformed Stiffness Coefficients Q$_{ij}$

$$\begin{bmatrix} Q_{11} \\ Q_{12} \\ Q_{16} \\ Q_{22} \\ Q_{26} \\ Q_{66} \end{bmatrix} = \begin{bmatrix} c^4 & 2\cdot c^2\cdot s^2 & s^4 & 4\cdot c^2\cdot s^2 \\ c^2\cdot s^2 & c^4+s^4 & c^2\cdot s^2 & -4\cdot c^2\cdot s^2 \\ c^3\cdot s & -c\cdot s\cdot\left(c^2-s^2\right) & -c\cdot s^3 & -2\cdot c\cdot s\cdot\left(c^2-s^2\right) \\ s^4 & 2\cdot c^2\cdot s^2 & c^4 & 4\cdot c^2\cdot s^2 \\ c\cdot s^3 & c\cdot s\cdot\left(c^2-s^2\right) & -c^3\cdot s & 2\cdot c\cdot s\cdot\left(c^2-s^2\right) \\ c^2\cdot s^2 & -2\cdot c^2\cdot s^2 & c^2\cdot s^2 & \left(c^2-s^2\right)^2 \end{bmatrix} \cdot \begin{bmatrix} Q'_{11} \\ Q'_{12} \\ Q'_{22} \\ Q'_{66} \end{bmatrix} = \begin{bmatrix} 0 & 0 & 1 & 0 \\ 0 & 1 & 0 & 0 \\ 0 & 0 & 0 & 0 \\ 1 & 0 & 0 & 0 \\ 0 & 0 & 0 & 0 \\ 0 & 0 & 0 & 1 \end{bmatrix} \cdot \begin{bmatrix} Q'_{11} \\ Q'_{12} \\ Q'_{22} \\ Q'_{66} \end{bmatrix}$$

$c = \cos(\theta) \quad s = \sin(\theta)$

$Q_{11} = Q'_{22} = 0.849\times10^6$ psi

$Q_{22} = Q'_{11} = 4.539\times10^6$ psi

$Q_{66} = Q'_{66} = 0.418\times10^6$ psi

$Q_{12} = Q'_{12} = 0.237\times10^6$ psi

2.2.3 – (E-Glass/Polyester) Unidirectional (m1810)

$E_L = 3.815\times10^6$ psi

$E_T = 0.760\times10^6$ psi

$G_{LT} = 0.365\times10^6$ psi

$\nu_{LT} = 0.287$

$\nu_{TL} = 0.057$

Lamina Reduced Stiffness Coefficients Q'ij

$$Q_{11}^{'} = \frac{E_1^{'}}{\left(1-\nu_{12}^{'}\cdot\nu_{21}^{'}\right)} = \frac{E_L}{\left(1-\nu_{LT}\cdot\nu_{TL}\right)} = \frac{\left(3.815\times10^6 \text{ psi}\right)}{\left(1-\left(0.287\right)\cdot\left(0.057\right)\right)} = 3.878\times10^6 \text{ psi}$$

$$Q_{22}^{'} = \frac{E_2^{'}}{\left(1-\nu_{12}^{'}\cdot\nu_{21}^{'}\right)} = \frac{E_T}{\left(1-\nu_{LT}\cdot\nu_{TL}\right)} = \frac{\left(0.760\times10^6 \text{ psi}\right)}{\left(1-\left(0.287\right)\cdot\left(0.057\right)\right)} = 0.773\times10^6 \text{ psi}$$

$$Q_{66}^{'} = G_{12}^{'} = E_6^{'} = G_{LT} = 0.365\times10^6 \text{ psi}$$

$$Q_{12}^{'} = \frac{E_2^{'}\cdot\nu_{12}^{'}}{\left(1-\nu_{12}^{'}\cdot\nu_{21}^{'}\right)} = \frac{E_T\cdot\nu_{LT}}{\left(1-\nu_{LT}\cdot\nu_{TL}\right)} = \frac{\left(0.760\times10^6 \text{ psi}\right)\cdot\left(0.287\right)}{\left(1-\left(0.287\right)\cdot\left(0.057\right)\right)} = 0.222\times10^6 \text{ psi}$$

Lamina Transformed Stiffness Coefficients Qij

$Q_{11} = Q_{11}^{'} = 3.878\times10^6$ psi

$Q_{22} = Q_{22}^{'} = 0.773\times10^6$ psi

$Q_{66} = Q_{66}^{'} = 0.365\times10^6$ psi

$Q_{12} = Q_{12}^{'} = 0.222\times10^6$ psi

* Due to lamina coordinates being the same as the global coordinates.

Appendix 2.3

Elastic Laminate Behavior of Individual Face Sheet

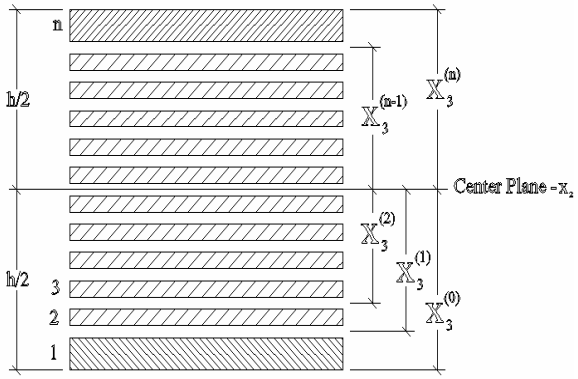

Laminate Lay-up

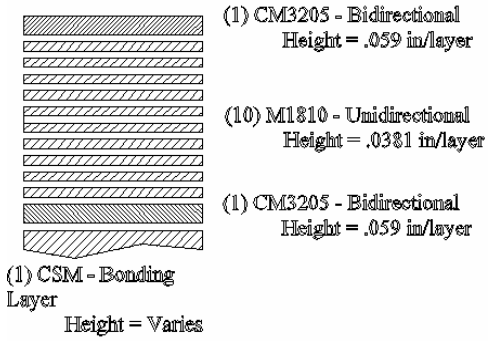

Top and Bottom Face Sheet Lay-up

2.3.1 - Lay-up Sequence and Lamina Info

$[(cm3205)_{0°}/(cm3205)_{90°}/(m1810)/(m1810)/(m1810)/(m1810)/(m1810)]_S$

$$h = 2\cdot(0.059\text{ in}) + 10\cdot(0.0381\text{ in}) = .499\text{ in}$$

E-Glass/Polyester – Bidirectional $(cm3205)_{0°}$

$$h^{(k)} = \frac{(0.059\text{ in})}{2} = 0.0295\text{ in}$$
$$Q_{11} = 4.539\times10^6\text{ psi}$$
$$Q_{22} = 0.849\times10^6\text{ psi}$$
$$Q_{66} = 0.418\times10^6\text{ psi}$$
$$Q_{12} = 0.237\times10^6\text{ psi}$$
$$Q_{16} = Q_{26} = 0\text{ psi}$$

E-Glass/Polyester – Bidirectional $(cm3205)_{90°}$

$$h^{(k)} = 0.0295\text{ in}$$
$$Q_{11} = 0.849\times10^6\text{ psi}$$
$$Q_{22} = 4.539\times10^6\text{ psi}$$
$$Q_{66} = 0.418\times10^6\text{ psi}$$
$$Q_{12} = 0.237\times10^6\text{ psi}$$
$$Q_{16} = Q_{26} = 0\text{ psi}$$

E-Glass/Polyester - Unidirectional (m1810)

$$h^{(k)} = 0.0381\text{ in}$$
$$Q_{11} = 3.878\times10^6\text{ psi}$$
$$Q_{22} = 0.773\times10^6\text{ psi}$$
$$Q_{66} = 0.365\times10^6\text{ psi}$$
$$Q_{12} = 0.222\times10^6\text{ psi}$$
$$Q_{16} = Q_{26} = 0\text{ psi}$$

*From Appendix 2.2

2.3.3 - Axial Stiffness for Top Face Laminate

$$A_{ij} = \sum_{k=1}^{n} Q_{ij}^{(k)} \cdot h^{(k)} = \sum_{k=1}^{12} Q_{ij}^{(k)} \cdot h^{(k)}$$

$$A_{11} = \sum_{k=1}^{14} Q_{11}^{(k)} \cdot h^{(k)} = 2 \cdot \left(\left(4.539 \times 10^{6} \text{ psi} \right) \cdot \left(0.0295 \text{ in} \right) \right)$$

$$+2 \cdot \left(\left(0.849 \times 10^{6} \text{ psi} \right) \cdot \left(0.0295 \text{ in} \right) \right) + 10 \cdot \left(\left(3.878 \times 10^{6} \text{ psi} \right) \cdot \left(0.0381 \text{ in} \right) \right)$$

$$= 1.796 \times 10^{6} \text{ psi} \cdot \text{in}$$

Similarly,

$$A_{11} = 1.796 \times 10^{6} \text{ psi} \cdot \text{in}$$

$$A_{22} = 0.612 \times 10^{6} \text{ psi} \cdot \text{in}$$

$$A_{66} = 0.188 \times 10^{6} \text{ psi} \cdot \text{in}$$

$$A_{12} = 0.112 \times 10^{6} \text{ psi} \cdot \text{in}$$

$$A_{16} = A_{26} = 0 \text{ psi} \cdot \text{in}$$

2.3.3 - Coupling Stiffness for Top Face Laminate

$$B_{ij} = \sum_{k=1}^{n} Q_{ij}^{(k)} \cdot \bar{x}_3^{(k)} \cdot h^{(k)} = \sum_{k=1}^{12} Q_{ij}^{(k)} \cdot \bar{x}_3^{(k)} \cdot h^{(k)}$$

$$B_{11} = \sum_{k=1}^{14} Q_{11}^{(k)} \cdot \bar{x}_3^{(k)} \cdot h^{(k)}$$

$$= \left[\left(4.539 \times 10^{6} \text{ psi} \right) \cdot \left(0.2348 \text{ in} \right) \cdot \left(0.0295 \text{ in} \right) \right]^{(cm3205)_{0^\circ}}$$

$$+ \left[\left(0.849 \times 10^{6} \text{ psi} \right) \cdot \left(0.2053 \text{ in} \right) \cdot \left(0.0295 \text{ in} \right) \right]^{(cm3205)_{90^\circ}}$$

$$+ \left[\left(3.878 \times 10^{6} \text{ psi} \right) \cdot \left(0 \text{ in} \right) \cdot \left(\left(10 \text{ Lam} \right) \cdot \left(0.0381 \text{ in} \right) \right) \right]^{(m1810)}$$

$$+ \left[\left(0.849 \times 10^{6} \text{ psi} \right) \cdot \left(-0.2053 \text{ in} \right) \cdot \left(0.0295 \text{ in} \right) \right]^{(cm3205)_{90^\circ}}$$

$$+ \left[\left(4.539 \times 10^{6} \text{ psi} \right) \cdot \left(-0.2348 \text{ in} \right) \cdot \left(0.0295 \text{ in} \right) \right]^{(cm3205)_{0^\circ}} = 0 \text{ psi} \cdot \text{in}^2$$

Similarly due to laminate lay-up symmetry,

$$B_{11} = B_{22} = B_{66} = B_{12} = B_{16} = B_{26} = 0 \text{ psi} \cdot \text{in}$$

2.3.4 - Flexural Stiffness for Top Face Laminate

$$D_{ij} = \sum_{k=1}^{n} Q_{ij}^{(k)} \cdot h^{(k)} \cdot \left(\bar{x}_3^{(k)^2} + \frac{h^{(k)^2}}{12} \right) = \sum_{k=1}^{12} Q_{ij}^{(k)} \cdot h^{(k)} \cdot \left(\bar{x}_3^{(k)^2} + \frac{h^{(k)^2}}{12} \right)$$

$$D_{11} = \sum_{k=1}^{14} Q_{11}^{(k)} \cdot h^{(k)} \cdot \left(\bar{x}_3^{(k)^2} + \frac{h^{(k)^2}}{12} \right)$$

$$= \left[\left(4.539 \times 10^6 \text{ psi}\right) \cdot \left(0.0295 \text{ in}\right) \cdot \left(\left(0.2348 \text{ in}\right)^2 + \frac{\left(0.0295 \text{ in}\right)^2}{12} \right) \right]^{(cm3205)_{0°}}$$

$$+ \left[\left(0.849 \times 10^6 \text{ psi}\right) \cdot \left(0.0295 \text{ in}\right) \cdot \left(\left(0.2053 \text{ in}\right)^2 + \frac{\left(0.0295 \text{ in}\right)^2}{12} \right) \right]^{(cm3205)_{90°}}$$

$$+ \left[\left(3.878 \times 10^6 \text{ psi}\right) \cdot \left(\left(10 \text{ Lam}\right) \cdot \left(0.0381 \text{ in}\right) \right) \cdot \left(\left(0 \text{ in}\right)^2 + \frac{\left(\left(10 \text{ Lam}\right) \cdot \left(0.0381 \text{ in}\right) \right)^2}{12} \right) \right]^{(m1810)}$$

$$+ \left[\left(0.849 \times 10^6 \text{ psi}\right) \cdot \left(0.0295 \text{ in}\right) \cdot \left(\left(-0.2053 \text{ in}\right)^2 + \frac{\left(0.0295 \text{ in}\right)^2}{12} \right) \right]^{(cm3205)_{90°}}$$

$$+ \left[\left(4.539 \times 10^6 \text{ psi}\right) \cdot \left(0.0295 \text{ in}\right) \cdot \left(\left(-0.2348 \text{ in}\right)^2 + \frac{\left(0.0295 \text{ in}\right)^2}{12} \right) \right]^{(cm3205)_{0°}}$$

$$= 0.035 \times 10^6 \text{ psi} \cdot \text{in}^3$$

Similarly,

$$D_{11} = 0.035 \times 10^6 \text{ psi} \cdot \text{in}^3$$
$$D_{22} = 0.018 \times 10^6 \text{ psi} \cdot \text{in}^3$$
$$D_{66} = 0.004 \times 10^6 \text{ psi} \cdot \text{in}^3$$
$$D_{12} = 0.002 \times 10^6 \text{ psi} \cdot \text{in}^3$$
$$D_{16} = D_{26} = 0 \text{ psi} \cdot \text{in}^3$$

2.3.5 - Constitutive Equation for Top Face Laminate

$$\begin{bmatrix} N_1 \\ N_2 \\ N_6 \\ \cdots \\ M_1 \\ M_2 \\ M_6 \end{bmatrix} = \begin{bmatrix} 1.796\times10^6 & 0.112\times10^6 & 0 & \vdots & 0 & 0 & 0 \\ 0.112\times10^6 & 0.612\times10^6 & 0 & \vdots & 0 & 0 & 0 \\ 0 & 0 & 0.188\times10^6 & \vdots & 0 & 0 & 0 \\ \cdots & \cdots & \cdots & \cdots & \cdots & \cdots & \cdots \\ 0 & 0 & 0 & \vdots & 0.035\times10^6 & 0.002\times10^6 & 0 \\ 0 & 0 & 0 & \vdots & 0.002\times10^6 & 0.018\times10^6 & 0 \\ 0 & 0 & 0 & \vdots & 0 & 0 & 0.004\times10^6 \end{bmatrix} \cdot \begin{bmatrix} \varepsilon_{a1} \\ \varepsilon_{a2} \\ \varepsilon_{a6} \\ \cdots \\ \kappa_1 \\ \kappa_2 \\ \kappa_6 \end{bmatrix}$$

Appendix 2.4

Sinusoidal Honeycomb Sandwich Behavior

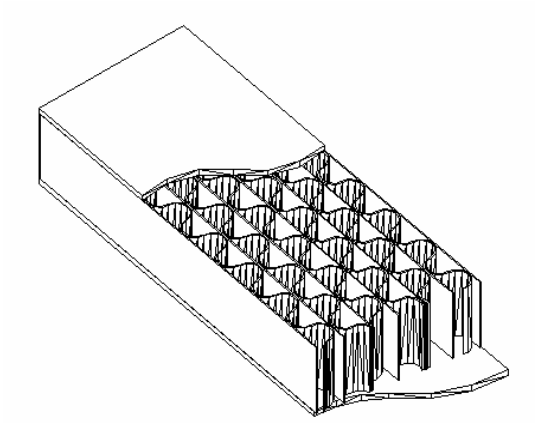

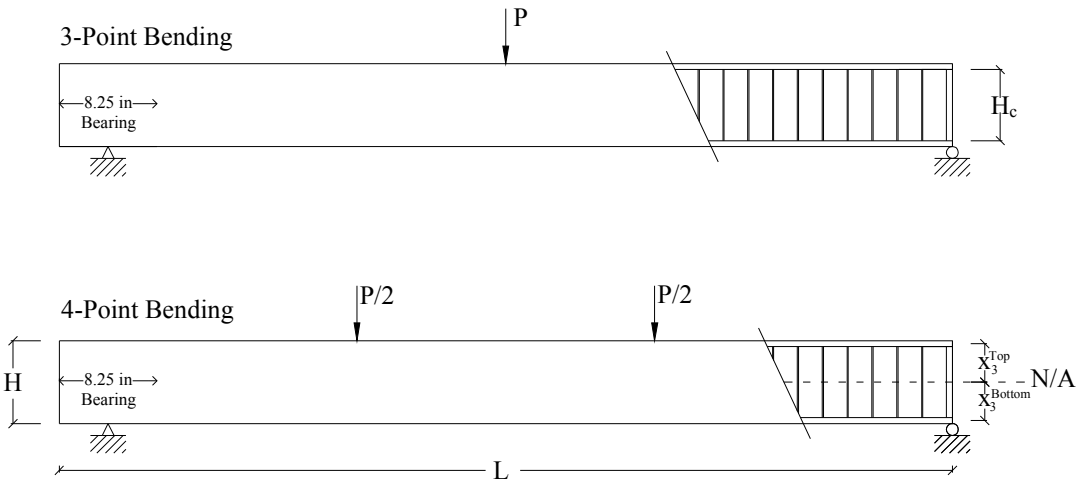

2.4.1 – Overall Sandwich Beam Properties

$L = 75.75$ in

$B = 13.4$ in

$H = 7$ in

$H_c = 6.002$ in

Neutral Axis = 3.5 in (from bottom of beam)

$X_3^{Top} = 3.2505$ in

$X_3^{Bottom} = -3.2505$ in

2.4.2 – Sinusoidal Core Properties

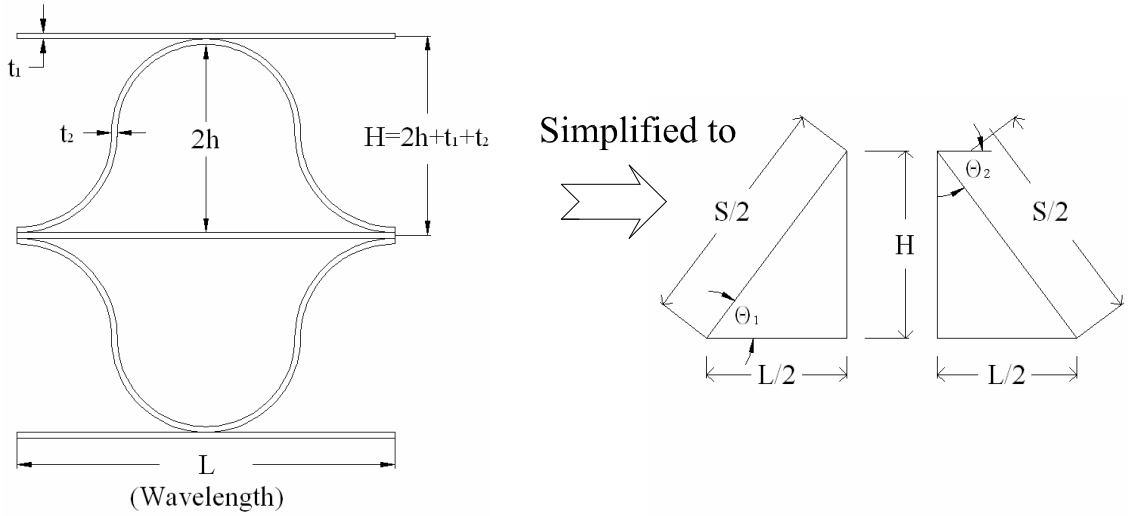

where,

$$t_1 = 0.1 \text{ in}$$
$$t_2 = 0.1 \text{ in}$$
$$h = 1 \text{ in}$$
$$L = 4 \text{ in}$$
$$\mathrm{H} = 2 \cdot h + t_1 + t_2 = 2 \cdot (1 \text{ in}) + (0.1 \text{ in}) + (0.1 \text{ in}) = 2.2 \text{ in}$$

$$\frac{S}{2} = \sqrt{\left(\left(L/2\right)^2 + \left(H\right)^2\right)} = \sqrt{\left(\left(4 \text{ in}/2\right)^2 + \left(2.2 \text{ in}\right)^2\right)} = 2.973 \text{ in}$$

$$\theta_1 = \tan^{-1}\left(\frac{(H)}{\left(L/2\right)}\right) = \tan^{-1}\left(\frac{(2.2 \text{ in})}{\left(4 \text{ in}/2\right)}\right) = 47.73° = 0.833 \text{ rad}$$

$$\theta_2 = \tan^{-1}\left(\frac{(-H)}{\left(L/2\right)}\right) = \tan^{-1}\left(\frac{(-2.2 \text{ in})}{\left(4 \text{ in}/2\right)}\right) = -47.73° = -0.833 \text{ rad}$$

$$G_{12}^{core} = 0.324 \times 10^6 \text{ psi}$$

Sandwich Core Properties

$$G_{13} = G_{12}^{core}\left(\frac{2\cdot t_1}{H} + \frac{4\cdot t_2}{H\cdot L}\cdot\frac{S}{2}\cdot\left(\cos^2\theta_1 + \cos^2\theta_2\right)\right)$$

$$= \left(0.324\times10^6\right)\left(\frac{2\cdot\left(0.1\text{ in}\right)}{\left(2.2\text{ in}\right)} + \frac{4\cdot\left(0.1\text{ in}\right)}{\left(2.2\text{ in}\right)\cdot\left(2\text{ in}\right)}\cdot\left(2.973\text{ in}\right)\cdot\left(\cos^2\left(0.833\text{ rad}\right) + \cos^2\left(-0.833\text{ rad}\right)\right)\right)$$

$$= 0.037\times10^6\text{ psi}$$

$$G_{23} = G_{12}^{core}\left(\frac{4\cdot t_2}{H\cdot L}\cdot\frac{S}{2}\cdot\left(\sin^2\theta_1 + \sin^2\theta_2\right)\right)$$

$$= \left(0.324\times10^6\text{ psi}\right)\left(\frac{4\cdot\left(0.1\text{ in}\right)}{\left(2.2\text{ in}\right)\cdot\left(4\text{ in}\right)}\cdot\left(2.973\text{ in}\right)\cdot\left(\sin^2\left(0.833\text{ rad}\right) + \sin^2\left(-0.833\text{ rad}\right)\right)\right)$$

$$= 0.048\times10^6\text{ psi}$$

Transverse Shear Stiffness Coefficients and A^s Matrix

$$C_{44} = C'_{44} = E_{44} = G_{23} = 0.048\times10^6\text{ psi}$$

$$C_{55} = C'_{55} = E_{55} = G_{13} = 0.037\times10^6\text{ psi}$$

*No rotation is needed because core geometry is already aligned to global coordinates.

$$A_{ij}^s = \sum_{k=1}^{n} C_{ij}^{(k)}\cdot\left(x_3^{(k)} - x_3^{(k-1)}\right) = \sum_{k=1}^{n} C_{ij}^{(k)}\cdot h^{(k)} \qquad i,j = 4,5$$

$$A_{44}^s = C_{44}\cdot H_C = \left(0.048\times10^6\text{ psi}\right)\cdot\left(6.002\text{ in}\right) = 0.288\times10^6\text{ psi}\cdot\text{in}$$

$$A_{55}^s = C_{55}\cdot H_C = \left(0.037\times10^6\text{ psi}\right)\cdot\left(6.002\text{ in}\right) = 0.222\times10^6\text{ psi}\cdot\text{in}$$

$$A_{45}^s = C_{45}\cdot H_C = \left(0\right)\cdot\left(6.002\text{ in}\right) = 0\text{ psi}$$

$$\begin{bmatrix} Q_4^s \\ Q_5^s \end{bmatrix} = \begin{bmatrix} A_{44}^s & A_{45}^s \\ A_{45}^s & A_{55}^s \end{bmatrix}\cdot\begin{bmatrix} \gamma_4^s \\ \gamma_5^s \end{bmatrix} = \begin{bmatrix} 0.288\times10^6 & 0 \\ 0 & 0.222\times10^6 \end{bmatrix}\cdot\begin{bmatrix} \gamma_4^s \\ \gamma_5^s \end{bmatrix}$$

2.4.3 – Equivalent Face Sheet Properties

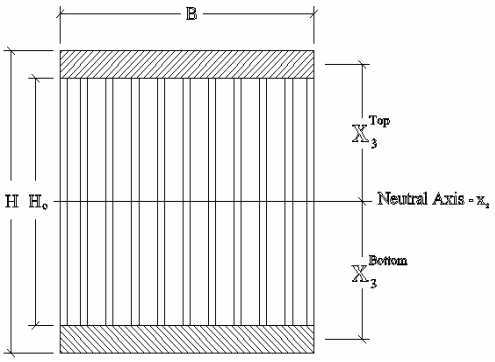

Sandwich Cross-section

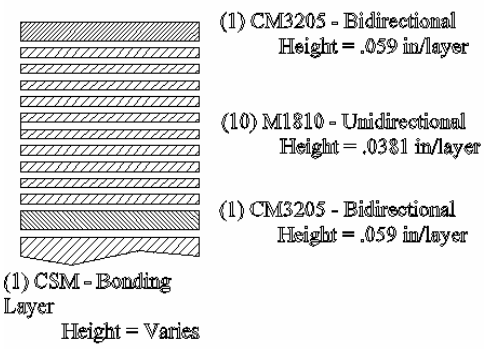

Top and Bottom Face Sheet Lay-up

2.4.3.1 – First Approach - Treat Sandwich Panel as One Laminate

E-Glass/Polyester – Bidirectional $(cm3205)_{0°}$

$$h^{(k)} = \frac{(0.059 \text{ in})}{2} = 0.0295 \text{ in}$$
$$Q_{11} = 4.539\times10^6 \text{ psi}$$
$$Q_{22} = 0.849\times10^6 \text{ psi}$$
$$Q_{66} = 0.418\times10^6 \text{ psi}$$
$$Q_{12} = 0.237\times10^6 \text{ psi}$$
$$Q_{16} = Q_{26} = 0 \text{ psi}$$

E-Glass/Polyester – Bidirectional $(cm3205)_{90°}$

$$h^{(k)} = 0.0295 \text{ in}$$
$$Q_{11} = 0.849\times10^6 \text{ psi}$$
$$Q_{22} = 4.539\times10^6 \text{ psi}$$
$$Q_{66} = 0.418\times10^6 \text{ psi}$$
$$Q_{12} = 0.237\times10^6 \text{ psi}$$
$$Q_{16} = Q_{26} = 0 \text{ psi}$$

E-Glass/Polyester - Unidirectional (m1810)

$$h^{(k)} = 0.0381 \text{ in}$$
$$Q_{11} = 3.878\times10^6 \text{ psi}$$
$$Q_{22} = 0.773\times10^6 \text{ psi}$$
$$Q_{66} = 0.365\times10^6 \text{ psi}$$
$$Q_{12} = 0.222\times10^6 \text{ psi}$$
$$Q_{16} = Q_{26} = 0 \text{ psi}$$

Axial Stiffness for Sandwich

$$A_{ij} = \sum_{k=1}^{n} Q_{ij}^{(k)} \cdot h^{(k)} = \sum_{k=1}^{12} Q_{ij}^{(k)} \cdot h^{(k)}$$

$$A_{11} = \sum_{k=1}^{28} Q_{11}^{(k)} \cdot h^{(k)} = 4 \cdot \left(\left(4.539\times10^6 \text{ psi}\right) \cdot \left(0.0295 \text{ in}\right) \right)$$

$$+4 \cdot \left(\left(0.849\times10^6 \text{ psi}\right) \cdot \left(0.0295 \text{ in}\right) \right) + 20 \cdot \left(\left(3.878\times10^6 \text{ psi}\right) \cdot \left(0.0381 \text{ in}\right) \right)$$

$$= 3.59\times10^6 \text{ psi} \cdot \text{in}$$

Similarly,

$$A_{11} = 3.591\times10^{6}\ \text{psi}\cdot\text{in}$$
$$A_{22} = 1.225\times10^{6}\ \text{psi}\cdot\text{in}$$
$$A_{66} = 0.376\times10^{6}\ \text{psi}\cdot\text{in}$$
$$A_{12} = 0.225\times10^{6}\ \text{psi}\cdot\text{in}$$
$$A_{16} = A_{26} = 0\ \text{psi}\cdot\text{in}$$

Coupling Stiffness for Sandwich

$$B_{ij} = \sum_{k=1}^{n} Q_{ij}^{(k)} \cdot \bar{x}_3^{(k)} \cdot h^{(k)} = \sum_{k=1}^{12} Q_{ij}^{(k)} \cdot \bar{x}_3^{(k)} \cdot h^{(k)}$$

$$B_{11} = \sum_{k=1}^{28} Q_{11}^{(k)} \cdot \bar{x}_3^{(k)} \cdot h^{(k)}$$

$$= \left[\left(4.539\times10^{6}\ \text{psi}\right)\cdot\left(3.485\ \text{in}\right)\cdot\left(0.0295\ \text{in}\right)\right]^{(cm3205)_{0^\circ}}$$
$$+\left[\left(0.849\times10^{6}\ \text{psi}\right)\cdot\left(3.456\ \text{in}\right)\cdot\left(0.0295\ \text{in}\right)\right]^{(cm3205)_{90^\circ}}$$
$$+\left[\left(3.878\times10^{6}\ \text{psi}\right)\cdot\left(3.251\ \text{in}\right)\cdot\left(\left(10\ \text{Lam}\right)\cdot\left(0.0381\ \text{in}\right)\right)\right]^{(m1810)}$$
$$+\left[\left(0.849\times10^{6}\ \text{psi}\right)\cdot\left(3.045\ \text{in}\right)\cdot\left(0.0295\ \text{in}\right)\right]^{(cm3205)_{90^\circ}}$$
$$+\left[\left(4.539\times10^{6}\ \text{psi}\right)\cdot\left(3.016\ \text{in}\right)\cdot\left(0.0295\ \text{in}\right)\right]^{(cm3205)_{0^\circ}}$$
$$+\left[\left(4.539\times10^{6}\ \text{psi}\right)\cdot\left(-3.016\ \text{in}\right)\cdot\left(0.0295\ \text{in}\right)\right]^{(cm3205)_{0^\circ}}$$
$$+\left[\left(0.849\times10^{6}\ \text{psi}\right)\cdot\left(-3.045\ \text{in}\right)\cdot\left(0.0295\ \text{in}\right)\right]^{(cm3205)_{90^\circ}}$$
$$+\left[\left(3.878\times10^{6}\ \text{psi}\right)\cdot\left(-3.251\ \text{in}\right)\cdot\left(\left(10\ \text{Lam}\right)\cdot\left(0.0381\ \text{in}\right)\right)\right]^{(m1810)}$$
$$+\left[\left(0.849\times10^{6}\ \text{psi}\right)\cdot\left(-3.456\ \text{in}\right)\cdot\left(0.0295\ \text{in}\right)\right]^{(cm3205)_{90^\circ}}$$
$$+\left[\left(4.539\times10^{6}\ \text{psi}\right)\cdot\left(-3.485\ \text{in}\right)\cdot\left(0.0295\ \text{in}\right)\right]^{(cm3205)_{0^\circ}} = 0\ \text{psi}\cdot\text{in}^2$$

Similarly due to laminate lay-up symmetry,

$$B_{11} = B_{22} = B_{66} = B_{12} = B_{16} = B_{26} = 0\ \text{psi}\cdot\text{in}^2$$

Flexural Stiffness for Sandwich

$$D_{ij} = \sum_{k=1}^{n} Q_{ij}^{(k)} \cdot h^{(k)} \cdot \left(\overline{x_3}^{(k)^2} + \frac{h^{(k)^2}}{12} \right) = \sum_{k=1}^{12} Q_{ij}^{(k)} \cdot h^{(k)} \cdot \left(\overline{x_3}^{(k)^2} + \frac{h^{(k)^2}}{12} \right)$$

$$D_{11} = \sum_{k=1}^{28} Q_{11}^{(k)} \cdot h^{(k)} \cdot \left(\overline{x_3}^{(k)^2} + \frac{h^{(k)^2}}{12} \right)$$

$$= \left[\left(4.539 \times 10^6 \text{ psi}\right) \cdot \left(0.0295 \text{ in}\right) \cdot \left(\left(3.485 \text{ in}\right)^2 + \frac{\left(0.0295 \text{ in}\right)^2}{12} \right) \right]^{(cm3205)_{0°}}$$

$$+ \left[\left(0.849 \times 10^6 \text{ psi}\right) \cdot \left(0.0295 \text{ in}\right) \cdot \left(\left(3.456 \text{ in}\right)^2 + \frac{\left(0.0295 \text{ in}\right)^2}{12} \right) \right]^{(cm3205)_{90°}}$$

$$+ \left[3.878 \left(3.829 \times 10^6 \text{ psi}\right) \cdot \left(\left(10 \text{ Lam}\right) \cdot \left(0.0381 \text{ in}\right) \right) \cdot \left(\left(3.251 \text{ in}\right)^2 + \frac{\left(\left(10 \text{ Lam}\right) \cdot \left(0.0381 \text{ in}\right) \right)^2}{12} \right) \right]^{(m1810)}$$

$$+ \left[\left(0.849 \times 10^6 \text{ psi}\right) \cdot \left(0.0295 \text{ in}\right) \cdot \left(\left(3.045 \text{ in}\right)^2 + \frac{\left(0.0295 \text{ in}\right)^2}{12} \right) \right]^{(cm3205)_{90°}}$$

$$+ \left[\left(4.539 \times 10^6 \text{ psi}\right) \cdot \left(0.0295 \text{ in}\right) \cdot \left(\left(3.016 \text{ in}\right)^2 + \frac{\left(0.0295 \text{ in}\right)^2}{12} \right) \right]^{(cm3205)_{0°}}$$

$$+ \left[\left(4.539 \times 10^6 \text{ psi}\right) \cdot \left(0.0295 \text{ in}\right) \cdot \left(\left(-3.016 \text{ in}\right)^2 + \frac{\left(0.0295 \text{ in}\right)^2}{12} \right) \right]^{(cm3205)_{0°}}$$

$$+ \left[\left(0.849 \times 10^6 \text{ psi}\right) \cdot \left(0.0295 \text{ in}\right) \cdot \left(\left(-3.045 \text{ in}\right)^2 + \frac{\left(0.0295 \text{ in}\right)^2}{12} \right) \right]^{(cm3205)_{90°}}$$

$$+ \left[3.878 \left(3.829 \times 10^6 \text{ psi}\right) \cdot \left(\left(10 \text{ Lam}\right) \cdot \left(0.0381 \text{ in}\right) \right) \cdot \left(\left(3.251 \text{ in}\right)^2 + \frac{\left(\left(10 \text{ Lam}\right) \cdot \left(0.0381 \text{ in}\right) \right)^2}{12} \right) \right]^{(m1810)}$$

$$+ \left[\left(0.849 \times 10^6 \text{ psi}\right) \cdot \left(0.0295 \text{ in}\right) \cdot \left(\left(-3.456 \text{ in}\right)^2 + \frac{\left(0.0295 \text{ in}\right)^2}{12} \right) \right]^{(cm3205)_{90°}}$$

$$+ \left[\left(4.539 \times 10^6 \text{ psi}\right) \cdot \left(0.0295 \text{ in}\right) \cdot \left(\left(-3.485 \text{ in}\right)^2 + \frac{\left(0.0295 \text{ in}\right)^2}{12} \right) \right]^{(cm3205)_{0°}}$$

$$= 38.019 \times 10^6 \text{ psi} \cdot \text{in}^3$$

Similarly,

$$D_{11} = 38.019 \times 10^6 \text{ psi} \cdot \text{in}^3$$
$$D_{22} = 12.97 \times 10^6 \text{ psi} \cdot \text{in}^3$$
$$D_{66} = 3.989 \times 10^6 \text{ psi} \cdot \text{in}^3$$
$$D_{12} = 2.381 \times 10^6 \text{ psi} \cdot \text{in}^3$$
$$D_{16} = D_{26} = 0 \text{ psi} \cdot \text{in}^3$$

Constitutive Equation [ABD] Matrix for Sandwich – First Approach

$$\begin{bmatrix} N_1 \\ N_2 \\ N_6 \\ \cdots \\ M_1 \\ M_2 \\ M_6 \end{bmatrix} = \left[\begin{array}{ccc:ccc:c} 3.591\times10^6 & 0.225\times10^6 & 0 & 0 & 0 & 0 & \\ 0.225\times10^6 & 1.225\times10^6 & 0 & 0 & 0 & 0 & \\ 0 & 0 & 0.376\times10^6 & 0 & 0 & 0 & \\ \cdots & \cdots & \cdots & \cdots & \cdots & \cdots & \\ 0 & 0 & 0 & 38.019\times10^6 & 2.381\times10^6 & 0 & \\ 0 & 0 & 0 & 2.381\times10^6 & 12.97\times10^6 & 0 & \\ 0 & 0 & 0 & 0 & 0 & 3.989\times10^6 & \end{array}\right] \cdot \begin{bmatrix} \varepsilon_{a1} \\ \varepsilon_{a2} \\ \varepsilon_{a6} \\ \cdots \\ \kappa_1 \\ \kappa_2 \\ \kappa_6 \end{bmatrix}$$

*Values are in psi

2.4.2.2 – Second Approach - Equivalent Face Sheet Properties

Constitutive Equation for Individual Face Sheet

$$\begin{bmatrix} N_1 \\ N_2 \\ N_6 \\ \cdots \\ M_1 \\ M_2 \\ M_6 \end{bmatrix} = \begin{bmatrix} 1.796\times10^6 & 0.112\times10^6 & 0 & \vdots & 0 & 0 & 0 \\ 0.112\times10^6 & 0.612\times10^6 & 0 & \vdots & 0 & 0 & 0 \\ 0 & 0 & 0.188\times10^6 & \vdots & 0 & 0 & 0 \\ \cdots & \cdots & \cdots & \cdots & \cdots & \cdots & \cdots \\ 0 & 0 & 0 & \vdots & 0.035\times10^6 & 0.002\times10^6 & 0 \\ 0 & 0 & 0 & \vdots & 0.002\times10^6 & 0.018\times10^6 & 0 \\ 0 & 0 & 0 & \vdots & 0 & 0 & 0.004\times10^6 \end{bmatrix} \cdot \begin{bmatrix} \varepsilon_{a1} \\ \varepsilon_{a2} \\ \varepsilon_{a6} \\ \cdots \\ \kappa_1 \\ \kappa_2 \\ \kappa_6 \end{bmatrix}$$

*Values from Appendix 2.3 [psi]

Equivalent Axial Properties

$$E_1^N = \frac{A_{11}\cdot A_{22} - A_{12}^2}{h\cdot A_{22}} = \frac{\left(\left(1.796\times10^6\ \text{psi}\cdot\text{in}\right)\cdot\left(0.612\times10^6\ \text{psi}\cdot\text{in}\right) - \left(0.112\times10^6\ \text{psi}\cdot\text{in}\right)^2\right)}{\left(0.499\ \text{in}\right)\cdot\left(0.612\times10^6\ \text{psi}\cdot\text{in}\right)}$$

$$= 3.558\times10^6\ \text{psi}$$

$$E_2^N = \frac{A_{11}\cdot A_{22} - A_{12}^2}{h\cdot A_{11}} = \frac{\left(\left(1.796\times10^6\ \text{psi}\cdot\text{in}\right)\cdot\left(0.612\times10^6\ \text{psi}\cdot\text{in}\right) - \left(0.112\times10^6\ \text{psi}\cdot\text{in}\right)^2\right)}{\left(0.499\ \text{in}\right)\cdot\left(1.796\times10^6\ \text{psi}\cdot\text{in}\right)}$$

$$= 1.212\times10^6\ \text{psi}$$

$$E_6^N = G_{12}^N = \frac{A_{66}}{h} = \frac{\left(0.188\times10^6\ \text{psi}\cdot\text{in}\right)}{\left(0.499\ \text{in}\right)} = .377\times10^6\ \text{psi}$$

$$\nu_{12}^N = \frac{A_{12}}{A_{22}} = \frac{\left(0.112\times10^6\ \text{psi}\cdot\text{in}\right)}{\left(0.612\times10^6\ \text{psi}\cdot\text{in}\right)} = 0.183$$

$$\nu_{21}^N = \frac{A_{12}}{A_{11}} = \frac{\left(0.112\times10^6\ \text{psi}\cdot\text{in}\right)}{\left(1.796\times10^6\ \text{psi}\cdot\text{in}\right)} = 0.062$$

Determine Neutral Axis for Sandwich Panel

$$\bar{y}^{k} = \frac{\sum_{k=1}^{3} E_1^k \cdot t^k \cdot \bar{y}^{k}}{\sum_{k=1}^{3} E_1^k \cdot t^k} \quad \text{where, } \bar{y} \text{ is from bottom of panel}$$

$$= \frac{\left[\left(3.558\times10^{6}\ \text{psi}\right)\cdot\left(0.499\ \text{in}\right)\cdot\left(6.7505\ \text{in}\right)\right]^{Top} + \left[\left(3.558\times10^{6}\ \text{psi}\right)\cdot\left(0.499\ \text{in}\right)\cdot\left(0.2495\ \text{in}\right)\right]^{Bottom}}{\left[\left(3.558\times10^{6}\ \text{psi}\right)\cdot\left(0.499\ \text{in}\right)\right]^{Top} + \left[\left(3.558\times10^{6}\ \text{psi}\right)\cdot\left(0.499\ \text{in}\right)\right]^{Bottom}}$$

$$= 3.5\ \text{in}$$

Determine Transformed Stiffness Coefficients Q_{ij} for Face Sheets

$$h^{(1)} = h^{(2)} = 0.499\ \text{in}$$

$$Q_{11}^{(1)} = Q_{11}^{(2)} = Q_{11}^{'} = \frac{E_1^N}{\left(1-\nu_{12}^N\cdot\nu_{21}^N\right)} = \frac{\left(3.558\times10^{6}\ \text{psi}\right)}{\left(1-\left(0.183\right)\cdot\left(0.062\right)\right)}$$

$$= 3.599\times10^{6}\ \text{psi}$$

$$Q_{22}^{(1)} = Q_{22}^{(2)} = Q_{22}^{'} = \frac{E_2^N}{\left(1-\nu_{12}^N\cdot\nu_{21}^N\right)} = \frac{\left(1.212\times10^{6}\ \text{psi}\right)}{\left(1-\left(0.183\right)\cdot\left(0.062\right)\right)}$$

$$= 1.226\times10^{6}\ \text{psi}$$

$$Q_{66}^{(1)} = Q_{66}^{(2)} = Q_{66}^{'} = E_6^N = G_{12}^N = 0.377\times10^{6}\ \text{psi}$$

$$Q_{12}^{(1)} = Q_{12}^{(2)} = Q_{12}^{'} = \frac{E_2^N\cdot\nu_{12}^N}{\left(1-\nu_{12}^N\cdot\nu_{21}^N\right)} = \frac{\left(1.212\times10^{6}\ \text{psi}\right)\cdot\left(0.183\right)}{\left(1-\left(0.183\right)\cdot\left(0.062\right)\right)} = 0.224\times10^{6}\ \text{psi}$$

Axial Stiffness for Sandwich Panel

$$A_{11} = \sum_{k=1}^{2} Q_{11}^{(k)} \cdot h^{(k)} = 2 \cdot \left(3.599 \times 10^{6} \text{ psi}\right) \cdot \left(0.499 \text{ in}\right)$$
$$= 3.591 \times 10^{6} \text{ psi} \cdot \text{in}$$

Similarly,

$$A_{11} = 3.592 \times 10^{6} \text{ psi} \cdot \text{in}$$
$$A_{22} = 1.224 \times 10^{6} \text{ psi} \cdot \text{in}$$
$$A_{66} = 0.376 \times 10^{6} \text{ psi} \cdot \text{in}$$
$$A_{12} = 0.224 \times 10^{6} \text{ psi} \cdot \text{in}$$
$$A_{16} = A_{26} = 0 \text{ psi} \cdot \text{in}$$

Coupling Stiffness for Sandwich Panel

$$B_{11} = \sum_{k=1}^{2} Q_{11}^{(k)} \cdot \bar{x}_{3}^{(k)} \cdot h^{(k)} = \left(3.599 \times 10^{6} \text{ psi}\right) \cdot \left(3.2505 \text{ in}\right) \cdot \left(0.499 \text{ in}\right)$$
$$+ \left(3.599 \times 10^{6} \text{ psi}\right) \cdot \left(-3.2505 \text{ in}\right) \cdot \left(0.499 \text{ in}\right) = 0 \text{ psi} \cdot \text{in}^{2}$$

Similarly,

$$B_{11} = B_{22} = B_{66} = B_{12} = B_{16} = B_{26} = 0 \text{ psi} \cdot \text{in}^{2}$$

Flexural Stiffness for Sandwich Panel

$$D_{11} = \sum_{k=1}^{2} Q_{11}^{(k)} \cdot h^{(k)} \cdot \left(\overline{x_3^{(k)}}^2 + \frac{h^{(k)^2}}{12} \right)$$

$$= \left[\left(3.599 \times 10^6 \text{ psi}\right) \cdot \left(0.499 \text{ in}\right) \cdot \left(\left(3.2505 \text{ in}\right)^2 + \frac{\left(0.499 \text{ in}\right)^2}{12} \right) \right]^{\text{(Top Face Sheet)}}$$

$$+ \left[\left(3.599 \times 10^6 \text{ psi}\right) \cdot \left(0.499 \text{ in}\right) \cdot \left(\left(-3.2505 \text{ in}\right)^2 + \frac{\left(0.499 \text{ in}\right)^2}{12} \right) \right]^{\text{(Bottom Face Sheet)}}$$

$$= 38.025 \times 10^6 \text{ psi} \cdot \text{in}^3$$

Similarly,

$$D_{11} = 38.025 \times 10^6 \text{ psi} \cdot \text{in}^3$$
$$D_{22} = 12.953 \times 10^6 \text{ psi} \cdot \text{in}^3$$
$$D_{66} = 3.983 \times 10^6 \text{ psi} \cdot \text{in}^3$$
$$D_{12} = 2.366 \times 10^6 \text{ psi} \cdot \text{in}^3$$
$$D_{16} = D_{26} = 0 \text{ psi} \cdot \text{in}^3$$

Constitutive Equation for Individual Face Sheet – Second Approach

$$\begin{bmatrix} N_1 \\ N_2 \\ N_6 \\ \cdots \\ M_1 \\ M_2 \\ M_6 \end{bmatrix} = \begin{bmatrix} 3.592 \times 10^6 & 0.224 \times 10^6 & 0 & \vdots & 0 & 0 & 0 \\ 0.224 \times 10^6 & 1.224 \times 10^6 & 0 & \vdots & 0 & 0 & 0 \\ 0 & 0 & 0.376 \times 10^6 & \vdots & 0 & 0 & 0 \\ \cdots & \cdots & \cdots & \cdots & \cdots & \cdots & \cdots \\ 0 & 0 & 0 & \vdots & 38.025 \times 10^6 & 2.366 \times 10^6 & 0 \\ 0 & 0 & 0 & \vdots & 2.366 \times 10^6 & 12.953 \times 10^6 & 0 \\ 0 & 0 & 0 & \vdots & 0 & 0 & 3.983 \times 10^6 \end{bmatrix} \cdot \begin{bmatrix} \varepsilon_{a1} \\ \varepsilon_{a2} \\ \varepsilon_{a6} \\ \cdots \\ \kappa_1 \\ \kappa_2 \\ \kappa_6 \end{bmatrix}$$

* Values are in psi

2.4.2.3 – Third Approach - Transform [ABD] Matrix with Parallel Axis Theorem

Constitutive Equation for Individual Face Sheet

$$\begin{bmatrix} N_1 \\ N_2 \\ N_6 \\ \cdots \\ M_1 \\ M_2 \\ M_6 \end{bmatrix} = \begin{bmatrix} 1.796\times10^6 & 0.112\times10^6 & 0 & \vdots & 0 & 0 & 0 \\ 0.112\times10^6 & 0.612\times10^6 & 0 & \vdots & 0 & 0 & 0 \\ 0 & 0 & 0.188\times10^6 & \vdots & 0 & 0 & 0 \\ \cdots & \cdots & \cdots & \cdots & \cdots & \cdots & \cdots \\ 0 & 0 & 0 & \vdots & 0.035\times10^6 & 0.002\times10^6 & 0 \\ 0 & 0 & 0 & \vdots & 0.002\times10^6 & 0.018\times10^6 & 0 \\ 0 & 0 & 0 & \vdots & 0 & 0 & 0.004\times10^6 \end{bmatrix} \cdot \begin{bmatrix} \varepsilon_{a1} \\ \varepsilon_{a2} \\ \varepsilon_{a6} \\ \cdots \\ \kappa_1 \\ \kappa_2 \\ \kappa_6 \end{bmatrix}$$

* Values are in psi

Determine Neutral Axis for Sandwich Panel

$$\bar{y}^k = \frac{\sum_{k=1}^{2}\left(\frac{A_{11}^k \cdot A_{22}^k + A_{12}^{k\,2}}{A_{22}^k}\right)\cdot \bar{y}^k}{\sum_{k=1}^{2}\left(\frac{A_{11}^k \cdot A_{22}^k + A_{12}^{k\,2}}{A_{22}^k}\right)} \quad \text{where, } \bar{y} \text{ is from bottom of panel}$$

$$= \frac{\left[\frac{\left(1.796\times10^6\ \text{psi}\right)\cdot\left(0.612\times10^6\ \text{psi}\right)+\left(0.112\times10^6\ \text{psi}\right)^2}{\left(0.612\times10^6\ \text{psi}\right)\cdot\left(6.7505\ \text{in}\right)^{-1}}\right]^{Top} + \left[\frac{\left(1.796\times10^6\ \text{psi}\right)\cdot\left(0.612\times10^6\ \text{psi}\right)+\left(0.112\times10^6\ \text{psi}\right)^2}{\left(0.612\times10^6\ \text{psi}\right)\cdot\left(0.2495\ \text{in}\right)^{-1}}\right]^{Bottom}}{\left[\frac{\left(1.796\times10^6\ \text{psi}\right)\cdot\left(0.612\times10^6\ \text{psi}\right)+\left(0.112\times10^6\ \text{psi}\right)^2}{\left(0.612\times10^6\ \text{psi}\right)}\right]^{Top} + \left[\frac{\left(1.796\times10^6\ \text{psi}\right)\cdot\left(0.612\times10^6\ \text{psi}\right)+\left(0.112\times10^6\ \text{psi}\right)^2}{\left(0.612\times10^6\ \text{psi}\right)}\right]^{Bottom}}$$

$= 3.5$ in

Axial Stiffness for Sandwich Panel

$$A_{ij}^S = A_{ij}^L$$

$$A_{11}^S = A_{11}^{L-Top} + A_{11}^{L-Bottom} = \left(1.790\times10^6\ \text{psi}\right) + \left(1.790\times10^6\ \text{psi}\right)$$

$$= 3.580\times10^6\ \text{psi}$$

Similarly,

$$A_{11}^S = 3.580\times10^6 \text{ psi}$$
$$A_{22}^S = 1.466\times10^6 \text{ psi}$$
$$A_{66}^S = 0.430\times10^6 \text{ psi}$$
$$A_{12}^S = 0.306\times10^6 \text{ psi}$$
$$A_{16}^S = A_{26}^S = 0 \text{ psi}$$

Axial Stiffness for Sandwich Panel

$$B_{ij}^S = B_{ij}^L + x_O \cdot A_{ij}^L \quad \text{where, } x_O = (3.5 \text{ in}) - \frac{(0.499 \text{ in})}{2} = 3.2505 \text{ in}$$
$$B_{11}^S = \left(B_{11}^{L-Top} + x_O^{L-Top} \cdot A_{11}^{L-Top}\right) + \left(B_{11}^{L-Bottom} + x_O^{L-Bottom} \cdot A_{11}^{L-Bottom}\right)$$
$$= \left((0 \text{ psi}) + (3.2505 \text{ in}) \cdot \left(1.790\times10^6 \text{ psi}\right)\right) + \left((0 \text{ psi}) + (-3.2505 \text{ in}) \cdot \left(1.790\times10^6 \text{ psi}\right)\right)$$
$$= 0 \text{ psi}$$

Similarly,

$$B_{11}^S = B_{22}^S = B_{66}^S = B_{12}^S = B_{16}^S = B_{26}^S = 0 \text{ psi}$$

Axial Stiffness for Sandwich Panel

$$D_{ij}^S = D_{ij}^L + 2 \cdot x_O \cdot B_{ij}^L + x_O^2 \cdot A_{ij}^L \quad \text{where, } x_O = (3.5 \text{ in}) - \frac{(0.499 \text{ in})}{2} = 3.2505 \text{ in}$$
$$D_{11}^S = D_{11}^L + 2 \cdot x_O \cdot B_{11}^L + x_O^2 \cdot A_{11}^L$$
$$= \left((0.035\times10^6 \text{ psi}) + 2 \cdot (3.2505 \text{ in}) \cdot (0 \text{ psi}) + (3.2505 \text{ in})^2 \cdot \left(1.790\times10^6 \text{ psi}\right)\right)$$
$$+ \left((0.035\times10^6 \text{ psi}) + 2 \cdot (-3.2505 \text{ in}) \cdot (0 \text{ psi}) + (-3.2505 \text{ in})^2 \cdot \left(1.790\times10^6 \text{ psi}\right)\right)$$
$$= 37.89\times10^6 \text{ psi}$$

Similarly,

$$D_{11}^S = 37.89\times10^6 \text{ psi}$$
$$D_{22}^S = 15.53\times10^6 \text{ psi}$$
$$D_{66}^S = 4.553\times10^6 \text{ psi}$$
$$D_{12}^S = 3.239\times10^6 \text{ psi}$$
$$D_{16}^S = D_{26}^S = 0 \text{ psi}$$

Constitutive Equation Sandwich Panel – Third Approach

$$\begin{bmatrix} N_1 \\ N_2 \\ N_6 \\ \cdots \\ M_1 \\ M_2 \\ M_6 \end{bmatrix} = \left[\begin{array}{ccccccc} 3.591\times10^6 & 0.225\times10^6 & 0 & \vdots & 0 & 0 & 0 \\ 0.225\times10^6 & 1.225\times10^6 & 0 & \vdots & 0 & 0 & 0 \\ 0 & 0 & 0.376\times10^6 & \vdots & 0 & 0 & 0 \\ \cdots & \cdots & \cdots & \cdots & \cdots & \cdots & \cdots \\ 0 & 0 & 0 & \vdots & 38.019\times10^6 & 2.381\times10^6 & 0 \\ 0 & 0 & 0 & \vdots & 2.381\times10^6 & 12.97\times10^6 & 0 \\ 0 & 0 & 0 & \vdots & 0 & 0 & 3.989\times10^6 \end{array}\right] \cdot \begin{bmatrix} \varepsilon_{a1} \\ \varepsilon_{a2} \\ \varepsilon_{a6} \\ \cdots \\ \kappa_1 \\ \kappa_2 \\ \kappa_6 \end{bmatrix}$$

* Variation is due to roundoff error

* Values are in psi

2.4.3– Sandwich Panel Reactions: 3-Point Bending

$L = 75.75 \text{ in}$

$b = 13.4 \text{ in}$

$$\overline{D}_{11} = b \cdot D_{11} = \left(13.4 \text{ in}\right) \cdot \left(38.019 \times 10^6 \text{ psi} \cdot \text{in}^3\right) = 509.45 \times 10^6 \text{ psi} \cdot \text{in}^4$$

Euler-Bernoulli:3-point Bending at 8Kips

$$M_1^E = \frac{P \cdot x_1}{2}$$

$$M_{\max}^E = \frac{P \cdot L}{4} = \frac{\left(8 \text{ kips}\right) \cdot \left(75.75 \text{ in}\right)}{4} = 151.5 \text{ in} \cdot \text{kip}$$

$$w_1^E = -\frac{P \cdot x_1}{48 \cdot \overline{D}_{11}} \cdot \left(3 \cdot L^2 - 4 \cdot {x_1}^2\right)$$

$$w_{\max}^E = -\frac{P \cdot L^3}{48 \cdot \overline{D}_{11}} = -\frac{\left(8000 \text{ lbs}\right) \cdot \left(75.75 \text{ in}\right)^3}{48 \cdot \left(509.45 \times 10^6 \text{ psi} \cdot \text{in}^4\right)} = -0.1421 \text{ in}$$

Appendix 2.5

Stresses and Strains in the Sandwich Panel

2.5.1– Strain Profile for Sandwich Panel

Panel Reactions: 3-point Bending at 8Kips

$$M^{E}_{\max} = 151.5 \text{ in} \cdot \text{kip}$$
$$w^{E}_{\max} = -0.1421 \text{ in}$$

abd Matrix for Sandwich Panel

$$\begin{bmatrix} \varepsilon_{a1} \\ \varepsilon_{a2} \\ \varepsilon_{a6} \\ \cdots \\ \kappa_1 \\ \kappa_2 \\ \kappa_6 \end{bmatrix} = \begin{bmatrix} 0.282\times10^{-6} & 0.052\times10^{-6} & 0 & \vdots & 0 & 0 & 0 \\ 0.052\times10^{-6} & 0.826\times10^{-6} & 0 & \vdots & 0 & 0 & 0 \\ 0 & 0 & 2.654\times10^{-6} & \vdots & 0 & 0 & 0 \\ \cdots & \cdots & \cdots & \cdots & \cdots & \cdots & \cdots \\ 0 & 0 & 0 & \vdots & 0.0266\times10^{-6} & -0.001\times10^{-6} & 0 \\ 0 & 0 & 0 & \vdots & -0.001\times10^{-6} & 0.078\times10^{-6} & 0 \\ 0 & 0 & 0 & \vdots & 0 & 0 & 0.251\times10^{-6} \end{bmatrix} \cdot \begin{bmatrix} N_1 \\ N_2 \\ N_6 \\ \cdots \\ M_1 \\ M_2 \\ M_6 \end{bmatrix}$$

* Values are in psi

Flexural Curvature and Strains in Top Biaxial Laminas

$$\kappa_1 = \frac{d_{11} \cdot M_1}{b} = \frac{\left(0.0266\times10^{-3} \text{ ksi}^{-1} \cdot \text{in}^{-3}\right) \cdot \left(151.5 \text{ in} \cdot \text{kip}\right)}{\left(13.4 \text{ in}\right)} = 0.00030 \text{ in}^{-1}$$

$$\kappa_2 = \frac{d_{12} \cdot M_1}{b} = \frac{\left(-0.001\times10^{-3} \text{ ksi}^{-1} \cdot \text{in}^{-3}\right) \cdot \left(151.5 \text{ in} \cdot \text{kip}\right)}{\left(13.4 \text{ in}\right)} = 0.00001 \text{ in}^{-1}$$

$\kappa_2 \approx 0$ Therefor it is ignored

$$\varepsilon^{Top}_{(cm3205)_{0^\circ}} = \kappa_1 \cdot X_3^{Top(cm3205)_{0^\circ}} = \left(0.0003007 \text{ in}^{-1}\right) \cdot \left(3.5 \text{ in}\right) = 0.00105$$

$$\varepsilon^{Top}_{(cm3205)_{90°}} = \kappa_1 \cdot X_3^{Top(cm3205)_{90°}} = \left(0.00030\ \text{in}^{-1}\right)\cdot\left(3.4705\ \text{in}\right) = 0.001041$$

$$\varepsilon^{Bottom}_{(cm3205)_{90°}} = \kappa_1 \cdot X_3^{Bottom(cm3205)_{90°}} = \left(0.00030\ \text{in}^{-1}\right)\cdot\left(3.4441\ \text{in}\right) = 0.001032$$

Flexural Stresses in Top Biaxial Laminas

$$\sigma^{Top}_{(cm3205)_{0°}} = \varepsilon \cdot Q_{11}^{(cm3205)_{0°}} = \left(0.00105\right)\cdot\left(4539\ \text{ksi}\right) = 4.77\ \text{ksi}$$

$$\sigma^{Bottom}_{(cm3205)_{0°}} = \varepsilon \cdot Q_{11}^{(cm3205)_{0°}} = \left(0.001041\right)\cdot\left(4539\ \text{ksi}\right) = 4.73\ \text{ksi}$$

$$\sigma^{Top}_{(cm3205)_{0°}} = \varepsilon \cdot Q_{11}^{(cm3205)_{90°}} = \left(0.001041\right)\cdot\left(849\ \text{ksi}\right) = 0.88\ \text{ksi}$$

$$\sigma^{Bottom}_{(cm3205)_{0°}} = \varepsilon \cdot Q_{11}^{(cm3205)_{90°}} = \left(0.001032\right)\cdot\left(849\ \text{ksi}\right) = 0.88\ \text{ksi}$$

In a similar manor all the strains and stresses can be found though out the sandwich cross-section.

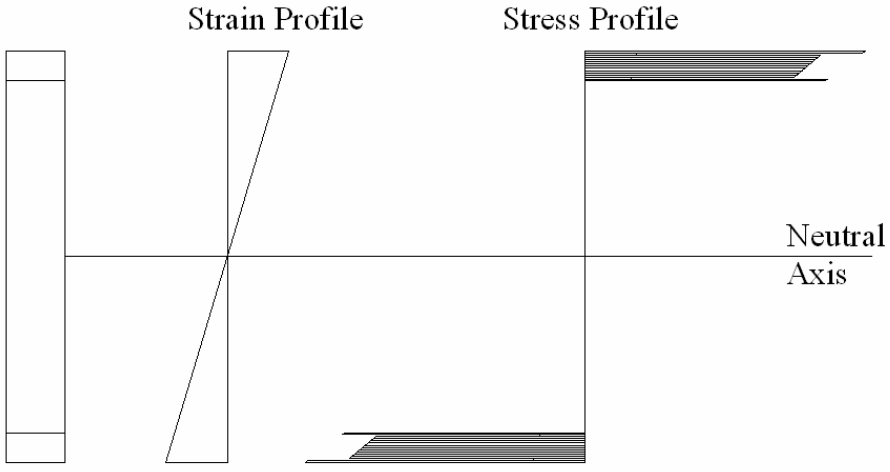

Appendix 2.6

[ABD] Parallel Axis Derivation

Parallel Axis for A_{ij}

$$A_{ij}^{S} = \sum_{k=1}^{n} Q_{ij}^{(k)} \cdot \left(x_3^{(k)} - x_3^{(k-1)} \right) = \sum_{k=1}^{n} Q_{ij}^{(k)} \cdot \left(\left(x_L^{(k)} + x_O \right) - \left(x_L^{(k-1)} + x_O \right) \right) =$$

$$= \sum_{k=1}^{n} \left(Q_{ij}^{(k)} \cdot \left(x_L^{(k)} + \cancel{x_O} - x_L^{(k-1)} - \cancel{x_O} \right) \right) =$$

$$= \sum_{k=1}^{n} \left(Q_{ij}^{(k)} \cdot \left(x_L^{(k)} - x_L^{(k-1)} \right) \right) =$$

$$= A_{ij}^{L}$$

Where, xo is the offset from the neutral axis.

Parallel Axis for B_{ij}

$$B_{ij}^{S} = \frac{1}{2} \cdot \sum_{k=1}^{n} Q_{ij}^{(k)} \cdot \left(x_3^{(k)^2} - x_3^{(k-1)^2} \right) = \frac{1}{2} \cdot \sum_{k=1}^{n} Q_{ij}^{(k)} \cdot \left(\left(x_L^{(k)^2} + x_O \right) - \left(x_L^{(k-1)^2} + x_O \right) \right) =$$

$$= \frac{1}{2} \cdot \sum_{k=1}^{n} \left(Q_{ij}^{(k)} \cdot \left(x_L^{(k)^2} + 2 \cdot x_O \cdot x_L^{(k)} + \cancel{x_O^2} - x_L^{(k-1)^2} - 2 \cdot x_O \cdot x_L^{(k-1)} - \cancel{x_O^2} \right) \right) =$$

$$= \frac{1}{2} \cdot \sum_{k=1}^{n} \left(Q_{ij}^{(k)} \cdot \left(\left(x_L^{(k)^2} - x_L^{(k-1)^2} \right) + \left(2 \cdot x_L^{(k)} - 2 \cdot x_L^{(k-1)} \right) \cdot x_O \right) \right) =$$

$$= \frac{1}{2} \cdot \sum_{k=1}^{n} \left(Q_{ij}^{(k)} \cdot \left(x_L^{(k)^2} - x_L^{(k-1)^2} \right) + 2 \cdot Q_{ij}^{(k)} \cdot \left(x_L^{(k)} - x_L^{(k-1)} \right) \cdot x_O \right) =$$

$$= \frac{1}{2} \cdot \sum_{k=1}^{n} Q_{ij}^{(k)} \cdot \left(x_L^{(k)^3} - x_L^{(k-1)^3} \right) + \sum_{k=1}^{n} Q_{ij}^{(k)} \cdot \left(x_L^{(k)} - x_L^{(k-1)} \right) \cdot x_O =$$

$$= B_{ij}^{L} + x_O \cdot A_{ij}^{L}$$

Where, xo is the offset from the neutral axis.

Parallel Axis for D_{ij}

$$D_{ij}^{S} = \frac{1}{3}\cdot\sum_{k=1}^{n} Q_{ij}^{(k)}\cdot\left(x_3^{(k)^3} - x_3^{(k-1)^3}\right) = \frac{1}{3}\cdot\sum_{k=1}^{n} Q_{ij}^{(k)}\cdot\left(\left(x_L^{(k)^3} + x_O\right) - \left(x_L^{(k-1)^3} + x_O\right)\right) =$$

$$= \frac{1}{3}\cdot\sum_{k=1}^{n}\left(Q_{ij}^{(k)}\cdot\left(x_L^{(k)^3} + 3\cdot x_O\cdot x_L^{(k)^2} + 3\cdot x_O^2\cdot x_L^{(k)} + \cancel{x_O^3} - x_L^{(k-1)^3} - 3\cdot x_O\cdot x_L^{(k-1)^2} - 3\cdot x_O^2\cdot x_L^{(k-1)} - \cancel{x_O^3}\right)\right) =$$

$$= \frac{1}{3}\cdot\sum_{k=1}^{n}\left(Q_{ij}^{(k)}\cdot\left(\left(x_L^{(k)^3} - x_L^{(k-1)^3}\right) + \left(3\cdot x_L^{(k)^2} + 3\cdot x_O\cdot x_L^{(k)} - 3\cdot x_L^{(k-1)^2} - 3\cdot x_O\cdot x_L^{(k-1)}\right)\cdot x_O\right)\right) =$$

$$= \frac{1}{3}\cdot\sum_{k=1}^{n}\left(Q_{ij}^{(k)}\cdot\left(x_L^{(k)^3} - x_L^{(k-1)^3}\right) + 3\cdot Q_{ij}^{(k)}\cdot\left(x_L^{(k)^2} - x_L^{(k-1)^2}\right)\cdot x_O + 3\cdot Q_{ij}^{(k)}\cdot\left(x_L^{(k)} - x_L^{(k-1)}\right)\cdot x_O^2\right) =$$

$$= \frac{1}{3}\cdot\sum_{k=1}^{n} Q_{ij}^{(k)}\cdot\left(x_L^{(k)^3} - x_L^{(k-1)^3}\right) + \sum_{k=1}^{n} Q_{ij}^{(k)}\cdot\left(x_L^{(k)^2} - x_L^{(k-1)^2}\right)\cdot x_O + \sum_{i=1}^{n} Q_{ij}^{(k)}\cdot\left(x_L^{(k)} - x_L^{(k-1)}\right)\cdot x_O^2 =$$

$$= D_{ij}^{L} + 2\cdot x_O\cdot B_{ij}^{L} + x_O^2\cdot A_{ij}^{L}$$

Where, xo is the offset from the neutral axis.

Appendix 2.7

Bernoulli and Timoshenko Beam Theory

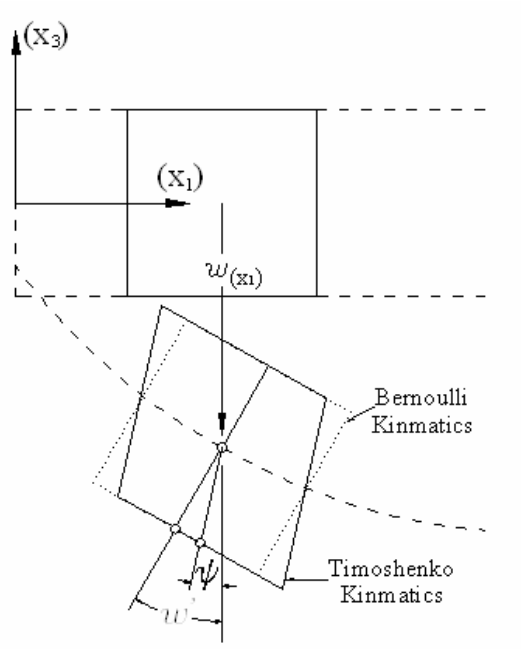

2.7.1 - Standard Equilibrium Equations: Flexure with Bending About the x_2 Axis

Timoshenko Beam Theory

$$M^T = E \cdot I \cdot \frac{d\psi}{dx_1}$$

$$Q^T = \frac{dM}{dx_1} = \frac{d}{dx_1}\left[E \cdot I \cdot \frac{d\psi}{dx_1} \right]$$

$$q^T = \frac{d^2M}{dx_1^{\,2}} = \frac{d^2}{dx_1^{\,2}}\left[E \cdot I \cdot \frac{d\psi}{dx_1} \right]$$

$$\frac{dw}{dx_1} - \psi^T_{(x_1)} = \frac{-Q}{k^s \cdot G \cdot A}$$

$$\kappa_1 = \frac{d\psi}{dx_1}$$

Euler-Bernoulli Theory

$$M^E = E \cdot I \cdot \frac{d^2w}{dx_1^{\,2}}$$

$$Q^E = \frac{dM}{dx_1} = \frac{d}{dx_1}\left[E \cdot I \cdot \frac{d^2w}{dx_1^{\,2}} \right]$$

$$q^E = \frac{d^2M}{dx_1^{\,2}} = \frac{d^2}{dx_1^{\,2}}\left[E \cdot I \cdot \frac{d^2w}{dx_1^{\,2}} \right]$$

$$\frac{dw}{dx_1} - \psi^E_{(x_1)} \approx 0$$

$$\psi^E = \frac{dw}{dx_1}$$

2.7.2 - Composite Equilibrium Equations: Flexure with Bending About the x_2 Axis

Timoshenko Beam Theory

$$M^T_{(x_1)} = b \cdot \left(B_{11} \cdot \varepsilon_{a1} + D_{11} \cdot \frac{d\psi^T}{dx_1} \right)$$

$$Q^T_{(x_1)} = \frac{d}{dx_1} \left[b \cdot \left(B_{11} \cdot \varepsilon_{a1} + D_{11} \cdot \frac{d\psi^T}{dx_1} \right) \right]$$

$$q^T_{(x_1)} = \frac{d^2}{dx_1{}^2} \left[b \cdot \left(B_{11} \cdot \varepsilon_{a1} + D_{11} \cdot \frac{d\psi_1}{dx_1} \right) \right]$$

$$\frac{dw}{dx_1} - \psi^T_{(x_1)} = \frac{-Q^T_{(x_1)}}{k^s \cdot b \cdot A^s_{55}}$$

$$\kappa_1 = \frac{d\psi_1}{dx_1}$$

Euler-Bernoulli Theory

$$M^E_{(x_1)} = b \cdot \left(B_{11} \cdot \varepsilon_{a1} + D_{11} \cdot \frac{d^2 w}{dx_1{}^2} \right)$$

$$Q^E_{(x_1)} = \frac{d}{dx_1} \left[b \cdot \left(B_{11} \cdot \varepsilon_{a1} + D_{11} \cdot \frac{d^2 w}{dx_1{}^2} \right) \right]$$

$$q^E_{(x_1)} = \frac{d^2}{dx_1{}^2} \left[b \cdot \left(B_{11} \cdot \varepsilon_{a1} + D_{11} \cdot \frac{d^2 w}{dx_1{}^2} \right) \right]$$

$$\frac{dw}{dx_1} - \psi^E_{(x_1)} = \frac{-Q^E_{(x_1)}}{k^s \cdot b \cdot A^s_{55}} = \varepsilon_5 \approx 0$$

$$\psi^E_{(x_1)} = \frac{dw}{dx_1}$$

Appendix 2.8

Euler-Bernoulli vs. Timshenko Beam Theory

$$M^{E}_{(x_1)} = -\overline{D}_{11} \cdot \frac{d^2 w^E}{dx_1^{\,2}} \qquad M^{T}_{(x_1)} = -\overline{D}_{11} \cdot \frac{d\psi}{dx_1}$$

$$Q^{E}_{(x_1)} = \frac{dM^{E}_{(x_1)}}{dx_1} = -\overline{D}_{11} \cdot \frac{d^3 w^E}{dx_1^{\,3}} \qquad Q^{T}_{(x_1)} = -k^s \cdot G \cdot A \cdot \left(\psi_{(x_1)} - \frac{dw^T}{dx_1} \right)$$

Assume [B] matrix is zero

Equilibrium Equations

$$\frac{dM_{(x_1)}}{dx_1} = Q_{(x_1)} \qquad \frac{dQ_{(x_1)}}{dx} = -q_{(x_1)}$$

Euler-Bernoulli Governing Equation

$$-\overline{D}_{11} \cdot \frac{d^4 w^E}{dx_1^{\,4}} = \frac{d^2 M^{E}_{(x_1)}}{dx^2} = -q_{(x_1)}$$

Timoshenko Governing Equation

$$k^s \cdot G \cdot A \cdot \left(\psi_{(x_1)} - \frac{dw^T}{dx_1} \right) = \overline{D}_{11} \cdot \frac{d^2 \psi}{dx_1^{\,2}}$$

$$k^s \cdot G \cdot A \cdot \left(\frac{d\psi_{(x_1)}}{dx} - \frac{d^2 w^T}{dx_1^{\,2}} \right) = \overline{D}_{11} \cdot \frac{d^3 \psi}{dx_1^{\,3}} = q_{(x_1)}$$

Therefore, from the Timoshenko moment equation we get,

$$-\overline{D}_{11} \cdot \frac{d^3\psi}{dx_1^{\,3}} = \frac{d^2 M^T_{(x_1)}}{dx^2} = -q_{(x_1)}$$

And with the Euler-Bernoulli Governing Equation we get,

$$-\overline{D}_{11} \cdot \frac{d^3\psi}{dx_1^{\,3}} = \frac{d^2 M^T_{(x_1)}}{dx^2} = -q_{(x_1)} = \frac{d^2 M^E_{(x_1)}}{dx^2} = -\overline{D}_{11} \cdot \frac{d^4 w^E}{dx_1^{\,4}}$$

$$\frac{d^3\psi}{dx_1^{\,3}} = \frac{d^4 w^E}{dx_1^{\,4}}$$

And integrating multiple times we get,

$$\psi_{(x_1)} = \frac{dw^E}{dx_1} + C_1 \cdot \frac{x_1^{\,2}}{2} + C_2 \cdot x_1 + C_3$$

Differentiating once,

$$\frac{d\psi}{dx} = \frac{d^2 w^E}{dx_1^{\,2}} + C_1 \cdot x_1 + C_2 \quad \therefore -\frac{M^T_{(x_1)}}{\overline{D}_{11}} = -\frac{M^E_{(x_1)}}{\overline{D}_{11}} + C_1 \cdot x_1 + C_2$$

And again,

$$\frac{d^2\psi}{dx^2} = \frac{d^3 w^E}{dx_1^{\,3}} + C_1 \quad \therefore -\frac{Q^T_{(x_1)}}{\overline{D}_{11}} = -\frac{Q^E_{(x_1)}}{\overline{D}_{11}} + C_1$$

Entering these results into the Timoshenko governing equation we get,

$$k^s \cdot G \cdot A \cdot \left(\psi_{(x_1)} - \frac{dw^T}{dx_1} \right) = \overline{D}_{11} \cdot \frac{d^2\psi}{dx_1^{\,2}}$$

$$k^s \cdot G \cdot A \cdot \left(\left(\frac{dw^E}{dx_1} + C_1 \cdot \frac{x_1^{\,2}}{2} + C_2 \cdot x_1 + C_3 \right) - \frac{dw^T}{dx_1} \right) = \overline{D}_{11} \left(\frac{d^3 w^E}{dx_1^{\,3}} + C_1 \right)$$

$$\left(\frac{dw^E}{dx_1} + C_1 \cdot \frac{x_1^{\,2}}{2} + C_2 \cdot x_1 + C_3 \right) - \frac{dw^T}{dx_1} = \frac{\overline{D}_{11} \left(\frac{d^3 w^E}{dx_1^{\,3}} + C_1 \right)}{k^s \cdot G \cdot A}$$

$$\frac{dw^T}{dx_1} = -\frac{\overline{D}_{11} \left(\frac{d^3 w^E}{dx_1^{\,3}} + C_1 \right)}{k^s \cdot G \cdot A} + \left(\frac{dw^E}{dx_1} + C_1 \cdot \frac{x_1^{\,2}}{2} + C_2 \cdot x_1 + C_3 \right)$$

$$\frac{dw^T}{dx_1} = \frac{dw^E}{dx_1} + \frac{-\overline{D}_{11} \cdot \frac{d^3 w^E}{dx_1^{\,3}}}{k^s \cdot G \cdot A} + C_1 \cdot \left(\frac{x_1^{\,2}}{2} - \frac{\overline{D}_{11}}{k^s \cdot G \cdot A} \right) + C_2 \cdot x_1 + C_3$$

Integrating we get,

$$w^T_{(x_1)} = w^E_{(x_1)} + \frac{-\overline{D}_{11} \cdot \frac{d^2 w^E}{dx_1^{\,2}}}{k^s \cdot G \cdot A} + C_1 \cdot \left(\frac{x_1^{\,3}}{6} - \frac{\overline{D}_{11} \cdot x_1}{k^s \cdot G \cdot A} \right) + \frac{C_2 \cdot x_1^{\,2}}{2} + C_3 \cdot x_1 + C_4$$

$$w^T_{(x_1)} = w^E_{(x_1)} + \frac{M^E_{(x_1)}}{k^s \cdot G \cdot A} + C_1 \cdot \left(\frac{x_1^{\,3}}{6} - \frac{\overline{D}_{11} \cdot x_1}{k^s \cdot G \cdot A} \right) + \frac{C_2 \cdot x_1^{\,2}}{2} + C_3 \cdot x_1 + C_4$$

Our equations are now,

$$\psi_{(x_1)} = \frac{dw^E}{dx_1} + C_1 \cdot \frac{x_1^{\,2}}{2} + C_2 \cdot x_1 + C_3$$

$$-\frac{M^T_{(x_1)}}{\overline{D}_{11}} = -\frac{M^E_{(x_1)}}{\overline{D}_{11}} + C_1 \cdot x_1 + C_2$$

$$-\frac{Q^T_{(x_1)}}{\overline{D}_{11}} = -\frac{Q^E_{(x_1)}}{\overline{D}_{11}} + C_1$$

$$w^T_{(x_1)} = w^E_{(x_1)} + \frac{M^E_{(x_1)}}{k^s \cdot G \cdot A} + C_1 \cdot \left(\frac{x_1^{\,3}}{6} - \frac{\overline{D}_{11} \cdot x_1}{k^s \cdot G \cdot A} \right) + \frac{C_2 \cdot x_1^{\,2}}{2} + C_3 \cdot x_1 + C_4$$

For a simply supported beam we have the following boundary conditions at $x = 0,\ x = l$

$$w^T = w^E = M^T = M^E = 0 \quad \therefore C_1 = C_2 = C_3 = C_4 = 0$$

So for a simply supported beam we have the following equations,

$$\psi_{(x_1)} = \frac{dw^E}{dx_1}$$

$$M^T_{(x_1)} = M^E_{(x_1)}$$

$$Q^T_{(x_1)} = Q^E_{(x_1)}$$

$$w^T_{(x_1)} = w^E_{(x_1)} + \frac{M^E_{(x_1)}}{k^s \cdot G \cdot A}$$

Appendix 2.9

3-Point Bending Equation Derivation

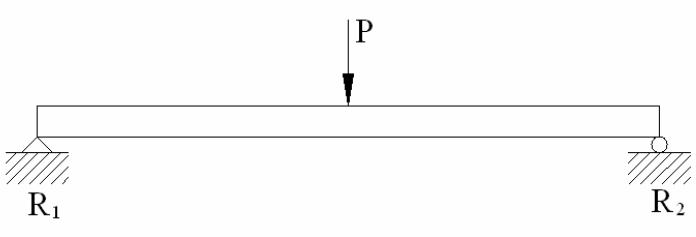

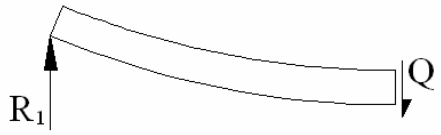

Boundary Conditions:

Deflection: $w_{[x_1=0]} = 0$

Rotaion about X_2 Axis: $\psi = \dfrac{dw}{dx_1}_{\left[x_1=L/2\right]} = 0$

Moment: $M = b \cdot \overline{D}_{11} \cdot \dfrac{d^2 w}{dx_1^{\,2}}_{[x_1=0]} = 0$

Shear: $Q = b \cdot \overline{D}_{11} \dfrac{d^3 w}{dx_1^{\,3}}_{\left[x_1=L/2\right]} = -\dfrac{P}{2}$

Distributed Load: $q = b \cdot \overline{D}_{11} \cdot \dfrac{d^4 w}{dx_1^{\,4}} = 0$

Solve for Constants:

$$q = b \cdot \overline{D}_{11} \cdot \frac{d^4 w}{dx_1^{\,4}} = 0$$

$$Q = b \cdot \overline{D}_{11} \frac{d^3 w}{dx_1^{\,3}} = C_1 \qquad \text{and,} \quad b \cdot \overline{D}_{11} \frac{d^3 w}{dx_1^{\,3}}_{\left[x_1=L/2\right]} = -\frac{P}{2} \quad \therefore C_1 = -\frac{P}{2}$$

$$M = b \cdot \overline{D}_{11} \frac{d^2 w}{dx_1^{\,2}} = -\frac{P \cdot x_1}{2} + C_2 \qquad \text{and,} \quad \left.\frac{d^2 w}{dx_1^{\,2}}\right|_{[x_1=0]} = 0 \quad \therefore C_2 = 0$$

$$b \cdot \overline{D}_{11} \cdot \psi = b \cdot \overline{D}_{11} \cdot \frac{dw}{dx_1} = -\frac{P \cdot x_1^{\,2}}{4} + C_3 \qquad \text{and,} \quad \left.\frac{dw}{dx_1}\right|_{\left[x_1 = L/2\right]} = 0 \quad \therefore C_3 = \frac{P \cdot L^2}{16}$$

$$b \cdot \overline{D}_{11} \cdot w = -\frac{P \cdot x_1^{\,3}}{12} + \frac{P \cdot L^2 \cdot x_1}{16} + C_4 \qquad \text{and,} \quad w_{[x_1=0]} = 0 \quad \therefore C_4 = 0$$

Euler-Bernoulli: 3-Point Bending Equations

$$w_1^E = -\frac{P \cdot x_1}{48 \cdot b \cdot \overline{D}_{11}} \cdot \left(3 \cdot L^2 - 4 \cdot x_1^{\,2}\right)$$

$$\psi_1^E = \frac{P}{48 \cdot b \cdot \overline{D}_{11}} \cdot \left(3 \cdot L^2 - 12 \cdot x_1^{\,2}\right)$$

$$M_1^E = \frac{P \cdot x_1}{2}$$

$$Q_5^E = \frac{dM_{(x_1)}^E}{dx_1} = \frac{P}{2}$$

Timshenko: 3-Point Bending Equations

$$w_1^T = w_1^E + \frac{M_1^E}{k^s \cdot b \cdot A_{s55}} = \frac{P \cdot x_1}{48 \cdot b \cdot \overline{D}_{11}} \cdot \left(3 \cdot L^2 - 4 \cdot x_1^{\,2}\right) + \frac{P \cdot x_1}{2 \cdot k^s \cdot b \cdot A_{s55}}$$

$$\psi_1^T = \frac{dw^E}{dx_1} = \frac{P}{48 \cdot b \cdot \overline{D}_{11}} \cdot \left(3 \cdot L^2 - 12 \cdot x_1^{\,2}\right)$$

$$M_1^T = M_1^E = \frac{P \cdot x_1}{2}$$

$$Q_1^T = Q_1^E = \frac{P}{2}$$

* See Appendix 2.8

VITA

Curtis Patrick Nordin was born and raised in Fairbanks, Alaska. He graduated from high school at Far North Christian School. From there, he attended college at the University of Alaska Fairbanks, and received a B.S. in civil engineering with a minor in math in 2005. After which he pursued a graduate degree at the University of Tennessee Knoxville, where he received a M.S. in civil engineering with a structural emphasis in 2008.